Cover Page

Recipient Organization:	University of Minnesota
Project Title:	Optimization and Evaluation of Energy Savings for Connected and Autonomous Off-Road Vehicles
Date of Report:	10/18/2024
Award Number:	DE-EE0009200
Project Manager:	Gurpreet Singh
Project Partner(s):	Texas A&M University, CNH Industrial

ACKNOWLEDGMENT

This material is based upon work supported by the U.S. Department of Energy's Office of Energy Efficiency and Renewable Energy, Vehicle Technologies Office under Award Number DE-EE0009200.

DISCLAIMER

Abstract

Off-road vehicles, such as wheel loaders, excavators, and harvesters, are extensively utilized across a wide range of industries, including construction, agriculture, and mining. These machines have become indispensable in supporting the day-to-day operational needs of a nation, playing a critical role in various sectors' infrastructure and productivity. However, despite their utility, off-road vehicles are significant consumers of fossil fuels, resulting in substantial emissions that contribute to environmental degradation. This highlights the pressing need for research and technological advancements aimed at improving their energy efficiency and reducing their carbon footprint. There are, however, two primary challenges that must be addressed to achieve these goals. First, off-road vehicles typically perform both driving and working tasks simultaneously, which introduces a high level of complexity into their overall dynamic systems. Analysis the interactions between these functions is challenging. Second, research into off-road vehicles is inherently interdisciplinary, demanding expertise across several domains such as fluid power systems, vehicle dynamics, control theory, optimization techniques, and real-world implementation. Recognizing these challenges, we proposed the project titled "Optimization and Evaluation of Energy Savings for Connected and Autonomous Off-Road Vehicles" as a comprehensive solution to enhance fuel efficiency while simultaneously improving productivity. This project specifically focuses on autonomous off-road vehicles, with particular attention to wheel loaders, and seeks to develop novel methods to optimize energy consumption without sacrificing operational performance. The project integrates real-time control algorithms, vehicle dynamics modeling, and co-optimization of powertrain system and vehicle system to achieve these goals.

Our optimization strategy dynamically co-optimizes critical parameters at both the powertrain and vehicle levels, including vehicle speed, working tool movements, powertrain dynamics, and engine operations in real-time. To streamline this optimization process, we developed a vehicle model that captures the key dynamics while significantly enhancing computational efficiency. This allows the system to intelligently minimize fuel consumption, all while maintaining or even improving productivity through real-time calculations during various off-road operations.

To validate the effectiveness of this energy optimization method, we introduced a state-of-the-art Hardware-in-the-Loop (HIL) testbed. This reconfigurable testbed seamlessly integrates the actual engine with virtual models of the wheel loader's subsystems, allowing for accurate emulation of real-world operational loads and environments. By simulating these conditions, the HIL testbed enables us to evaluate the wheel loader’s performance under diverse working scenarios, ensuring the developed solution is applicable in real-world operations. This testbed proved to be instrumental in validating the optimization algorithms and demonstrating the system's practical effectiveness.

During the evaluation and testing phase, we employed the HIL testbed to rigorously assess the energy savings and productivity improvements generated by the optimized system. The results were highly encouraging, revealing that the automated wheel loader achieved over 30% fuel savings compared to traditional, human-operated cycles, with comparable or even enhanced levels of productivity. The insights gained from this HIL-based testing provided critical validation of our approach and highlighted the potential for deploying these optimized autonomous technologies in real-world off-road vehicles

Table of Contents

1. Executive Summary 1
  1.1 Key Objectives 1
  1.2 Project Execution 1
    1.2.1 Task 1 - Optimization Strategy Development 1
    1.2.2 Task 2 - Hardware-in-the-Loop (HIL) Testbed Development 1
    1.2.3 Task 3 - Evaluation and Testing with HIL Testbed 1
  1.3 Project Contributions 2
2. Optimization Strategy Development 3
  2.1 System Modeling 3
    2.1.1 Off-road Vehicle Model 3
    2.1.2 Reduced Order Model 16
    2.1.3 Worksite Simulation 17
    2.1.4 Communication System Development 18
  2.2 Optimization 21
    2.2.1 Transport Phase Optimization 21
    2.2.2 Bucket Loading Optimization 26
    2.2.3 Combined Cycle Optimization 32
3. HIL Testbed Development 42
  3.1 HIL Testbed Design 42
    3.1.1 HIL Testbed Design Overview 43
    3.1.2 Dynamometer 44
    3.1.3 Engine 46
  3.2 HIL Testbed Control 50
    3.2.1 Engine Map Development 51
    3.2.2 Engine Speed Control 52
    3.2.3 Load Torque Control 53
4. Evaluation and Testing with HIL Testbed 56
  4.1 Baseline Evaluation 56
    4.1.1 Cycle Description 56
    4.1.2 Methodology 56
    4.1.3 Baseline Evaluation HIL Test Result 60
  4.2 Partial Automation Evaluation 61

4.2.1 Baseline Cycle Digging Phase 61
4.2.2 Baseline Cycle Transport Phase 62
4.2.3 Optimization for Digging Phase. 62
4.2.4 Optimization for Transport Phase 64
4.2.5 Partial Automation Evaluation 68
4.3 Joint Automation Evaluation 70
4.3.1 Joint Optimization Simulation Result 70
4.3.2 Joint Optimization HIL Test Result 75
4.3.3 Joint Automation Evaluation Summary 77
4.4 Different Scenarios Evaluation 77
4.4.1 HIL Evaluation for the Straight-Line Pile Optimization Profile 77
4.4.2 HIL Evaluation for the Curve Pile Optimization Profile 79
5. Summary and Conclusions 81
6. Publications and Patents 82

1. Executive Summary

The project "Optimization and Evaluation of Energy Savings for Connected and Autonomous Off-Road Vehicles" aims to develop systematic methods and tools to optimize and evaluate energy savings for connected and autonomous off-road vehicles. The objective is to achieve 20-40% energy savings while improving productivity. This will be achieved by implementing real-time optimization and control systems, developing a hardware-in-the-loop (HIL) testbed, and conducting HIL-based testing to validate these systems. The project focuses on co-optimizing vehicle dynamics and powertrain operations through connectivity and automation, with the testbed being capable of evaluating different off-road vehicle architectures and operation scenarios.

1.1 Key Objectives

The project focused on implementing advanced real-time control algorithms for co-optimizing vehicle speed, engine performance, and tool motions in autonomous off-road vehicles. By developing a flexible and reconfigurable Hardware-in-the-Loop (HIL) testbed, the project enabled accurate real-time evaluations of vehicle operations, energy consumption, and system dynamics. The primary goal was to achieve significant energy savings, targeting a 20-40% improvement in fuel efficiency. These improvements were validated through simulation and HIL-based testing, demonstrating the system's effectiveness across a variety of operating scenarios.

1.2 Project Execution

1.2.1 Task 1 - Optimization Strategy Development

The project developed an optimization strategy that co-optimizes vehicle motion, powertrain dynamics, and fluid power system operations. It integrates data from communication systems to make real-time adjustments based on vehicle conditions. A simplified vehicle model was created to accelerate computation during optimization.

1.2.2 Task 2 - Hardware-in-the-Loop (HIL) Testbed Development

The HIL testbed allows the physical testing of the control algorithms and optimization system by simulating a real-world environment. The testbed includes real engine components and uses a transient dynamometer to emulate vehicle loads during operational cycles.

1.2.3 Task 3 - Evaluation and Testing with HIL Testbed

The testbed was used to evaluate energy savings and productivity improvements. The project validated over 30% fuel savings through real-time testing compared to traditional, non-optimized cycles.

1.3 Project Contributions

The contributions of the project are substantial in advancing both the field of off-road vehicle research and the broader context of energy efficiency for autonomous systems. The project developed an innovative optimization and control system that successfully demonstrated how real-time co-optimization of vehicle dynamics, powertrain systems, and tool operations can lead to significant improvements in energy efficiency without compromising productivity. The integration of Hardware-in-the-Loop (HIL) testing further validated the performance of these algorithms, providing a robust method for real-world simulation and evaluation. The project's approach demonstrated more than 30% fuel savings compared to traditional human-operated cycles, offering a clear pathway to reducing the energy consumption of off-road vehicles.

In terms of off-road vehicle research, this project has laid the groundwork for future innovations in the design and control of autonomous systems. By focusing on real-time optimization and system integration, it has provided a framework that can be adapted to various vehicle types and tasks, making it highly applicable across the off-road vehicle domain. The use of HIL testbeds allows for ongoing testing and refinement of control strategies, ensuring that these systems remain adaptable to changing conditions and evolving technological demands.

From an energy efficiency perspective, the project contributes to the growing body of research aimed at reducing the environmental impact of heavy machinery and vehicles. The ability to optimize vehicle operations dynamically, in response to real-time data, offers the potential for significant reductions in fuel consumption and emissions. This not only benefits individual vehicles but also contributes to a more sustainable and energy-efficient operation across entire fleets and industries. The insights gained from this project have the potential to influence energy management strategies for the off-road vehicle community and beyond, driving a shift towards more sustainable practices in the use of autonomous technologies in agriculture, construction, mining, and other sectors.

2. Optimization Strategy Development

The optimization strategy will be developed, which controls the target off-road vehicle based on the communicated information through connectivity and performs the co-optimization of vehicle speed and tool motion, fluid power system and the engine through automation. To formulate the model-based optimization problem, the target off-road vehicle model will be developed. Efficient numerical methods will be applied to solve the optimization.

2.1 System Modeling

This part consists of the following work:

I. Off-road vehicle model
II. Reduced order model
III. Worksite simulation
IV. Communication system development

2.1.1 Off-road Vehicle Model

The off-road vehicle model focuses on capturing the energy consumption of key components in a wheel loader, such as the drivetrain, hydraulic systems, and steering mechanisms. The target architecture is depicted in Fig. 1, which outlines the main components. The simulation model, developed in MATLAB Simulink, serves as a foundation for understanding energy flows and optimizing efficiency. Creating an accurate model is essential for analyzing the energy demands and interactions of each subsystem to achieve significant energy savings.

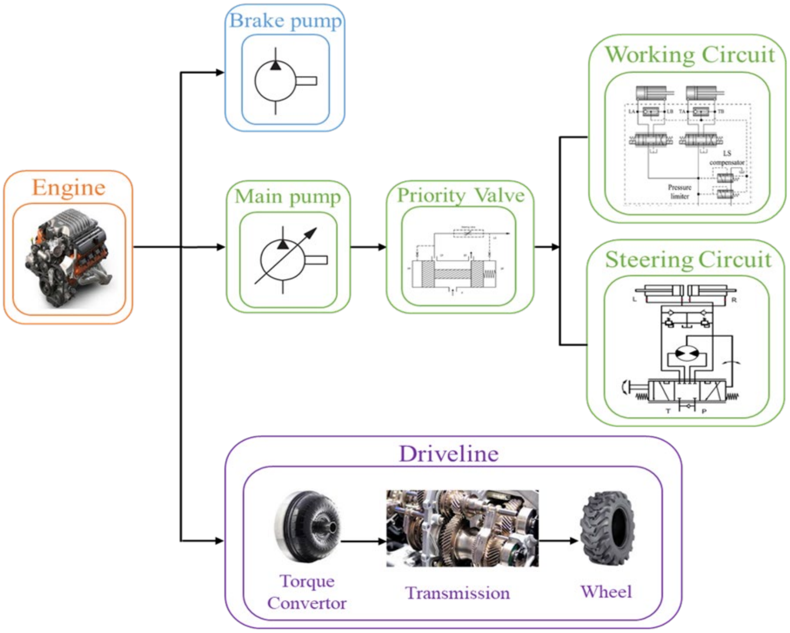

Figure 1. The target wheel loader model

2.1.1.1 Engine Model

The engine shaft is connected to the torque converter pump, the implement pump for the work and steering circuit, and the brake pump. The shaft dynamics are given by the following equation:

$$T_e - T_p - T_w - T_b = J\dot{\omega}_e + b\omega_e \tag{1}$$

where T_e is the torque produced by the engine, T_p is the pump torque for the torque converter, T_w is the hydraulic work and steering circuit torque, T_b is the brake circuit torque, ω_e is the shaft speed, J is the lumped inertia of the engine shaft and the three pumps, and b is the friction coefficient for the engine shaft.

The engine is modeled by an engine map which relates throttle, speed and torque. With any of those two variables known, the third one can be determined. The engine map functions as a 2-D lookup table. In this case, the engine map takes throttle and speed as inputs to determine the torque produced.

2.1.1.2 Driveline Model

The driveline model consists of a torque converter, transmission, and wheel model. The torque converter pump is connected to the engine shaft, while the turbine is connected to the gear set. Transmission is a set of gears with a gear ratio determined by a shift schedule.

Torque converter

The torque converter is modeled by two different methods, the Kotwicki method and the K-factor method, each of which takes the pump and turbine speed as inputs to determine the pump and turbine torques. The Kotwicki method employs the regression fitting technique based on pump speed squared, turbine speed squared, and the product of the two speeds. The Kotwicki model equations to determine pump torque T_p and turbine torque T_t are stated as follows:

$$T_p = a_1{\omega_p}^2 + a_2\omega_p\omega_t + a_3{\omega_t}^2 \tag{2}$$

$$T_t = b_1{\omega_p}^2 + b_2\omega_p\omega_t + b_3{\omega_t}^2 \tag{3}$$

and for the fluid coupling mode ($\omega_t/\omega_p > 0.9$):

$$T_p = T_t = c_1{\omega_p}^2 + c_2\omega_p\omega_t + c_3{\omega_t}^2 \tag{4}$$

where ω_p is the pump speed and ω_t is the turbine speed. The Kotwicki coefficients a_i, b_i, and c_i are determined by a least-square regression fitting of experimental data.

The K-factor method uses a look-up table instead of a curve fitting. The speed ratio (ω_t/ω_p), torque ratio (T_t/T_p) and K-factor are recorded from experimental data. The K-factor is defined as:

$$K - factor = \omega_p / \sqrt{T_p} \tag{5}$$

The K-factor and the torque ratio can be uniquely determined by the speed ratio for a particular torque converter. Thus, for all pump and turbine speeds, the pump and turbine torque can be determined.

Transmission

The transmission gear ratio is determined by a shift schedule, which determines whether to upshift or downshift based on the current gear, engine throttle, and vehicle speed. The shift schedule is calibrated separately for forward and reverse, which have differing sets of gear ratios. A lookup table determines the minimum vehicle speed required to shift up, and the maximum vehicle speed required to shift down. A shift occurs when the vehicle speed either exceeds the upshift speed or is less than the downshift speed. Additional shifts are prevented during shift-transience.

The shift dynamics are then modeled by a first-order transfer function the reaches steady-state in 0.5 seconds, which is the approximate transient time of a gear shift. The gear ratio amplifies the torque converter turbine torque as it is transmitted to the drive shaft.

The gear ratio is determined by the gear command and whether the vehicle is traveling in forward or reverse.

Wheel

The wheel model uses the drive torque from the transmission and the load on the vehicle to determine vehicle acceleration. This is modeled at the drive shaft as described by the following equations.

$$T_{drive} - T_{load} = (J_r + J_f)\dot{\omega}_f \tag{6}$$

$$T_{load} = \frac{R_{wh}}{k_f}\left(\mu m g + \frac{1}{2}\rho v^2 C_d A + F_{th}\right) \tag{7}$$

where T_{drive} is the torque on the drive shaft, T_{load} is the vehicle load torque, J_r is the inertia of the transmission ring gear and drive shaft, J_f is the vehicle inertia on the final drive shaft, $\dot{\omega}_f$ is the acceleration of the final drive shaft, R_{wh} is the wheel radius, k_f is the final drive ratio, μ is the rolling friction coefficient of the wheels, m is the vehicle mass, g is acceleration due to gravity, ρ is the density of air, v is the vehicle speed, C_d is the drag coefficient, A is the cross-sectional area of the vehicle, and F_{th} is the thrust resistance force when the bucket is used.

2.1.1.3 Hydraulic System Model

The hydraulic system model consists of main pump, priority valve, working circuit, and steering circuit.

Main pump

The main pump in the wheel loader is a variable displacement pump, which can be triggered the variable displacement by the flow compensated mechanism. The pump will deliver only the flow required by the hydraulic circuit, which is realized by the flow compensation mechanism. The load sensing signal is received and connected to the spring side of flow regulator. Together with spring, when the load sensing signal overcomes the pump outlet pressure on the other side of flow regulator, the flow regulator is in the closed position. The counterbalance spring pushes the swash plate to larger displacement position. Once the pump outlet pressure increases to overcome the load sensing signal together with the flow regulator spring, it will be ported to the control piston through the flow regulator spool. The control piston pushes the swash plate to smaller displacement position. The load sensing signal is the highest load pressure that occurs through the hydraulic working and steering circuit.

The torque T_{mp} and the outlet flow Q_{mp} of the main implement pump are given by

$$T_{mp} = \frac{P_m x_m D_m}{\eta_{mm}} \tag{8}$$

and

$$Q_{mp} = x_m D_m \omega_e \eta_{mv} \tag{9}$$

respectively, where P_m is main pump outlet pressure, x_m is the displacement fraction of the main pump, D_m is the full displacement of the main pump, η_{mm} is the mechanical efficiency of the main pump, ω_e is the engine speed, η_{mv} is the volumetric efficiency of the main pump.

The outlet chamber of the hydraulic main pump connects to the inlet of the priority valve. The main pump provides the pressure and flow for both the work and steering circuits. The hydraulic pressure P, at any point can be calculated by Eq. (10).

$$\frac{dP}{dt} = \frac{\beta}{V}(Q_{in} - Q_{out}) \tag{10}$$

where β is the bulk modulus of fluid, V is the control volume, Q_{in} is the inlet flow, Q_{out} is the outlet flow. The main pump outlet pressure, P_{mp}, can be found using this equation.

$$\dot{P}_{mp} = \frac{\beta}{V_{mp}}(Q_{mp} - Q_{CF} - Q_{EF}) \tag{11}$$

Where Q_{CF} and Q_{EF} are the steering and work circuit flows respectively.

Priority valve

Steering is more critical to the operation of the wheel loader, so the priority valve is used to provide oil to the steering circuit first. Once the steering circuit is satisfied, all of the excess supply oil is then available to the loader hydraulic system. The schematic of the priority valve is shown below in Fig. 2. It is a pilot assisted spool-spring system. The CF (Control Flow) directs to the steering circuit, the PP is the pilot port, the P port is from the supply pump, the EF (Excess Flow) directs the flow to other hydraulic circuits and the LS (Load Sensing) receives feedback from the steering circuit. The flow distribution to CF or EF ports is determined by the position of the spool, which depends on the pilot pressure, the pre-adjusted spring and the pressure buildup in the spring chamber. When there is no steering, even though the LS pressure is low, pre-adjusted spring together with LS pressure moves the spool to the left side, which opens the CF port. The pressure in PP chamber will build up, then overcomes the spring and LS pressure, which moves the spool to the right side. Then the flow directs to EF port. Internally, there will be flow from CF port to the spring chamber and finally to tank. When the steering circuit works, the LS pressure together with the spring overcomes the pilot pressure, which moves the spool inside the valve. Consequently, the flow will be directed to CF port until the steering circuit meets requirement. Meanwhile, the flow to EF port will slowly reduce or even stop. The LS pressure increases as the steering unit turns because flow will be supplied to the LS port, which is LS flow. While the steering stops, the LS flow will stop and the LS pressure will decrease.

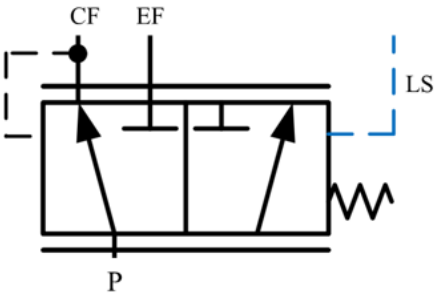

Figure 2. schematic of priority valve

The key part of the priority valve is the spool dynamics, which determines the flow to CF port and EF port. Based on Newton's law, the spool dynamics is governed by the below equation.

$$m_y\ddot{X} = \left(P_{pp} - P_{sp}\right)A_y - \left(B_v + B_f\right)\dot{X} - K_f X - k(x_0 + X) - F_{nl}(X) \tag{12}$$

where m_y is the mass of valve spool and spring, $\ddot{X}, \dot{X}, X$ is the acceleration, velocity and displacement of the spool, respectively, P_{pp} is the pilot chamber pressure, P_{sp} is the spring chamber pressure, A_y is the effective function area of valve spool, B_v is the viscous friction coefficient between valve spool and valve, B_f is the transient liquid dynamic damping coefficient, k is the valve spool spring stiffness, K_f is the steady liquid dynamic stiffness, x_0 is spring pre-compression value, F_{nl} is the mechanical stop force.

The first term is the pressure force caused by the pressure difference between the pilot chamber and spring chamber. The second term is the total damping force. The third term and the fourth term correspond to the spring force and pre-compression force. The last term on the right side is the mechanical stop force.

Hydraulic working circuit

The hydraulic working circuit has two functions: lift and tilt. The lift function is for raising and lowering the bucket (two lift cylinders) and tilt function is for loading and dumping material (one tilt cylinder). The schematic diagram of the hydraulic working circuit is shown in Figure 3, which shows only one lift cylinder for simplicity. The lift and tilt function are powered by the variable pressure and flow compensated pump. Each function is controlled by a proportional valve.

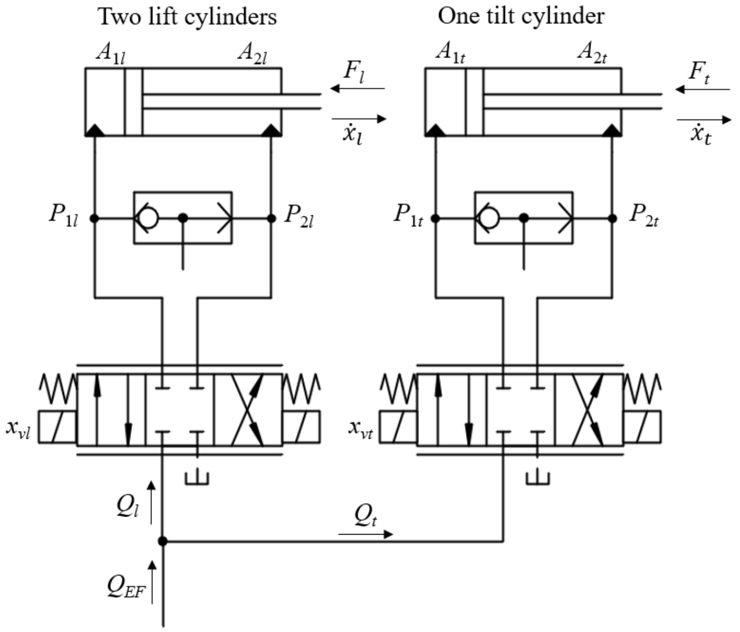

Figure 3. Schematic of hydraulic working circuit

The system consists of the following parts:

i. Lift valve flow calculation
ii. Tilt valve flow calculation
iii. Lift cylinders
iv. Tilt cylinder

1) Lift valve flow calculation

The valve flow rate can be calculated by the orifice flow equation

$$Q_{valve} = C_d A_{orifice} \sqrt{\frac{2|\Delta P|}{\rho}} sign(\Delta P) \tag{13}$$

where Q_{valve} is the valve flow rate, C_d is the flow coefficient, $A_{orifice}$ is the orifice area, ΔP is the pressure difference across the orifice, ρ is the oil density.

In this model, we assume the flow coefficient is a constant value 0.62 and the oil density is 850 kg/m^3. Lift valve flow calculation is based on the equation mentioned above.

2) Tilt valve flow calculation
Similarly, tilt valve flow calculation is based on the orifice flow equation mentioned before.

3) Lift cylinders

The lift piston dynamics is given by

$$m_l \ddot{x}_l = p_{1l} A_{1l} - p_{2l} A_{2l} - F_l - f_l - B_l \dot{x}_l \tag{14}$$

where m_l is mass of the lift piston, F_l is the load force of the lift piston, f_s is the frictional force of the lift piston, B_l is the viscous coefficient of the lift piston, $\ddot{x}_l$ is the acceleration of the lift piston, $\dot{x}_l$ is velocity of the lift piston, x_l is the displacement of the lift piston, A_{1l} is the piston chamber action area of the lift cylinder, A_{2l} is the rod chamber action area of the lift cylinder, P_{1l} is the piston chamber pressure of the lift cylinder, P_{2l} is the rod chamber pressure of the lift cylinder.

4) Tilt cylinder

The tilt cylinder dynamics is given by

$$m_t \ddot{x}_t = p_{1t} A_{1t} - p_{2t} A_{2t} - F_t - f_t - B_t \dot{x}_t \tag{15}$$

where m_t is mass of the tilt piston, F_t is the load force of the tilt piston, f_t is the frictional force of the tilt piston, B_l is the viscous coefficient of the tilt piston, $\ddot{x}_l$ is the acceleration of the tilt piston, $\dot{x}_t$ is velocity of the tilt piston, x_t is the displacement of the tilt piston, A_{1t} is the piston chamber action area of the tilt cylinder, A_{2t} is the rod chamber action area of the tilt cylinder, P_{1t} is the piston chamber pressure of the tilt cylinder, P_{2t} is the rod chamber pressure of the tilt cylinder.

Hydraulic steering circuit

The hydraulic steering circuit is shown in Figure 4. The steering control unit consists of a steering valve, a torque generator or gerotor pump, two relief valves and two check valves. The steering wheel column is connected to the spool of the steering valve. Once received commands from the operator, the steering valve allows the passage of fluid from the variable pressure and flow compensated pump to the gerotor pump that displaces successively the fluid to the steering cylinders. The gerotor pump rotates due the pressure difference between its two ports. Once the gerotor pump which is connected to the sleeve of the steering valve begins to displace fluid, the sleeve will follow the rotation of the spool. Due to the feedback movement of the sleeve, the connection with the steering cylinders is closed and they stop moving, therefore performing the steering of the vehicle tires according to the input of the operator. The steering cylinders are connected to the steering mechanism and perform the steering of the vehicle tires.

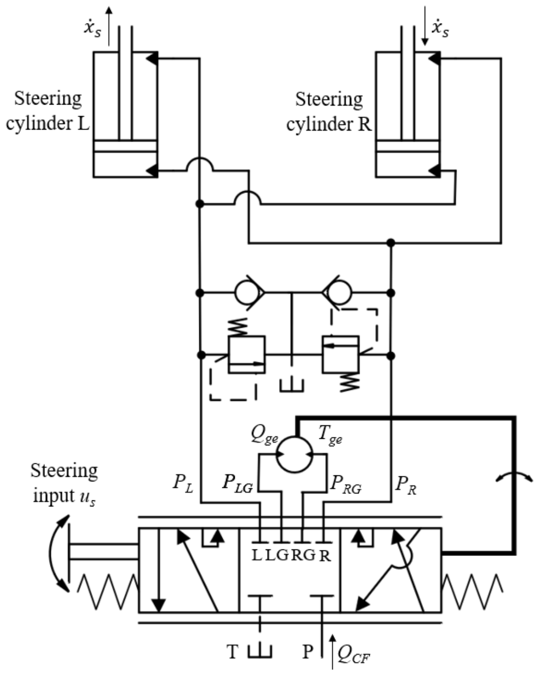

Figure 4. schematic of hydraulic steering circuit

The system is composed of the following parts:

i. Spool and sleeve dynamic
ii. Valve flow calculation
iii. Gerotor pump
iv. Steering cylinders

The key part of the hydraulic steering circuit is the directional valve realized by means of a rotary spool and a sleeve. Due to the angular position of the spool and sleeve, the flow areas that appear and disappear allow fluid to flow to gerotor pump and then to the steering cylinders. The two components are the fundamental elements of the hydraulic steering circuit and affect the behavior of the steering and the feeling on the steering wheel controlled by the operator.

For the spool dynamic, given the steering wheel speed input, integrating it can determine the spool angle during the time interval. For the sleeve dynamic, the gerotor torque, the damping friction torque and the spring torque drive the sleeve.

$$J_2\ddot{\theta} = T_{ge} + K_v\left(\dot{\delta} - \dot{\theta}\right) + K_s(\delta - \theta) \tag{16}$$

where δ is the angle of spool, θ is the angle of the sleeve, $\ddot{\theta}$ is the sleeve angular acceleration, $\dot{\theta}$ is the sleeve speed, $\dot{\delta}$ is the spool speed (also the steering wheel speed), T_{ge} is the torque generated by gerotor pump, J_2 is the inertia of momentum of sleeve and gerotor pump (connected to sleeve), K_v is the damping coefficient of spool-sleeve, K_s is the spring coefficient of spool-sleeve.

2) Valve flow calculation

The steering input will change the orifice opening between the pressure port to one work port of the steering cylinders, and the orifice opening between the other work port to the tank. Therefore, the steering valve is modelled using variable hydraulic orifices connected in parallel to represent each of the flow passages through the valve. The valve flow rate can be calculated by the orifice flow equation mentioned before. Here the orifice area is a function of the relative angular position between the spool and the sleeve. Figure 5 from exisiting literature shows the flow areas trends.

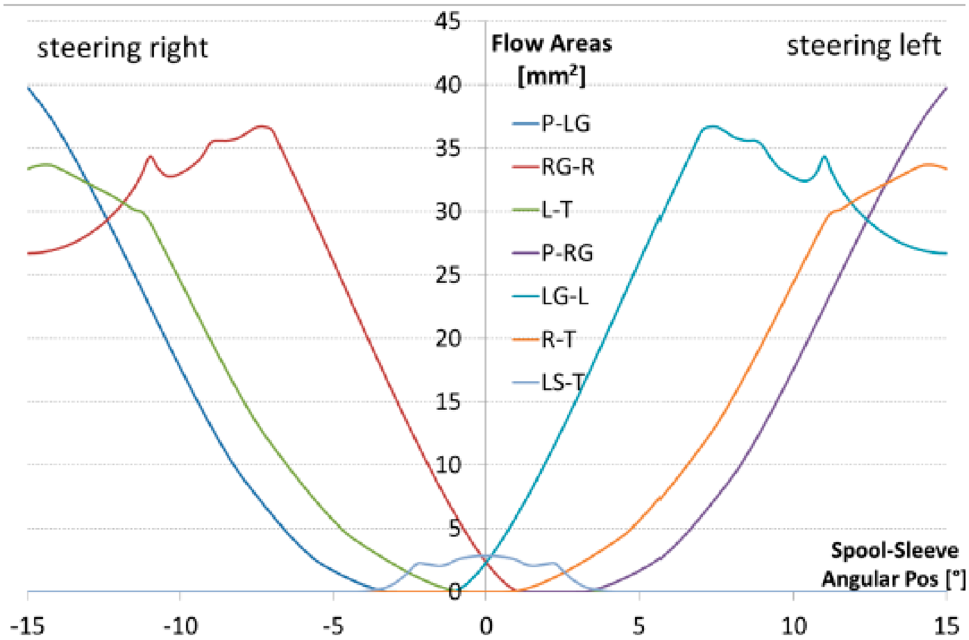

Figure 5. Valve Flow Areas Trends as Function of the Relative Angular Position between Spool and Sleeve

In this model, a linear approximation is used to capture the trend shown above.

3) Gerotor pump

The gerotor pump ports are connected to the steering valve by means of internal cavities. The gerotor pump in this model is a fixed displacement pump. As the operator turns the steering wheel, the spool rotates first. The relative angle between the spool and the sleeve increases, thus raising the pressure difference across the gerotor pump. Torque generated by this pressure difference will be applied to the sleeve to catch up with the spool. Therefore, there are two parameters needed in the gerotor pump model: gerotor pump torque and gerotor pump flow rate, which is used to calculate the transient inlet and outlet pressure of the gerotor pump.

For gerotor pump torque, it can be determined by the equation.

$$T_{ge} = D_p \times (P_{inlet} - P_{outlet}) \times \eta_{wm} \tag{17}$$

where T_{ge} is the gerotor torque, D_p is the displacement of gerotor pump, P_{inlet} is the gerotor pump inlet pressure, P_{outlet} is the gerotor pump outlet pressure, η_{wm} is the mechanical efficiency of the gerotor pump.

For gerotor pump flow rate, it can be determined by this equation.

$$Q_{ge} = D_p \times \omega_{sleeve} \times \eta_{wv} \tag{18}$$

where Q_{ge} is the gerotor pump flow rate, D_p is the displacement of gerotor pump, w_{sleeve} is the gerotor pump speed, η_{wv} is the volumetric efficiency of the gerotor pump.

4) Steering cylinders

The steering cylinders are connected to the steering valve as steering actuators. Two cylinders are cross connected. Change of the displacement of cylinders will cause the change of wheel steering angles.

The steering piston dynamics is given by

$$m_s \ddot{x}_s = p_{1s}A_s - p_{2s}A_s - F_s - f_s - B_s\dot{x}_s \tag{19}$$

where m_s is mass of the steering piston, F_s is the load force of the steering piston, f_s is the frictional force of the steering piston, B_s is the viscous coefficient of the steering piston, $\ddot{x}_s$ is the acceleration of the steering piston, $\dot{x}_s$ is velocity of the steering piston, x_s is the displacement of the steering piston, A_s is the piston area of the steering cylinders since they are symmetric, P_{1s} is the piston chamber pressure of the steering cylinder, P_{2s} is the rod chamber pressure of the steering cylinder.

2.1.1.4 Bucket Linkage Model

The diagram of the bucket linkage is shown in Figure 6. The linkage is used to control the motion of the bucket and is actuated by three hydraulic cylinders including one tilt and two lift cylinders. (One lift cylinder is shown in the Figure 6, while there is one more behind that.) The height of the bucket can be controlled by changing the lengths of the lift cylinders, while the length of tilt cylinder can be adjusted to change the orientation of the bucket. In this linkage, the lift cylinders and lift arm are attached to the wheel loader through the joints Y and A, respectively.

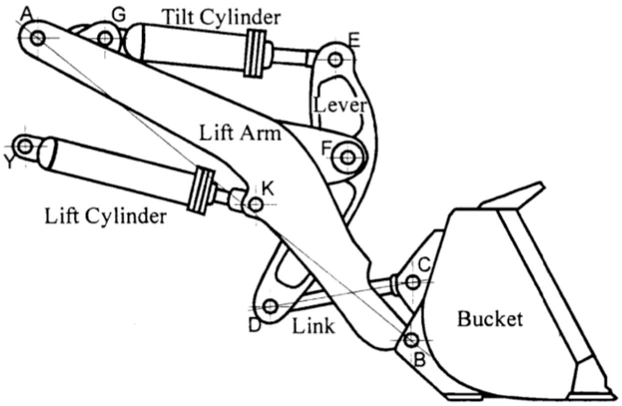

Figure 6. Schematic of Bucket Linkage

The objective of the modeling is, given the lengths of the cylinders and the forces on them, to determine the motion of the bucket, including its position and orientation. To derive the dynamic model, the system containing lift arm, lever, link, and the bucket is considered. The Lagrange's method is used for modeling and the procedures are:

i. Geometry Analysis
ii. Generalized forces analysis
iii. Lagrangian formulation
iv. Equations of motion

1) Geometry Analysis
As shown in Figure 7, the origin of the coordinate system is defined to at the joint Y. The position of the bucket tip, i.e., (x_t, y_t), is used to denote the position of the bucket. The orientation of the bucket is defined as the angle between the bucket tip and the horizontal line, with the tip lower than the horizontal line being positive.

The lengths $|AY|$, $|AK|$, $|AB|$, $|AF|$, $|AG|$, $|KB|$, $|GF|$, $|GK|$, $|KF|$, $|EF|$, $|FD|$, $|DE|$, $|CD|$, and $|BC|$ are known since they are fixed values and can be measured in advance. In addition, the angle β, between the line AY and the horizontal line, as indicated in the figure is also determined. So are the values z_t, the initial vertical distance between joint B and the bucket tip, and h_t, the initial horizontal distance between joint B and the bucket tip. The lengths of the cylinders vary during operation, so they are treated as variables l_l, the length of lift cylinders, and l_t, the length of tilt cylinder. According to Figure 7, $l_l = |YK|$ and $l_t = |GE|$.

With all above values known, the position of joints K and G can be expressed as functions of l_l, i.e., $\vec{r}_K = \vec{r}_K(l_l)$ and $\vec{r}_G = \vec{r}_G(l_l)$. Also, the positions of joint E and the bucket tip can be expressed as functions of both l_l and l_t, i.e., $\vec{r}_E = \vec{r}_E(l_l, l_t)$ and $\vec{r}_t = \vec{r}_t(l_l, l_t) = \big(x_t(l_l, l_t), y_t(l_l, l_t)\big)$.

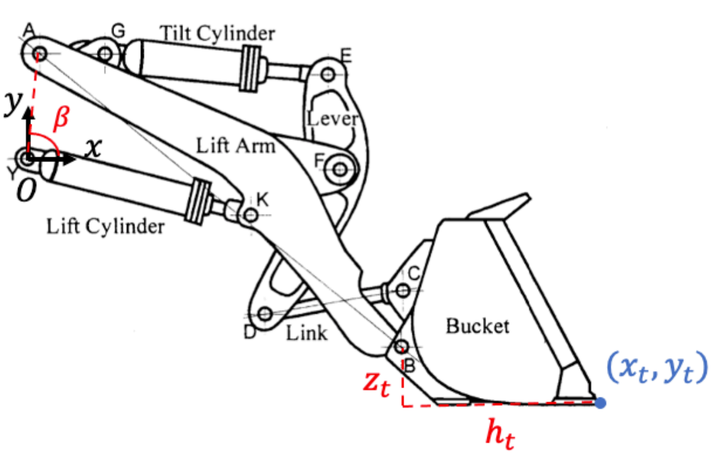

Figure 7. The Coordinate System for the Linkage

2) Generalized forces

The forces acting on the system are shown in Figure 8, where F_l is the force generated from lift cylinders, F_t is the force generated from tilt cylinder, and P_x and P_y are the forces acting on the bucket from the soil in horizontal and vertical direction, respectively.

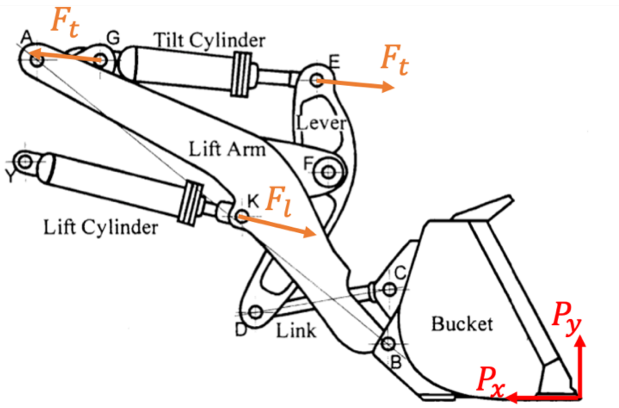

Figure 8. Forces Acting on the System

Then, the generalized forces Q_l and Q_t associated with variables l_l and l_t are:

$$Q_l = 2F_l \frac{\vec{r}_K}{l_l} \cdot \frac{\partial \vec{r}_K}{\partial l_l} + F_t \frac{\vec{r}_G - \vec{r}_E}{l_t} \cdot \left(\frac{\partial \vec{r}_G}{\partial l_l} - \frac{\partial \vec{r}_E}{\partial l_l} \right) + (-P_x \hat{\imath} + P_y \hat{\jmath}) \cdot \frac{\partial \vec{r}_t}{\partial l_l} \tag{20}$$

$$Q_t = -F_t \frac{\vec{r}_G - \vec{r}_E}{l_t} \cdot \frac{\partial \vec{r}_E}{\partial l_t} + (-P_x \hat{\imath} + P_y \hat{\jmath}) \cdot \frac{\partial \vec{r}_t}{\partial l_t} \tag{21}$$

3) Lagrangian

The Lagrangian is defined as the sum of the kinetic energy and the potential energy of all components in the system. For the lift arm, it undergoes only pure rotation relative to the body of the wheel loader, while for other three components, they undergo both rotational and translational motions. Therefore, it is assumed that the moment of inertia of lift arm about the joint A, J_{Lift}^{A}, and the moments of inertia of other three components about their centers of mass, J_{Lever}^{CM}, J_{Link}^{CM}, and J_{Bucket}^{CM}, are known. In addition, the masses of all the components, m_{Lift}, m_{Lever}, m_{Link}, and m_{Bucket}, are also known.

By the geometric approach, we can also express the centers of mass of the four components as functions of l_l and l_t, i.e., $\left(x_{Lift}^{CM}(l_l), y_{Lift}^{CM}(l_l)\right)$, $\left(x_{Lever}^{CM}(l_l, l_t), y_{Lever}^{CM}(l_l, l_t)\right)$, $\left(x_{Link}^{CM}(l_l, l_t), y_{Link}^{CM}(l_l, l_t)\right)$, and $\left(x_{Bucket}^{CM}(l_l, l_t), y_{Bucket}^{CM}(l_l, l_t)\right)$. In addition, the angles of the components relative to the horizontal axis are expressed as functions of l_l and l_t, i.e., $\theta_{Lift}(l_l)$, $\theta_{Lever}(l_l, l_t)$, $\theta_{Link}(l_l, l_t)$, and $\theta_{Bucket}(l_l, l_t)$.

Therefore, the kinetic energy of the lift arm is given by

$$T_{Lift} = \frac{1}{2} J_{Lift}^{A} \dot{\theta}_{Lift}^{2} \tag{22}$$

For the lever, the kinetic energy is given by

$$T_{Lever} = \frac{1}{2} J_{Lever}^{CM} \dot{\theta}_{Lever}^{2} + \frac{1}{2} m_{Lever} \left({\dot{x}_{Lever}^{CM}}^{2} + {\dot{y}_{Lever}^{CM}}^{2} \right) \tag{23}$$

The other two components, link and bucket, have the kinetic energies as the same form. The potential energy of the lift arm is given by

$$V_{Lift} = m_{Lift} g y_{Lift}^{CM} \tag{24}$$

The other three components have the same form of potential energies. So the Lagrangian is given by

$$\mathcal{L} = \left(T_{Lift} + T_{Lever} + T_{Link} + T_{Bucket} \right) - \left(V_{Lift} + V_{Lever} + V_{Link} + V_{Bucket} \right) \tag{25}$$

4) Equations of motion

According to the Lagrange's method, the generalized forces and the Lagrangian can be used to determine the equations of motion as:

$$\frac{d}{dt}\left(\frac{\partial \mathcal{L}}{\partial \dot{l}_l}\right) - \frac{\partial \mathcal{L}}{\partial l_l} = Q_l \tag{26}$$

$$\frac{d}{dt}\left(\frac{\partial \mathcal{L}}{\partial \dot{l}_t}\right) - \frac{\partial \mathcal{L}}{\partial l_t} = Q_t \tag{27}$$

These equations finally give two second-order differential equations:

$$\begin{bmatrix} \frac{\partial}{\partial \dot{l}_t}\left(\frac{\partial \mathcal{L}}{\partial \dot{l}_t}\right) & \frac{\partial}{\partial \dot{l}_l}\left(\frac{\partial \mathcal{L}}{\partial \dot{l}_t}\right) \\ \frac{\partial}{\partial \dot{l}_t}\left(\frac{\partial \mathcal{L}}{\partial \dot{l}_l}\right) & \frac{\partial}{\partial \dot{l}_l}\left(\frac{\partial \mathcal{L}}{\partial \dot{l}_l}\right) \end{bmatrix} \begin{bmatrix} \ddot{l}_t \\ \ddot{l}_l \end{bmatrix} = \begin{bmatrix} Q_t + \frac{\partial \mathcal{L}}{\partial l_t} - \frac{\partial}{\partial l_t}\left(\frac{\partial \mathcal{L}}{\partial \dot{l}_t}\right) \dot{l}_t - \frac{\partial}{\partial l_l}\left(\frac{\partial \mathcal{L}}{\partial \dot{l}_t}\right) \dot{l}_l \\ Q_l + \frac{\partial \mathcal{L}}{\partial l_l} - \frac{\partial}{\partial l_t}\left(\frac{\partial \mathcal{L}}{\partial \dot{l}_l}\right) \dot{l}_t - \frac{\partial}{\partial l_l}\left(\frac{\partial \mathcal{L}}{\partial \dot{l}_l}\right) \dot{l}_l \end{bmatrix} \tag{28}$$

which is the final form of the dynamics model of the bucket linkage system.

2.1.1.5 Integrated Vehicle Model

System validation is performed using field test data at the subsystem level and at the overall system level. For engine and drivetrain models, engine shaft dynamics and drive shaft dynamics are validated. For the hydraulic working circuit and the hydraulic steering circuit, the flows produced by the model are compared with experimental data with high accuracy. For this fully integrated system model, the difference between the measured fuel consumption of the loading cycle and the simulation result is 2.3%, which is shown in Fig. 9.

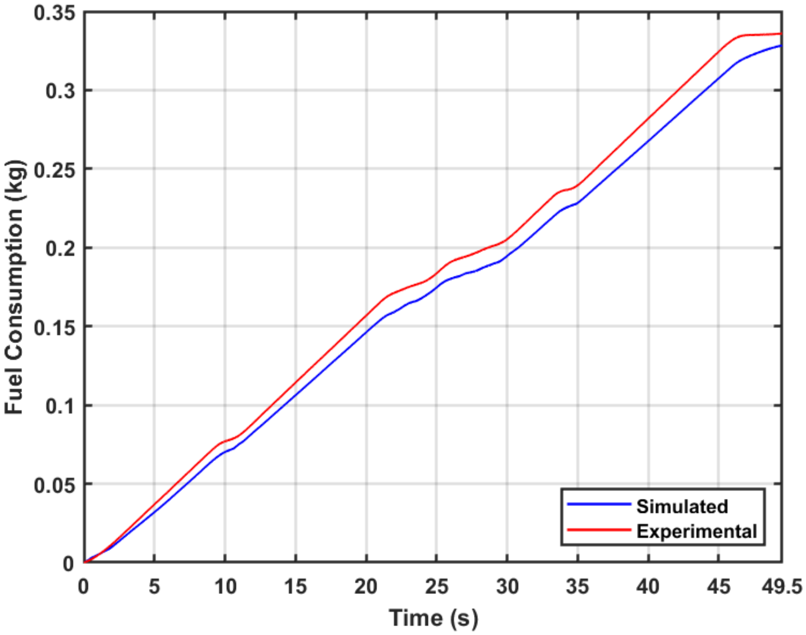

Figure 9. fuel consumption comparison

2.1.2 Reduced Order Model

The main work discussed in the provided document focuses on model order reduction (MOR) for a wheel loader system, specifically targeting the driveline, working hydraulic, and steering hydraulic systems. The goal of this reduction is to decrease the complexity of the model by 30%, ensuring that the reduced-order models remain computationally efficient while maintaining accuracy similar to the full-order models.

1) Driveline System:
The driveline system, initially of third-order, includes key components such as the engine, torque converter, and vehicle speed. By eliminating the gear ratio time delay, the system is reduced to second-order. Simulations comparing the reduced-order model with the full-order model show that the reduced model closely mirrors the performance of the full-order model, with minimal error (0% for engine speed and 0.29% for engine torque), and a reduction in running time by 9.3%.

2) Hydraulic Working System:
The working hydraulic system, originally of eighth-order, models the lift and tilt cylinders, including the pressure and flow dynamics in the cylinder chambers. The model is reduced to sixth-order by replacing the individual chamber pressures with pressure differences and simplifying the flow rate equations. The reduced-order model is tested through simulations, showing very close results to the full-order model, with errors as low as 0.00044% for lift cylinder displacement and a significant reduction in running time by 47.6%.

3) Hydraulic Steering System:
The steering hydraulic system, initially a ninth-order system, controls the steering through pressure differences across chambers and a gerotor. By defining new variables for pressure differences and reducing the differential equations, the system is reduced to sixth-order. Simulations indicate minimal errors (0.000028% for flow rate and 0.000038% for piston displacement), with a 60.1% reduction in computation time.

4) Integrated System:
The subsystems are integrated into a full system using load-sensing pumps and priority valves. The final reduced-order model combines all subsystems into a 14th-order system, down from the original 20th order, achieving the target 30% reduction. The integrated model retains high accuracy with errors under 1%, ensuring that the reduced model performs similarly to the full-order version while offering substantial computational efficiency gains.

In summary, the MOR process effectively reduces the computational load while preserving the essential dynamics and accuracy of the original models. This reduction is crucial for real-time optimization applications, especially in complex systems like wheel loaders.

2.1.3 Worksite Simulation

The worksite simulation software is designed to optimize the operation of connected autonomous vehicles for repetitive earthmoving tasks on construction or mining sites. The goal of this software is to facilitate macro-level site optimization by planning vehicle movements, including their starting and ending positions and orientations during loading cycles. This optimization ensures that vehicles complete their tasks in the most efficient and time-effective manner. The software's main audience consists of site managers or general contractors, and its interface is intended to be user-friendly, allowing non-technical users to input necessary site and task information. The software then generates vehicle commands in two forms: precise trajectory points for vehicle-level control and graphical representations for operators to review and adjust if needed. The flowchart is shown below.

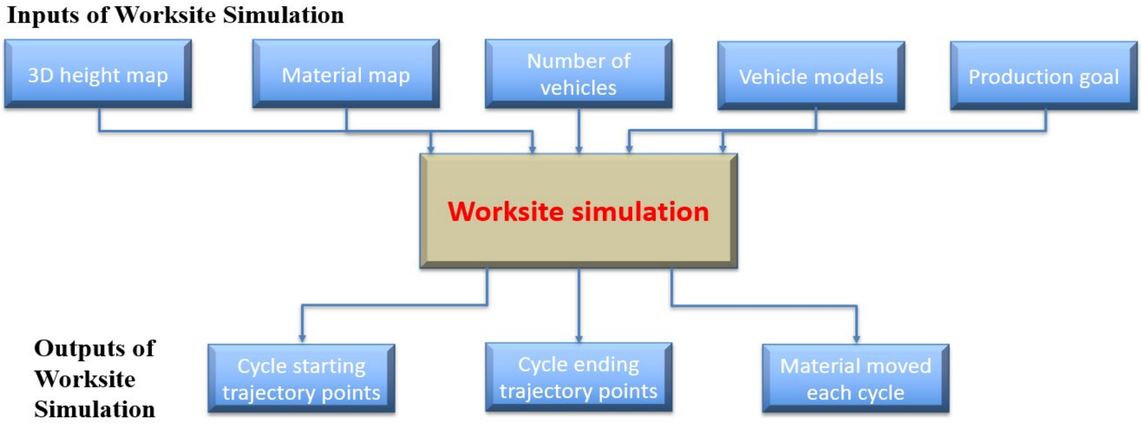

Figure 10: Flowchart overview of software IO

The worksite simulation requires several inputs, including a 3D terrain map, material distribution map, production goals, and vehicle details like types, models, and quantities. The software also considers various constraints such as maximum operating costs and operational length. These inputs help the software determine the best way to allocate and sequence the vehicle's movements across the site. For instance, it factors in the interaction between vehicles and different soil types to optimize vehicle paths and their performance during material loading or excavation. Additionally, the software accommodates variations in site conditions, such as weather changes, by considering the impact of soil properties on vehicle operations.

The outputs of the simulation include cycle trajectory starting and ending points for each vehicle, materials moved during each cycle, and a detailed breakdown of vehicle costs and movements. These outputs are essential for tracking the efficiency of each vehicle and the overall operation. By optimizing these factors, the software aims to minimize costs while meeting production targets, ensuring that site operations are both effective and economical.

2.1.4 Communication System Development

2.1.4.1 Communication System Overview

Communication systems are essential for enhancing the efficiency, safety, and automation of off-road vehicles, such as those used in construction and agricultural environments. In these contexts, it is critical for vehicles to communicate not only with each other (V2V) but also with remote control centers and infrastructure (V2I). This communication ensures that tasks are coordinated effectively, reducing human error, enhancing productivity, and potentially lowering operational costs. However, unlike on-road vehicles, research on communication systems for off-road vehicles remains limited. This study focuses on developing and testing a communication system that can reliably support real-time data exchange in off-road environments, where accurate, low-latency communication is vital.

Figure 11 illustrates the envisioned setup where a remote control center manages multiple off-road vehicles operating autonomously on a worksite. In this scenario, the communication between the vehicles and the control center must be seamless, with commands sent from the center and real-time data (such as vehicle speed and position) transmitted back. Additionally, the vehicles themselves need to exchange data during operations to ensure proper task coordination.

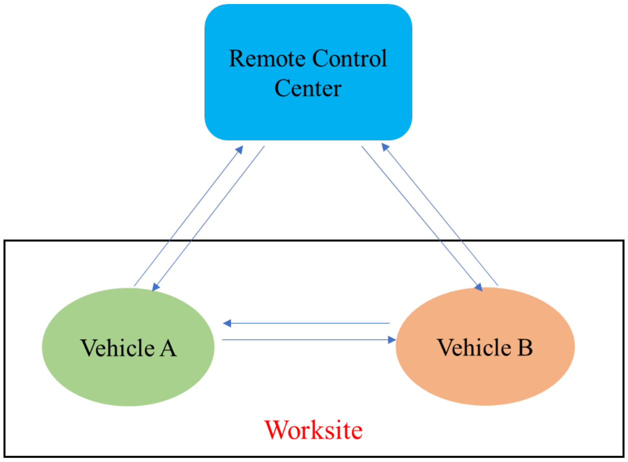

Figure 11. Background Setup

2.1.4.2 Demonstration Setup

The experiment was designed to test the communication system under realistic conditions, using a simulated demo setup. The demo aimed to evaluate the accuracy and latency of wireless communication between vehicles and a control center in off-road environments. The system architecture involves two computers: Computer A, which simulates machine data via CAN bus, and Computer B, which receives the data wirelessly.

Figure 12 shows the communication system test architecture used in the experiment. In this setup, Computer A generates CAN bus data to represent real vehicle data. The CAN bus data is transmitted through a Danfoss CS10 Wireless Gateway to Computer B, where it is analyzed. This setup was used to study the system's performance in terms of both message accuracy and communication latency. By varying the time intervals between messages and the physical distance between the two computers, the test aimed to determine how well the system could perform in real-world scenarios.

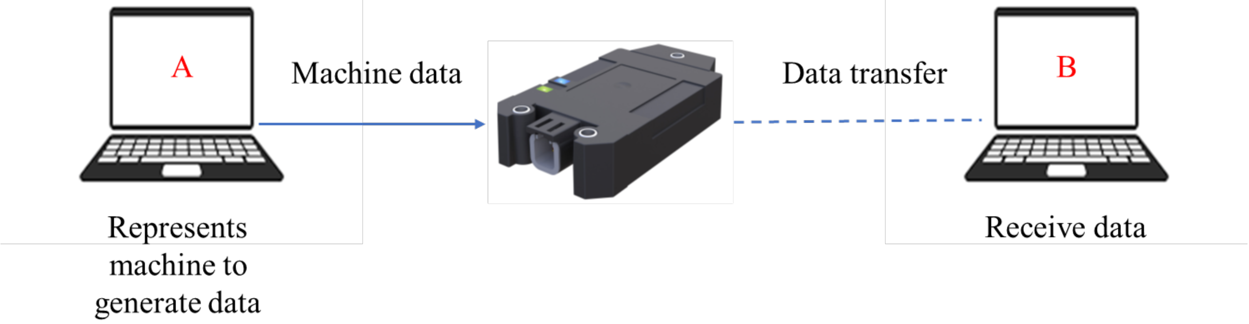

Figure 12. Communication System Test Architecture

2.1.4.3 Real Test Configuration

The actual test configuration incorporated real hardware and software to assess the performance of the communication system. In the test, Computer A was equipped with the Kvaser PCIEcan HS v2 to generate and transmit CAN bus messages through wiring to the Danfoss CS10 gateway. The wireless gateway then transmitted these messages to Computer B, where they were received and displayed using the PLUS+1 Service Tool software.

Figure 13 provides an overview of the real test setup, showing how the components were physically connected. The Kvaser PCIEcan was installed in Computer A, and the CAN bus was connected to the Danfoss CS10, which required an external power supply. The wireless transmission was then sent to Computer B, located at varying distances from Computer A, to assess how well the system could transmit and receive messages wirelessly.

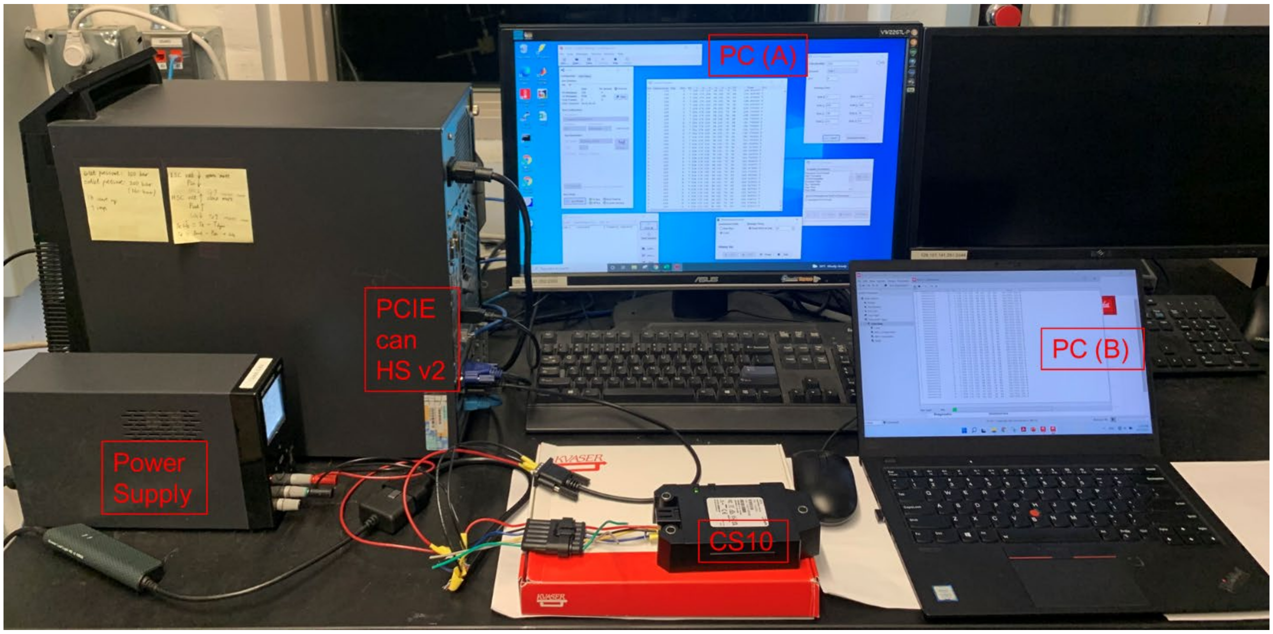

Figure 13. Real Configuration

2.1.4.4 Test Results and Conclusion

The experimental results showed that the communication system performed exceptionally well across all test conditions. Data transmission accuracy was 100% at both short (1 meter) and long (22 meters) distances, and the system consistently transmitted CAN bus messages with less than 100 milliseconds of latency, even when messages were sent every 1 millisecond. This high level of performance indicates that the Danfoss CS10 gateway is capable of handling the communication needs of off-road vehicles in real-time applications. With accurate and low-latency communication, this system could significantly improve the productivity and safety of autonomous vehicles operating in construction and agricultural environments.

2.2 Optimization

This part consists of the following optimization work:

I. Transport phase optimization
II. Bucket loading trajectory optimization
III. Combined cycle Optimization

2.2.1 Transport Phase Optimization

2.2.1.1 Technical Route

In our previous work, the full-order model of the wheel loader has been built and validated based on the CNH testing data. While this model provides an accurate representation of the system, it is too complex and high order for use in real-time optimization. Even the reduced order model remains complex enough to slow the optimization progress. Our technical route is to initialize the optimization work from a simplified model which can capture the basic characteristics of the wheel loader dynamics. The simplified model can be improved as the optimization progresses to capture more complicated features of the vehicle.

2.2.1.2 Simplified Model Dynamic Equations Formation

The simplified model dynamic equations will be presented in this section.

Engine Model

$$J\dot{\omega}_e = T_e - T_p - T_w - T_b \tag{29}$$

J := lumped inertia of engine and other three pumps ($kg \cdot m^2$)
ω_e := engine speed (rad/s)
T_e := engine torque ($N \cdot m$)
T_p := pump torque for the torque converter ($N \cdot m$)
T_ω := main hydraulic pump torque ($N \cdot m$)
T_b := brake pump torque ($N \cdot m$)

Note that: In this simplified model setting, the brake circuit torque T_b is assumed to be constant.
The detailed expression of each term of the right-hand side of equation (29) except for T_b is given as follows.

A. Engine Torque T_e

$$T_e = T_{ig} - T_{fric} \tag{30}$$

$$T_{ig} = 10^{-6} \frac{\eta_{ig} q_{hv} n_{cyl}}{4\pi} u_f \tag{31}$$

$$T_{fric} = 10^5 \frac{V_d}{4\pi} (C_{fr1}\omega_e^2 + C_{fr2}\omega_e + C_{fr3}) \tag{32}$$

T_{ig} := combustion generated torque ($N \cdot m$)
T_{fric} := engine friction torque ($N \cdot m$)
η_{ig} := combustion chamber efficiency
q_{hv} := heating value of diesel (J/kg);

n_{cy} := number of cylinders in engine
u_f := injected fuel per combustion cycle ($mg/cycle$)
V_d := engine displacement volume (m^3)
$C_{fr1}, C_{fr2}, C_{fr3}$:= engine friction coefficient determined by regression fitting

B. Torque Converter Pump Torque

$$T_p = a_1\omega_p^2 + a_2\omega_p\omega_t + a_3\omega_t^2 \tag{33}$$

$$\omega_t = 2.184\,\omega_f \tag{34}$$

$$\omega_p = \omega_e \tag{35}$$

ω_p := pump (engine) speed (rpm);
ω_t := turbine speed (rpm)
ω_f := final drive speed (rpm)
a_1, a_2, a_3 := coefficients determined by regression fitting;
Note that: In order to reduce the complexity of the transmission, we assume that the gear ratio is fixed in this simplified model.

C. Main hydraulic pump torque

$$T_w = \frac{m_{load}\,(g + u_p)v_l}{\omega_e\,\eta} \tag{36}$$

m_{load} := mass of the bucket (kg)
u_p := rod acceleration due to lift cylinder pressure (m/s^2)
v_l := lift cylinder velocity (m/s)
η := lift system efficiency
Note that: the complex dynamics of the hydraulic work circuit is ignored by using u_p directly as a control variable.

Driveline Model

$$(J_r + J_f)\,\dot{\omega}_f = T_{drive} - T_{load} - u_b \tag{37}$$

ω_f := final drive speed (rad/s)
J_r := inertia of drive shaft ($kg \cdot m^2$)
J_f := vehicle inertia on the final drive shaft ($kg \cdot m^2$)
u_b := braking torque ($N \cdot m$)
T_{drive} := drive torque ($N \cdot m$)
T_{load} := vehicle load torque ($N \cdot m$)

The expression of T_{drive} and T_{load} are given as follows.

$$T_{drive} = 2.184\,T_t \tag{38}$$

$$T_t = b_1\omega_p^2 + b_2\omega_p\omega_t + b_3\omega_t^2 \tag{39}$$

$$T_{load} = \frac{R_{wh}}{k_f}\mu m g \tag{40}$$

T_t := torque converter turbine torque ($N \cdot m$)

R_{wh} := wheel radius (m)
k_f := final drive ratio
μ := rolling friction coefficient of the wheels
m := total vehicle mass (kg)
b_1, b_2, b_3 := coefficients determined by regression fitting;

Vehicle Kinematic Model

$$\dot{x} = \frac{R_{wh}}{k_f} \omega_f \cos(\beta) \tag{41}$$

$$\dot{y} = \frac{R_{wh}}{k_f} \omega_f \sin(\beta) \tag{42}$$

R_{wh} := wheel radius (m)
k_f := final drive ratio
x, y := vehicle position coordinate (m)
ω_f := final drive speed (rad/s)
β := heading angle (rad)

Vehicle Steering Model

$$\dot{\beta} = 2 \frac{R_{wh}}{k_f} \omega_f \tan\left(\frac{\delta}{2}\right)/L \tag{43}$$

$$\dot{\delta} = u_s \tag{44}$$

R_{wh} := wheel radius (m)
k_f := final drive ratio
ω_f := final drive speed (rad/s)
δ := steering angle (rad)
L := wheelbase (m)
u_s := steering angle acceleration (rad/s^2)

Lifting Model

$$\dot{x}_l = v_l \tag{45}$$

$$\dot{v}_l = u_p \tag{46}$$

x_l := lift cylinder displacement (m)
v_l := lift cylinder velocity (m/s)
u_p := lift cylinder acceleration from pressure (m/s^2)

For convenience, the dynamic equations are considered in state-space form. The state vector is defined as

$$X \triangleq \left[\omega_e, \omega_f, x, y, \beta, \delta, x_l, v_l\right]^T \tag{47}$$

and the control vector is

$$U \triangleq \left[u_f, u_s, u_p, u_b\right]^T \tag{48}$$

2.2.1.3 Optimization Problem Definition

$$\min_{X,U} \left\{ \omega_1 \int_0^T dt + \omega_2 \int_0^T \dot{m}_f dt \right\} \tag{49}$$

$$\textbf{\textit{subject to}}: \quad \dot{X} = f(X) + g(X)\,U \tag{50}$$

$$\dot{m}_f = (10^{-6}/4\pi)\left(u_f \omega_e n_{cyl}\right) \tag{51}$$

$$X_{Lower\ Bound} \leq X \leq X_{Upper\ Bound} \tag{52}$$

$$U_{Lower\ Bound} \leq U \leq U_{Upper\ Bound} \tag{53}$$

$$h(X,U) \leq 0 \tag{54}$$

(50) represents our cost function with X, U as the optimization variables. (52) is the injected fuel mass per second. ω_1 and ω_2 in (50) are two nonnegative weights which provide flexibility to engineers or designers to decide the relative emphasis on minimizing time (productivity) or fuel consumption. (51) is the combination of (29), (37), (41), (42), (43), (44), (45), (46). (52) and (53) show the problem-oriented constraints which are based on the real limitations of the vehicle. (54) indicates the path constraints.

2.2.1.4 V-shape Transportation Trajectory Optimization

A V-shape transportation trajectory is generated via optimization, during which the bucket will be moved from a lower point to a higher position. The V-shaped transportation trajectory is a common part of the working cycle of a wheel loader. During the short loading cycle, the wheel loader digs out material from the stockpile, drives backward to the midpoint, then travels forward to the dump area (see Figure. 14).

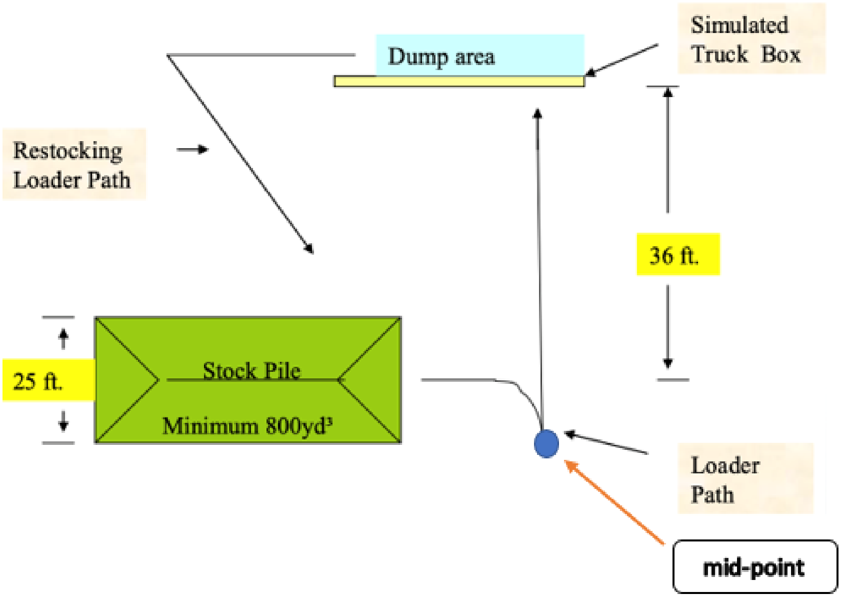

Figure 14: Schematic Diagram of Short Loading Cycle

2.2.1.5 Initial Conditions, Final Conditions and Constraints Setting

$$X_{initial} = [90, 0, -4, -12, \pi, 0, 0.1, 0]^T \tag{55}$$

$$X_{end} = [\sim, 0, 0, 0, \pi/2, \sim, 0.8, 0]^T \tag{56}$$

Note that the final conditions of ω_e and δ as well as the location of the midpoint will be determined by the optimization algorithm. In addition, we assume that the bucket takes $5000kg$ material from the stock pile.

The V-shape transportation will be divided into two parts: the first part is the phase from stock pile to midpoint with the vehicle traveling in reverse, and the second part is phase from the midpoint to dump area with the vehicle traveling forward. We will specify them separately.

From stockpile to midpoint:

$$X_{Lower\ Bound} = [90, -120, -4, \sim, \sim, -\pi/4, \sim, 0]^T \tag{57}$$

$$X_{Upper\ Bound} = [250, 0, 10, \sim, \sim, \pi/4, \sim, 5]^T \tag{58}$$

$$U_{LowerBound} = [0, -2, -5, 0]^T \tag{59}$$

$$U_{UpperBound} = [105, 2, 5,1500]^T \tag{60}$$

From midpoint to dump area:

$$X_{Lower\ Bound} = [90, 0, -4, \sim, \sim, -\pi/4, \sim, 0]^T \tag{61}$$

$$X_{Upper\ Bound} = [250, 100, 10, \sim, \sim, \pi/4, \sim, 5]^T \tag{62}$$

$$U_{LowerBound} = [0, -2, -5, 0]^T \tag{63}$$

$$U_{UpperBound} = [105, 2, 5,1500]^T \tag{64}$$

The only constraint at the midpoint is on the final drive speed, ω_f, which must to be zero, implying that the wheel loader is fully stopped at the midpoint to switch from driving in reverse to forward. We employ the solver OpenOCL to solve this optimization problem, in which the Interior-Point method for nonlinear programming is implemented.

2.2.1.6 Optimization Results and Analysis

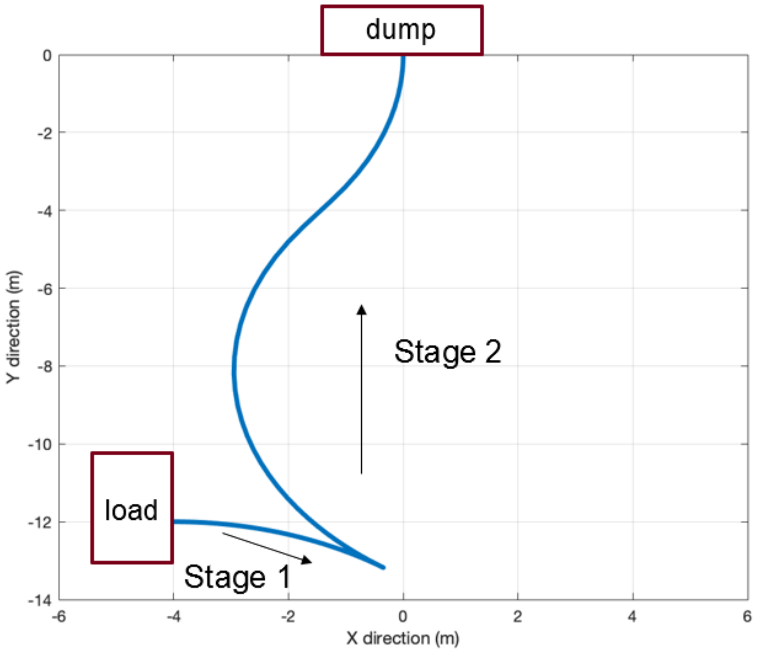

Figure 15. V-shaped Transportation Trajectory

Figure 15 shows the V-shaped transportation trajectory from loading position (stock pile) to dump position. The entire trajectory is generated by the optimization solver.

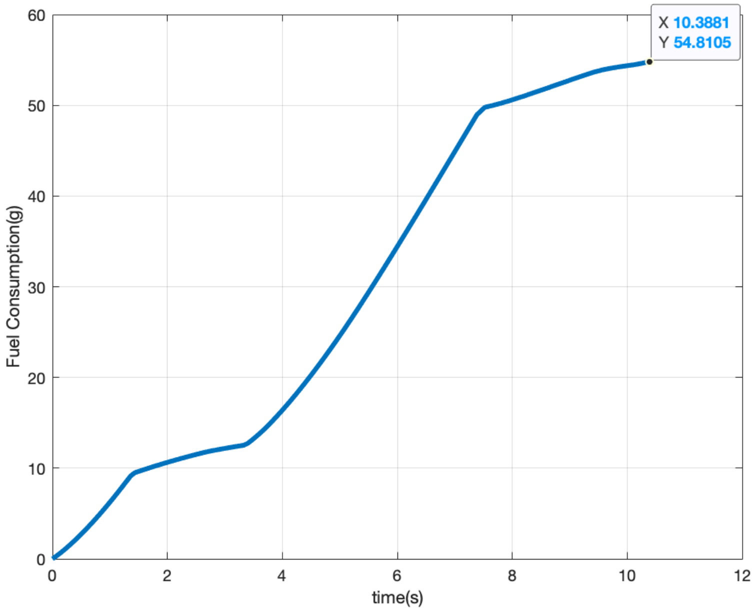

Figure 16. Fuel Consumption and Time

In this simulation, we set the weights ω_1 and ω_2 as 100 and 1, respectively. These weights place a heavy emphasis on time (productivity) relative to fuel consumption in order to compare results directly to human operators. Figure 16 shows that the total time is 10.3881 seconds, and the total fuel consumption is 54.8105 grams. Based on the provided CNH data, a professional human driver will take 10-11 seconds and around 80 grams fuel to complete the same transportation and bucket lifting phase. Compared with the optimal results, the time is similar with an almost 31% decrease in fuel consumed.

2.2.2 Bucket Loading Optimization

2.2.2.1 Formulation of Optimization Problem at Digging Phase

This part mainly focuses on the optimal trajectory planning the digging phase. As is well known, the digging phase is an integral part of the driving cycle for a wheel loader. This phase is an energy-intensive and highly variable process. Even for some professional human-drivers, it is hard to plan an optimal energy-saving digging trajectory. Proposing an optimal digging strategy from the perspective of the minimization of fuel consumption is of great benefit for the industries utilizing wheel loaders.

2.2.2.2 Mathematical Model Development

The principal challenge for the optimization design in the digging phase is that no valid digging phase model exists in the academic community that can be used for our purposes: To reflect not only the dynamic characteristics, but also be easily implemented by some existing nonlinear optimization techniques. In light of these considerations, our team propose a digging model for the purpose of energy optimization. Several assumptions are made as follows:

a. The coordinate frame is established as following figures. We assume that the bucket

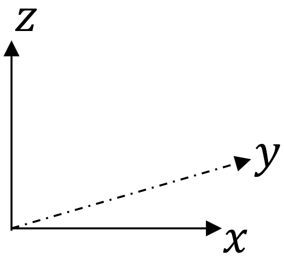

Figure 17. Coordinate Frame

can only move inside the x-z plane. There is no movement in y direction.

b. For convenient modeling, we consider the bucket tip alone to represent the movement of the whole bucket.

c. The vehicle is stationary during the digging phase.

Based on the practical motion of the bucket, we decompose its movement in the digging phase into rotational movement and translational movement. Let us consider the rotational movement first as shown in Figure 18, which indicates a bucket from the cross-sectional view.

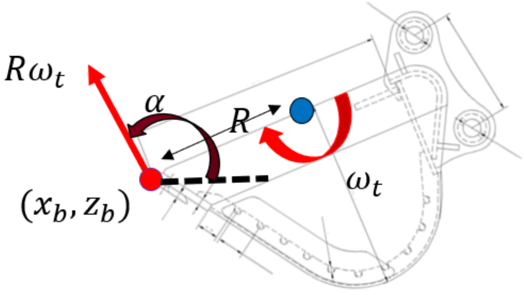

Figure 18. The Diagram of Rotation Movement

The red point is the tip of bucket. (x_b, z_b) is the x position and z position of the bucket tip within the coordinate frame x-z plane. The blue point represents the rotational axis of the bucket. Since it is the cross-sectional diagram, the axis is degenerated into a point. The distance from bucket tip to the axis of rotation is R. The orientation angle of the bucket is α with counterclockwise as the positive direction. Meanwhile, ω_t represent the rotational angular velocity. Correspondingly, the linear speed of the bucket tip due to rotation can be expressed as $R\omega_t$. From a physical perspective, ω_t is controlled by the tilt cylinder. As in the transportation phase, we employ u_t related to the tilt cylinder acceleration to avoid the complicated hydro-mechanical mechanism. The dynamic equations of this rotation movement can be formulated as:

$$\dot{\omega}_t = u_t \quad (65)$$

$$\dot{\alpha} = \omega_t \quad (66)$$

The next part is the translational movement of the bucket, which has been illustrated in Figure 19.

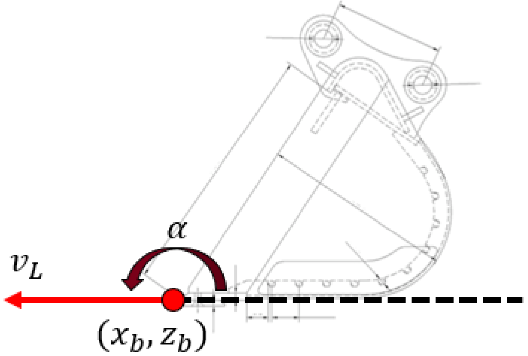

Figure 19. The Diagram of Translation Movement

In Figure 19, v_L represents the translational velocity of the bucket. For translational motion, we consider this movement to be driven by the lift cylinder. With the same logic as rotational motion, we take the lift acceleration u_p to control the translation speed v_L.

$$\dot{v}_L = u_p \quad (67)$$

The dynamic equations of the bucket position (x_b, z_b) are defined as follows.

$$\dot{x}_b = (v_L + R\omega_t) \cos \alpha \quad (68)$$

$$\dot{z}_b = (v_L + R\omega_t) \sin \alpha \quad (69)$$

The engine still provides all the energy for digging with its dynamics defined below.

$$J\dot{\omega}_e = T_e - T_p - T_w \quad (70)$$

where,
J := lumped inertia of engine and other three pumps $(kg \cdot m^2)$
ω_e := engine speed (rad/s)
T_e := engine torque $(N \cdot m)$
T_p := pump torque for the torque converter $(N \cdot m)$
T_ω := main hydraulic pump torque $(N \cdot m)$

The detailed expressions of the engine torque T_e, torque converter pump torque T_p, and main hydraulic pump torque T_w are stated as follows:

Engine Torque T_e

$$T_e = T_{ig} - T_{fric} \tag{71}$$

$$T_{ig} = 10^{-6} \frac{\eta_{ig} q_{hv} n_{cyl}}{4\pi} u_f \tag{72}$$

$$T_{fric} = 10^5 \frac{V_d}{4\pi} (C_{fr1}\omega_e^2 + C_{fr2}\omega_e + C_{fr3}) \tag{73}$$

T_{ig} := combustion generated torque ($N \cdot m$)
T_{fric} := engine friction torque ($N \cdot m$)
η_{ig} := combustion chamber efficiency
q_{hv} := heating value of diesel (J/kg);
n_{cy} := number of cylinders in engine
u_f := injected fuel per combustion cycle ($mg/cycle$)
V_d := engine displacement volume (m^3)
$C_{fr1}, C_{fr2}, C_{fr3}$:= engine friction coefficient determined by regression fitting.

Torque Converter Pump Torque T_p

$$T_p = a_1 \omega_p^2 \tag{74}$$

$$\omega_p = \omega_e \tag{75}$$

ω_p := pump (engine) speed (rpm);
ω_t := turbine speed (rpm)
a_1 := coefficients determined by regression fitting;

Main hydraulic pump torque T_w

$$T_w = \frac{F_{th}(v_L + R\omega_t)}{\omega_e \eta} + \frac{M_{load}(\mathrm{g} + u_p + R\,u_t)(v_L + R\omega_t)}{\omega_e \eta} \tag{76}$$

M_{load} := mass of the bucket including the materials in the bucket (kg)
$M_{load} = \rho * A * L$, where $\rho(kg/m^3)$ is the density of the material , $A(m^2)$ is the cross-sectional area of the bucket going through the stockpile and $L(m)$ is wedge lenght of the bucket.
u_p := rod acceleration due to lift cylinder pressure (m/s^2)
u_t := rod acceleration due to tilt cylinder pressure (m/s^2)
η := lift system efficiency
F_{th} := resistance force (N)

For convenience, the dynamic equations are considered in state-space form. The state vector is defined as

$$X \triangleq [\omega_e , v_L , \omega_t, \alpha, x_b, x_z]^T \tag{77}$$

and the control vector is

$$U \triangleq \left[u_f , u_p , u_t\right]^T \tag{78}$$

2.2.2.3 Optimization Problem Formulation

$$\min_{X,U}\left\{ \int_0^T \dot{m}_f dt \right\} \tag{79}$$

$$\textbf{\textit{subject to}}: \quad \dot{X} = f(X) + g(X)\,U \tag{80}$$

$$\dot{m}_f = (10^{-6}/4\pi)\left(u_f \omega_e n_{cyl}\right) \tag{81}$$

$$X_{Lower\ Bound} \leq X \leq X_{Upper\ Bound} \tag{82}$$

$$U_{Lower\ Bound} \leq U \leq U_{Upper\ Bound} \tag{83}$$

$$t \leq T_f \tag{84}$$

$$h(X,U) \leq 0 \tag{85}$$

(79) represents our cost function with X, U as the optimization variables. (81) is the injected fuel mass per second. (80) is the combination from (65) to (70). (82) and (83) show the problem-oriented constraints which are based on the real limitations of the vehicle. (84) implies that the whole digging operation should be completed at certain time T_f. (85) indicates the path constraints.

2.2.2.4 Digging Phase Trajectory Optimization

In order to simulate a realistic digging scenario, a parabola function will be employed to represent the stockpile. The vehicle is held stationary while digging. The bucket will start from some point at the edge the stockpile and will stop elsewhere at the boundary of the stockpile. The bucket is required to fill itself with a certain amount of material from the stockpile. The goal is to plan a trajectory with minimum fuel consumption and minimum time.

2.2.2.5 Initial Conditions, Final Conditions and Constraints Setting

$$X_{initial} = [95,0,0,0.75\pi,4,0]^T \tag{86}$$

$$X_{end} = [\sim,0,0,\sim,\sim,\sim]^T \tag{87}$$

Note that the final conditions of $\omega_e, \alpha, x_b, x_z$ will be determined by the optimization algorithm.

$$X_{Lower\ Bound} = [70,\ 0,-5,\ \pi/2,\ 0,\ 0]^T \tag{88}$$

$$X_{Upper\ Bound} = [250,\ 2,\ 5,\ \pi,\ 4,\ 3]^T \tag{89}$$

$$U_{LowerBound} = [0,-2,-5]^T \tag{90}$$

$$U_{UpperBound} = [105,\ 2,\ 5]^T \tag{91}$$

The first constraint is the cross-sectional area A should be greater or equal to 1 m^2. The second constraint is the final position of the bucket should be on the boundary of the stockpile. The third constraint is the total time should be less or equal then 3 seconds. Note that: after taking an analysis of CNH data and traditional resistance force model, out team realize that the accumulated material weight is the dominating part of resistance force. So, it is reasonable to set the resistance force as a constant with 15,000N to simplify the model. We employ the solver OpenOCL to solve this optimization problem, in which the Interior-Point method for nonlinear programming is implemented.

2.2.2.6 Optimization Results and Analysis

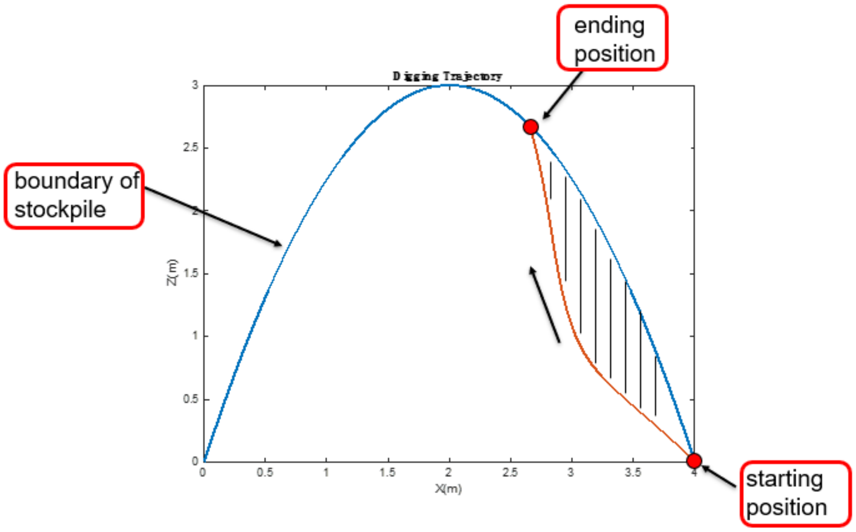

Figure 20. Digging Trajectory by Optimization Technique

Figure 20 shows the digging trajectory. The blue line represents the boundary of the stockpile. The bucket starting point is (4,0) m. The initial orientation angle of the bucket is $(0.75\pi)\ rad$. The ending point is not specified but is determined by the optimization algorithm with satisfaction of the bounds and constraints. The red line is the trajectory of the bucket. The shaded section is the cross-sectional area of material taken by the bucket. This area is the significant, since it will determine the productivity by how much material is transported by the wheel loader over a certain time. For the future work in the autonomous off-road wheel loader, we can accurately define this area depending on the volume of the bucket and the profile of the material piles.

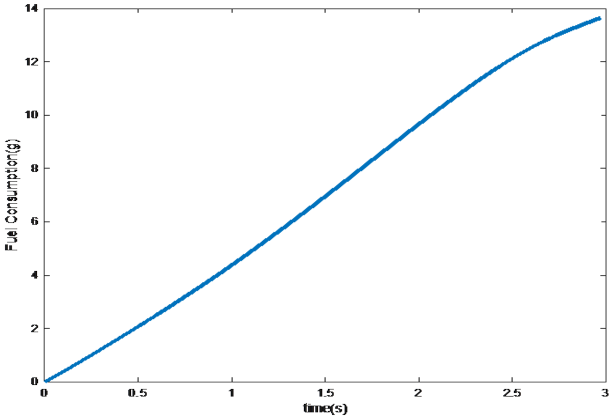

Figure 21: Fuel Consumption

Figure 21 shows the fuel consumption. At the end of the digging phase, total consumption is approximately 14g of fuel.

2.2.3 Combined Cycle Optimization

The goal of combined cycle optimization is to optimize the transport phase and digging phase together therefore more synergies between these phases can be leveraged.

2.2.3.1 Formulation of Combined Cycle Optimization Problem

The short loading cycle, also called the Y- or V-shape loading cycle, is a typical driving cycle used to test the performance of a wheel loader. The cycle generally consists of filling the bucket with some material from a pile, driving over to a truck or dump site to empty the bucket, and then driving back to the pile to repeat. Figure 22 shows a representation of this process. The dumping phase is not considered in this formulation because it is very short and contributes minimal fuel consumption relative to the other phases. Optimization of this combined cycle builds on the previous work of separately optimizing the bucket loading (digging) and the transport phases of this cycle. The combined optimization is created by combining several stages together, each with a slightly different set of constraints that represent a section of the cycle. By optimizing across the entire cycle at once, the algorithm can consider how each phase impacts the next one with the ability to plan ahead more effectively than a human driver. The optimal solutions to the separate phases from previous work can be combined to create an initial guess to "warm-start" the combined optimization solution.

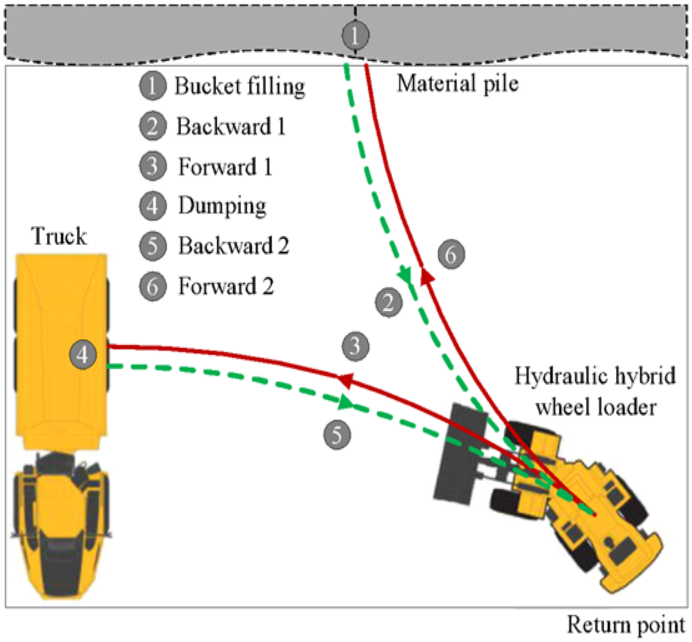

Figure 22. Schematic Diagram of the Short Loading Cycle

2.2.3.2 Control-oriented Model Development

The previous work on optimization of the transport and bucket-loading phases have already developed models for use in each phase separately. The different stages of the optimization can use different models depending on the relevant purpose. The transport stages need only consider the dynamics relevant to transport and bucket lifting, leaving out other bucket motion dynamics and interaction with the pile. Thus, the model used during the transport stages can remain essentially the same as in the separate transport optimization. The bucket-loading model; however, will require changes. Previously, it was assumed that the vehicle would remain stationary, using only the hydraulic cylinders to move and fill the bucket. To combine this phase with the transport phase, the model must be updated to include the vehicle motion.

(a). Transport Model

The model used during transport stages summarized in this section is the same as in previous work on the transport optimization. The lifting model is used only during the transport phase following bucket-loading, when the bucket must be lifted in preparation for dumping.

Engine Model

$$J\dot{\omega}_e = T_e - T_p - T_w - T_b \tag{92}$$

$$T_e = T_{ig} - T_{fric} \tag{93}$$

$$T_{ig} = 10^{-6}\frac{\eta_{ig} q_{hv} n_{cyl}}{4\pi} u_f \tag{94}$$

$$T_{fric} = 10^{5}\frac{V_d}{4\pi}(C_{fr1}\omega_e^2 + C_{fr2}\omega_e + C_{fr3}) \tag{95}$$

Driveline Model

$$\left(J_r + J_f\right)\dot{\omega}_f = T_{drive} - T_{load} - u_b \tag{96}$$

$$T_p = a_1\omega_p^2 + a_2\omega_p\omega_t + a_3\omega_t^2 \tag{97}$$

$$\omega_t = 2.184\,\omega_f \tag{98}$$

$$\omega_p = \omega_e \tag{99}$$

$$T_{drive} = 2.184\,T_t \tag{100}$$

$$T_t = b_1\omega_p^2 + b_2\omega_p\omega_t + b_3\omega_t^2 \tag{101}$$

$$T_{load} = \frac{R_{wh}}{k_f}\mu m g \tag{102}$$

Vehicle Kinematic Model

$$\dot{x} = \frac{R_{wh}}{k_f}\,\omega_f \cos(\beta) \tag{103}$$

$$\dot{y} = \frac{R_{wh}}{k_f}\,\omega_f \sin(\beta) \tag{104}$$

Vehicle Steering Model

$$\dot{\beta} = 2\,\frac{R_{wh}}{k_f}\omega_f \tan\left(\frac{\delta}{2}\right)/L \tag{105}$$

$$\dot{\delta} = u_s \tag{106}$$

Lifting Model

$$\dot{z}_b = v_l \tag{107}$$

$$\dot{v}_l = u_l \tag{108}$$

$$T_w = \frac{m_{load}\,(g + u_l)v_l}{\omega_e\,\eta} \tag{109}$$

(b). Bucket-Loading Model

Most of the model for this stage remains the same as in previous work. As before, the vehicle is assumed to operate only in the $x - z$ plane with no motion in the y direction. This means that the vehicle can only drive straight forward with no sideways steering. Because of this assumption, steering can be neglected while the vehicle motion is added.

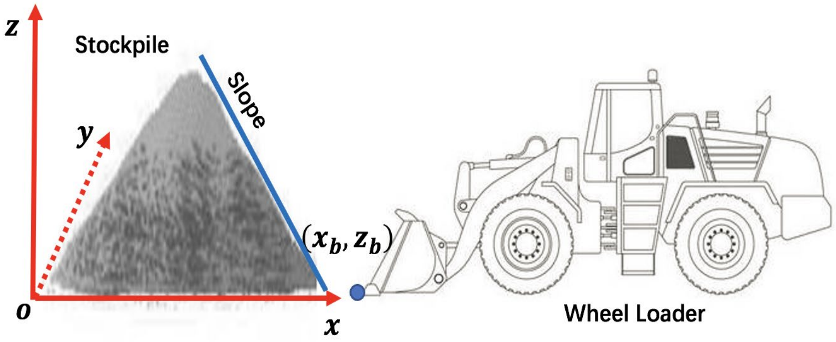

Figure 23. Bucket-loading Diagram

Powertrain Model:

To include vehicle motion during bucket-loading, the driveshaft dynamics are added back into the powertrain model. The engine model is the same as in the transport phase, using Eqs (92)-(95). Due to the interaction with the pile, the driveshaft dynamics from Eq (96) are altered to include the resistance that the pile exerts on the bucket as the vehicle drives into it:

$$\left(J_r + J_f\right)\dot{\omega}_f = T_{drive} - T_{load} - u_b - T_{res} \tag{110}$$

$$T_{res} = \frac{R_{wh}}{k_f}F^H \tag{111}$$

Eqs (97)-(101) still apply for the other terms. The vehicle kinematic model uses Eq (103) with a constant heading angle β of π or 180°, which will also make the y dynamics of Eq (104) be zero.

Bucket Motion Model:

Only one small change to the bucket motion model is required to couple its motion with that of the vehicle. As the wheel loader drives forward, the horizontal bucket position changes at the same rate, which can be written as:

$$\dot{x}_b = (v_l + r\omega_t cos\Theta)\cos\varphi + r\omega_t sin\Theta\sin(\pi - \varphi) + \frac{R_{wh}}{k_f}\,\omega_f \tag{112}$$

This is simply adding the vehicle motion onto the relative bucket motion to get the absolute bucket motion as the vehicle moves. If the vehicle remains stationary, ω_f will be zero and the bucket motion will be the same as in the previous bucket-loading optimization. The rest of the bucket motion model, summarized below, is the same as before.

$$\dot{\varphi} = \omega_t \tag{113}$$

$$\dot{\omega}_t = u_t \tag{114}$$

$$\dot{v}_l = u_l \tag{115}$$

$$\dot{z}_b = (v_l + r\omega_t cos\Theta)\sin\varphi + r\omega_t sin\Theta\cos(\pi - \varphi) \tag{116}$$

$$T_w = \frac{\left(F^H + m_b g sin(\pi - \Theta)\right)(v_L + r\omega_t cos\Theta) + \left(F^N + m_b g cos(\pi - \Theta)\right)(r\omega_t sin\Theta)}{\eta\omega_e} \tag{117}$$

The pile resistance forces F^H and F^N are found using the FEE model as described in previous reports.

2.2.3.3 Optimization Problem Formulation

Each stage of the combined optimization is formulated with its own cost function and set of constraints:

$$\min_{X,U}\left\{\frac{\omega_1}{T_{human}}\int_0^T dt + \frac{\omega_2}{m_{f,human}}\int_0^T \dot{m}_f dt\right\} \tag{118}$$

subject to :

$$\dot{X} = f(X) + g(X)\,U \tag{119}$$

$$\dot{m}_f = (10^{-6}/4\pi)\left(u_f\omega_e n_{cyl}\right) \tag{120}$$

$$X_{Lower\ Bound} \leq X \leq X_{Upper\ Bound} \tag{121}$$

$$U_{Lower\ Bound} \leq U \leq U_{Upper\ Bound} \tag{122}$$

$$X(0) = X_0 \tag{123}$$

$$X(T) = X_f \tag{124}$$

$$h\left(X_f\right) = 0 \tag{125}$$

Eq. (118) represents our cost function with X, U as the optimization variables. The weights ω_1 and ω_2 determine the relative emphasis on productivity and fuel savings. The values in the cost function are normalized against a typical human driving cycle. Eq. (120) is the injected fuel mass per second. Eq. (119) is a combination of equations from Eq. (92) to Eq. (117) for the relevant stage. Eq. (121) and Eq. (122) show the problem-oriented constraints which are based on the real limitations of the vehicle. Eq. (123)

and (124) is the initial and final condition. Eq. (125) is the final state constraint, used only during the final bucket-loading stage to guarantee that the bucket tip reaches the edge of the pile. These constraints will be given in more detail in the next section.

The optimization problem is divided into six stages:

1. Transport Reverse 1
2. Transport Forward 1
3. Bucket Loading 1
4. Bucket Loading 2
5. Transport Reverse 2
6. Transport Forward 2

The first set of transport stages have no bucket motion while approaching the pile. The first bucket loading stage is essentially a transition from transport into bucket loading, which includes some vehicle motion driving into the pile to begin filling. The second bucket loading stage does not include vehicle motion, returning to the stationary bucket filling from the previous work. This assumes that the optimal trajectory for filling the bucket involves first driving into the pile, reducing vehicle speed to zero, and then remaining stationary while the bucket loading is finished. The bucket loading is divided in this way so that the resistance force applied to the drivetrain through the bucket (see Eq (111)) can be set to zero when the vehicle is stationary. The final pair of transport stages includes the bucket lifting to prepare for dumping.

2.2.3.4 Initial Conditions, Final Conditions, and Constraints Setting

Initial and final conditions for each stage of the optimization are selected to craft the desired short loading cycle. Other state and control constraints are used to limit the algorithm to operate within the vehicle's limitations. Each of the following subsections will detail the state (X) and control (U) variables, their constraints, and the initial and final conditions for each stage. The initial condition for a state in any stage must align with the final condition for that state in the previous stage to ensure continuity. Only the conditions specified when formulating the problem will be listed here, but any blank condition is still constrained to match between consecutive stages. The unspecified initial and final conditions provide the value of combining the optimization of these stages together: the algorithm is able to choose the optimal values for these conditions when connecting the stages.

(a) Transport Reverse 1

The vehicle starts facing the dump site and reverses to an unspecified midpoint, where it stops and shifts to drive forward. The only requirement to finish this stage is coming to a complete stop.

State and control variables:

$$X = \left[\omega_e, \omega_f, x, y, \beta, \delta\right]^T \tag{126}$$

$$U = \left[u_f, u_b, u_s\right]^T \tag{127}$$

State and control constraints:

$$X_{max} = \left[220, 100, \sim, \sim, \sim, \frac{2}{9}\pi\right]^T \tag{128}$$

$$U_{min} = \left[115, 2200, \frac{5}{36}\pi\right]^T \tag{129}$$

$$X_{max} = \left[90, 0, \sim, \sim, \sim, -\frac{2}{9}\pi\right]^T \tag{130}$$

$$U_{min} = \left[15, 0, -\frac{5}{36}\pi\right]^T \tag{131}$$

Initial and final conditions:

$$X_0 = \left[120, 0, 0, 0, \frac{\pi}{2}, 0\right]^T \tag{132}$$

$$X_f = [\sim, 0, \sim, \sim, \sim, \sim]^T \tag{133}$$

(b) Transport Forward 1

The vehicle from where it finished the previous stage and drives to the edge of the pile, facing directly into it horizontally.

State and control variables:

$$X = \left[\omega_e, \omega_f, x, y, \beta, \delta\right]^T \tag{134}$$

$$U = \left[u_f, u_b, u_s\right]^T \tag{135}$$

State and control constraints:

$$X_{max} = \left[220, 100, \sim, \sim, \sim, \frac{2}{9}\pi\right]^T \tag{136}$$

$$U_{min} = \left[115, 2200, \frac{5}{36}\pi\right]^T \tag{137}$$

$$X_{max} = \left[90, 0, \sim, \sim, \sim, -\frac{2}{9}\pi\right]^T \tag{138}$$

$$U_{min} = \left[15,0, -\frac{5}{36}\pi\right]^T \tag{139}$$

Initial and final conditions:

$$X_0 = [\sim, 0, \sim, \sim, \sim, \sim]^T \tag{140}$$

$$X_f = [\sim, \sim, -4, -11, \pi, 0]^T \tag{141}$$

(c) Bucket Loading 1

The vehicle drives into the pile and begins filling the bucket until it comes to a stop.

State and control variables:

$$X = \left[\omega_e, \omega_f, x, x_b, z_b, v_l, \omega_t, \varphi, A\right]^T \tag{142}$$

$$U = \left[u_f, u_b, u_l, u_t\right]^T \tag{143}$$

State and control constraints:

$$X_{max} = [220, 100, \sim, \sim, \sim,1,1, \pi, 2]^T \tag{144}$$

$$U_{min} = [115, 2200,1,1]^T \tag{145}$$

$$X_{max} = \left[90, 0, \sim, \sim, \sim,0, -1, \frac{\pi}{2}, 0\right]^T \tag{146}$$

$$U_{min} = [15,0, -1, -1]^T \tag{147}$$

Initial and final conditions:

$$X_0 = [\sim, \sim, -4, -4, 0, 0, 0, \pi, 0]^T \tag{148}$$
$$X_f = [\sim, 0, \sim, \sim, \sim, \sim, \sim, \sim, \sim]^T \tag{149}$$

(d) Bucket Loading 2
The vehicle remains stationary while it finishes digging.

State and control variables:

$$X = [\omega_e, x_b, z_b, v_l, \omega_t, \varphi, A]^T \tag{150}$$
$$U = \left[u_f, u_l, u_t\right]^T \tag{151}$$

State and control constraints:

$$X_{max} = [220, \sim, \sim,1,1, \pi, 2]^T \tag{152}$$
$$U_{min} = [115,1,1]^T \tag{153}$$
$$X_{max} = \left[90, \sim, \sim,0, -1, \frac{\pi}{2}, 0\right]^T \tag{154}$$
$$U_{min} = [15, -1, -1]^T \tag{155}$$

Initial and final conditions:

$$X_0 = [\sim, \sim, \sim, \sim, \sim, \sim, \sim]^T \tag{156}$$
$$X_f = [\sim, \sim, \sim, \sim,0, \sim,1]^T \tag{157}$$

This stage also has a terminal constraint, Eq (125), that is a function of (x_b, z_b) and the pile geometry which forces the bucket tip to reach the edge of the pile as the bucket loading finishes. The same constraint was used in the prior work on bucket loading optimization.

(e) Transport Reverse 2
The vehicle starts facing the dump site and reverses to an unspecified midpoint, where it stops and shifts to drive forward. The only requirement to finish this stage is coming to a complete stop.

State and control variables:

$$X = \left[\omega_e, \omega_f, x, y, \beta, \delta, x_b, v_l\right]^T \tag{158}$$
$$U = \left[u_f, u_b, u_s, u_l\right]^T \tag{159}$$

State and control constraints:

$$X_{max} = \left[220, 100, \sim, \sim, \sim, \frac{2}{9}\pi, \sim,1\right]^T \tag{160}$$
$$U_{min} = \left[115, 2200, \frac{5}{36}\pi, 1\right]^T \tag{161}$$
$$X_{max} = \left[90, 0, \sim, \sim, \sim, -\frac{2}{9}\pi\right]^T \tag{162}$$
$$U_{min} = \left[15, 0, -\frac{5}{36}\pi, 0\right]^T \tag{163}$$

Initial and final conditions:

$$X_0 = [\sim, 0, -4, -11, \pi, 0, \sim, \sim]^T \tag{164}$$
$$X_f = [\sim, 0, \sim, \sim, \sim, \sim, \sim, \sim]^T \tag{165}$$

(f) Transport Forward 2

The vehicle starts facing the dump site and reverses to an unspecified midpoint, where it stops and shifts to drive forward. The only requirement to finish this stage is coming to a complete stop.

State and control variables:

$$X = \left[\omega_e, \omega_f, x, y, \beta, \delta, x_b, v_l\right]^T \tag{166}$$

$$U = \left[u_f, u_b, u_s, u_l\right]^T \tag{167}$$

State and control constraints:

$$X_{max} = \left[220, 100, \sim, \sim, \sim, \frac{2}{9}\pi, \sim, 1\right]^T \tag{168}$$

$$U_{min} = \left[115, 2200, \frac{5}{36}\pi, 1\right]^T \tag{169}$$

$$X_{max} = \left[90, 0, \sim, \sim, \sim, -\frac{2}{9}\pi\right]^T \tag{170}$$

$$U_{min} = \left[15, 0, -\frac{5}{36}\pi, 0\right]^T \tag{171}$$

Initial and final conditions:

$$X_0 = [\sim, 0, \sim, \sim, \sim, \sim, \sim, \sim]^T \tag{172}$$

$$X_f = \left[120, 0, 0, 0, \frac{\pi}{2}, 0, 5, 0\right]^T \tag{173}$$

The final conditions for this stage are the same as the initial conditions for the Transport Reverse 1 stage to complete the cycle. The bucket is also fully lifted in preparation for dumping.

2.2.3.5 Optimization Results and Analysis

The analysis from the previous transport optimization and bucket loading optimization still generally applies to these combined results within each stage. The main contribution of combined optimization is in freeing the transition conditions between stages, which allows for additional savings. The analysis in this report will focus on these new findings taken from the combined optimization.

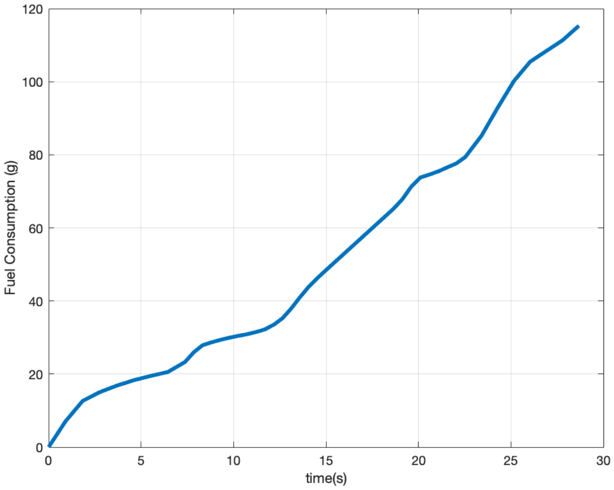

Figure 24. Fuel Consumption

The optimal solution takes 29.6 seconds and consumes 115.3 grams of fuel. The average human driver takes around 30 seconds and 200 grams of fuel to perform the same cycle, so the optimal solution represents 42% fuel savings with similar productivity. This set of results is using cost function weights of $\omega_1 = 0.35$ on time and $\omega_1 = 0.65$ on fuel mass, which were chosen to give a cycle that takes a similar amount of time as a human driver. This optimization problem also takes 21 seconds to solve, with is 71% of the cycle time.

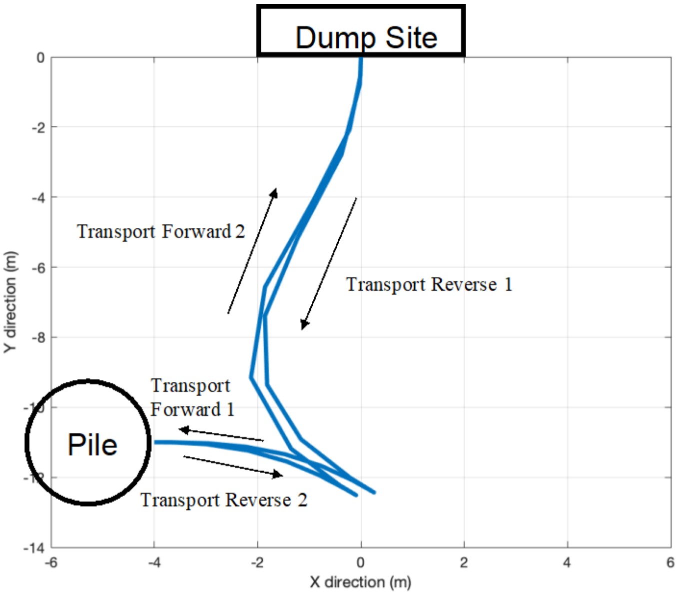

Figure 25. V-Shaped Transportation Trajectories

The two V-shape transport trajectories are shown in Figure 25. The first pair of transport stages go from the dump site to the pile, with the second pair reversing that process while lifting the bucket. The steering remains aggressive as before, since it shortens the distance traveled and benefits both productivity and fuel savings.

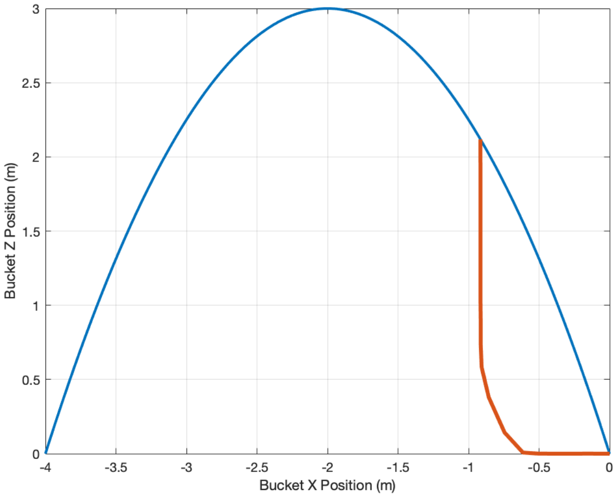

Figure 26. Bucket Loading Trajectory

Figure 26 shows the optimal trajectory for the bucket tip during the bucket loading stages. The initial angle of the bucket was set to be flat, so the bucket plunges straight into the pile before curving up to exit almost vertically once the bucket is filled. The main difference between this trajectory and the previous bucket loading optimization is the inclusion of vehicle motion, which leads to a flatter trajectory early on before a sharper exit.

3. HIL Testbed Development

Hardware-in-the-Loop testing is a method that connects a physical system or component to a virtual model, allowing for real-time interaction between the physical system and the virtual model. It has been widely used in various applications, including automotive, aerospace, renewable energy, etc. The method is cost-efficient, safe, and rapid prototyping for research and development work. Through this project, we have built a hardware-in-the-loop testbed for off-road vehicles. It can be used to evaluate the energy benefits of the automated wheel loader.

3.1 HIL Testbed Design

The overall architecture of the HIL testbed is shown in Figure 27. The two blue blocks are actual hardware, a real diesel engine, and a hydrostatic dynamometer. The blocks in orange indicate various controllers and mathematical models, including planning algorithms, vehicle models, and all necessary controllers. The HIL testbed is operated by using the three-level control structure. According to this structure, the engine can emulate the operating points of the real wheel loader carrying out loading cycles.

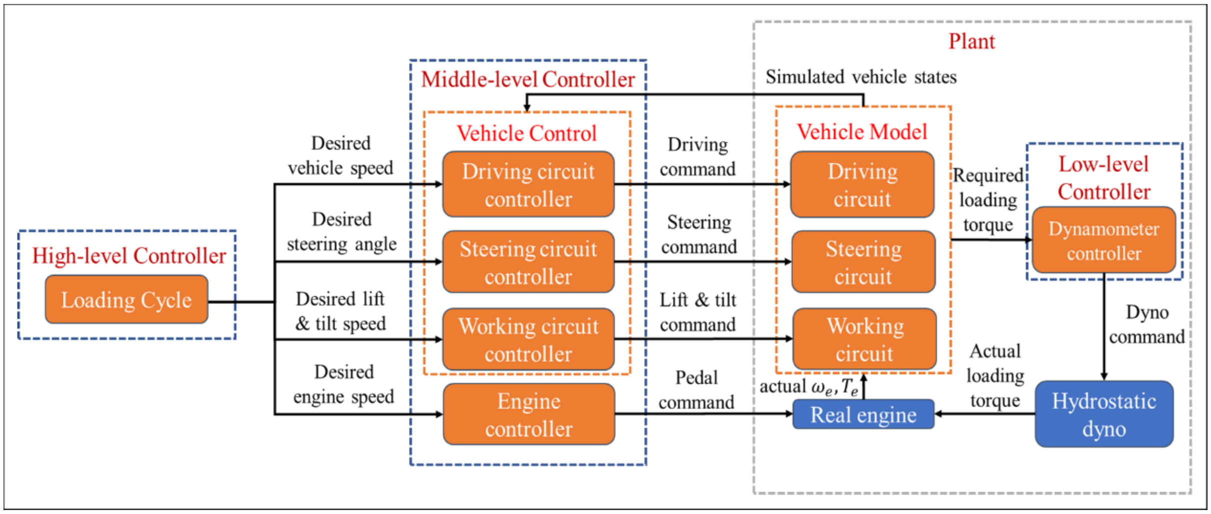

Figure 27. The overall architecture of the HIL testbed

(1) High-level controller. The high-level controller is used to produce the wheel loader operation motion profiles. Usually, it is called the loading cycle, including vehicle speed, steering angle, lift and tilt speed, and engine speed.

(2) Middle-level controller. The middle-level controller is used to automate the wheel loader operation. The driving controller is used to achieve the desired vehicle speed. The steering controller is to realize the desired steering angle. The working circuit controller is used to achieve the desired lift and tilt speed. The engine controller is used to realize the desired engine speed.

(3) Low-level controller. The low-level controller is used to achieve the desired load torque from the vehicle model, and it controls the hydrostatic dynamometer to output the load torque to the real engine.

3.1.1 HIL Testbed Design Overview

Figure 28 shows the overview of the HIL testbed. In the test room, the engine from an actual wheel loader is installed. All the necessary components of the engine are installed as well, including the engine electronic control unit, after-treatment system, smart fuse box, and universal control module. The fuel is supplied by AVL fuel measurement system with a fuel supply tank. The engine cooling system is customized to cool the engine. A transient hydrostatic dynamometer is adopted to load or motor the engine. The hydraulic oil is supplied by a variable displacement pump driven by a fixed-speed electric motor. A loading-sensing feedback strategy is adopted to control the inlet pressure of the engine loading pump/motor. A high-speed control valve (HSC) is used to change the outlet pressure of the engine loading pump/motor. The displacement of the engine loading pump/motor is kept constant during most operations due to the low bandwidth. A real-time controller is used to send the control commands and receive the measurement signals. The measurement mainly includes the inlet and outlet pressure of the engine loading pump/motor, The load torque and engine speed, the fuel rate, etc.

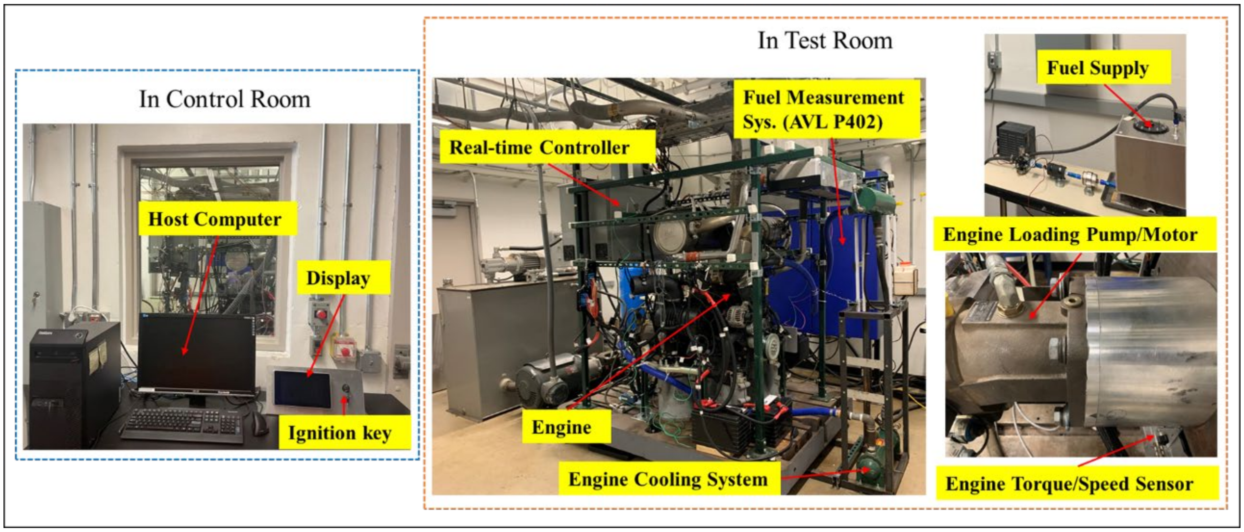

Figure 28. Overview of HIL testbed setting

In the control room, the host computer is equipped with MATLAB/Simulink, which allows it to interact with the real-time controller in the test room. It can send control signals including engine pedal commands for controlling the engine speed, HSC commands for controlling the outlet pressure of the engine loading pump/motor, etc.

The HIL testbed is shown in Figure 29. DYNO represents the hydrostatic dynamometer system and accessories. UEI represents the control system. ENGINE represents the test engine.

Figure 29. HIL Test Platform

3.1.2 Dynamometer

The dynamometer (dyno) is an important part of HIL test platform, as shown in Figure 30. The main hydrulic componetns include: a boost pump and an engine load (EL) pump/motor (both are variable displacement piston pumps), a load-sensing control (LSC) valve (proportional valve), and a high-speed control (HSC) valve (two-stage valve, shown in the bottom right corner of Figure 30).

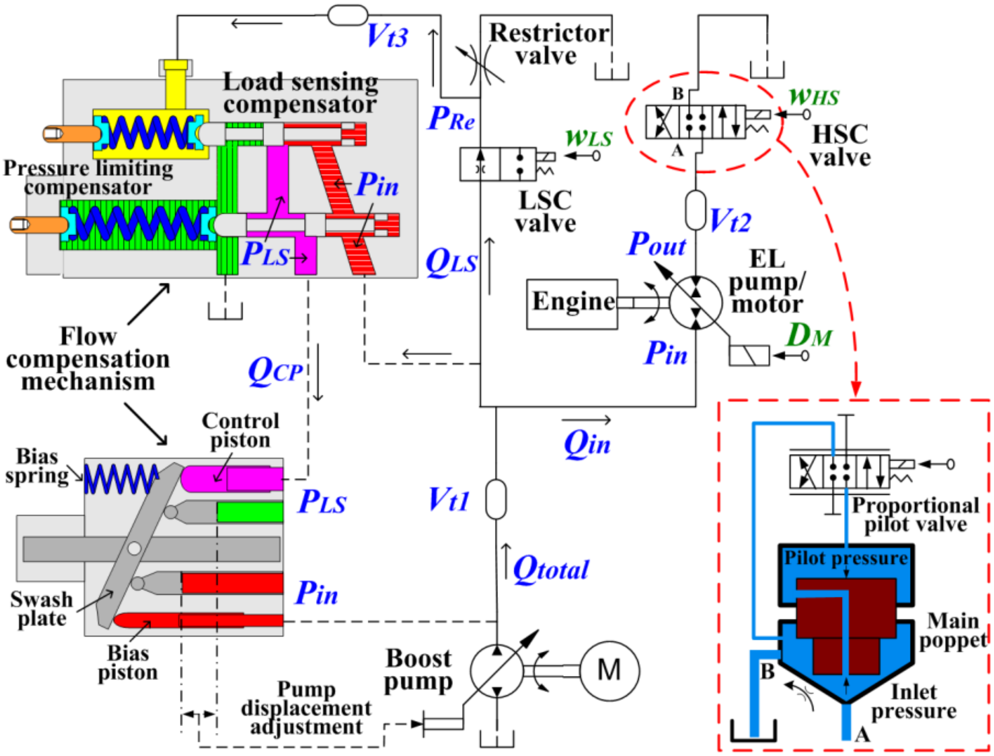

Figure 30. Architecture of the dynamometer for the HIL Test Platform

As shown in figure 30, the hydraulic system consists of one fluid supply and two loops: the engine loading and motoring loop and loading sensing feedback loop. Powered by an electrical motor, the boost pump provides fluid for both loops. The majority of the fluid enters the main loop as the engine load, while a small portion of the fluid flows into the feedback loop to generate a feedback pressure for the boost pump displacement control.

In the load sensing feedback loop, the LSC valve generated a proper feedback pressure as an input to the flow compensation mechanism. It can adjust the swashplate angle to regulate the boost pump displacement to ensure that the supplied fluid meets the engine demand and regulate the inlet pressure of the EL pump/motor.

In the engine loading/motoring loop, the HSC valve controls the outlet pressure of the EL pump/motor, while the displacement adjustment mechanism controls the displacement of the EL pump/motor. Since the dynamometer torque is a function of the displacement and pressure drop, we can manipulate the dynamometer torque to “counteract” the engine torque by controlling the above actuators and further, drive the engine to precisely track the desired speed profile.

Experimental results from previous test engines demonstrate precise tracking performance with less than 5% tracking error for transient and steady-state operations.

3.1.3 Engine

The engine model is used with latest technology HI-eSCR (DOC+SCR) to satisfy Tier 4B emissions. The new and unique Electronic Control Unit (ECU) is programmed to provide in real time a wide range of power and torque curves, according with optimized throttle. Moreover, the controller manages all procedures of emission reduction through the new ATS (After Treatment System) via CAN Bus J1939.

3.1.3.1 Mechanical Connection Design

The connection between engine and hydraulic pump/motor is critical in the test platform construction. In the case of high-speed rotation, if it is not concentric, it is easy to cause damage to the engine and hydraulic pump/motor. Hence, designing the flywheel coupler is central to the mechanical connection. The diagram for the mechanical connection is shown in Figure 31.

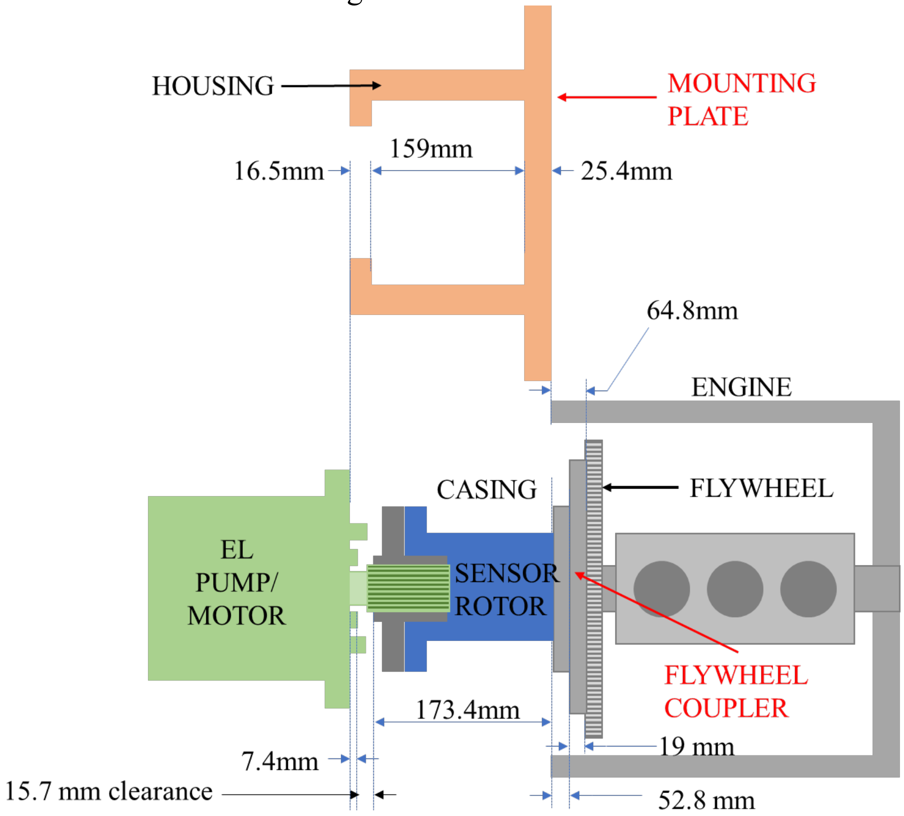

Figure 31. Mechanical Connection Diagram

The flywheel coupler and mounting plate was designed to achieve the goal. The mechanical connection is shown in the figure below.

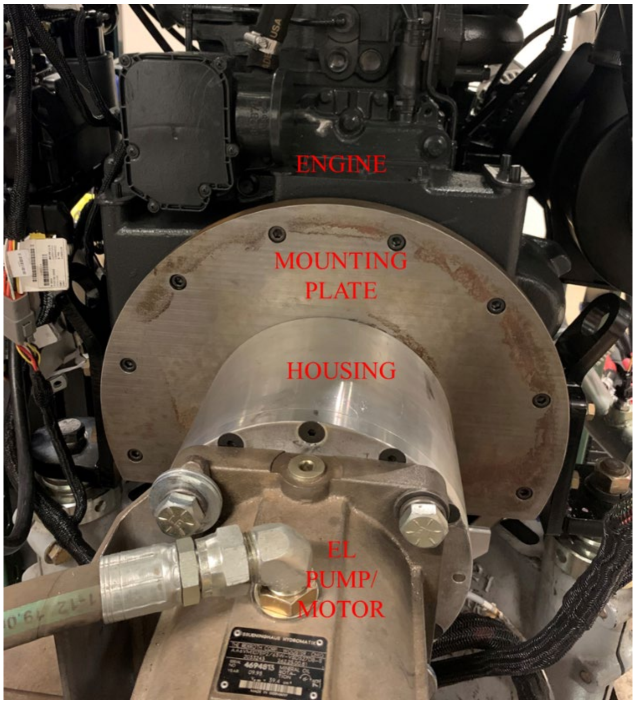

Figure 32. Mechanical Connection

3.1.3.2 Fuel Supply and Measurement System

Fuel is supplied by a pump and measured using an AVL FuelExact PLU P402 Fuel Measurement System (FMS). The unit is designed for transient applications. It has an internal data rate of 20 Hz. Fuel is measured using a positive displacement theory. A photo of the fuel supply and measurement system can be seen in Figure 33.

Figure 33. Fuel Supply and Measurement System

3.1.3.3 Engine Cooling System

The engine cooling system is critical to the engine. In test cell, we use the building's water supply to absorb heat from the coolant, which is more efficient than using viscous pusher fan and radiator in the real machine. It is shown in Figure 34. Therefore, the engine coolant temperature can be well controlled.

Figure 34. Engine Cooling System in Test Cell

3.1.3.4 After Treatment System

After treatment system includes Diesel Oxidation Catalyst (DOC), DEF dosing module, Selective Catalytic Reduction (SCR) catalyst, DEF supply module, DEF tank and a branch of sensors, like temperature sensors, NO_x sensors and NH_3 sensor. Diesel Oxidation Catalyst (DOC) oxidizes hydro-carbons (HC) and carbon monoxide (CO) to water vapor and carbon dioxide (CO_2), and converts part of the NO to NO_2. Then, the dosing module injects DEF/ADBLUE ($CO(NH_2)_2$), whose hydrolysis generates ammonia NH_3.

The dosing module is integrated in the outlet area of the DOC canister and injects into the exhaust stream the precise amount of the reduction agent DEF/ADBLUE required for the chemical reaction in the SCR catalytic converter. The dosing valve is Pulse Width Modulation (PWM) controlled by the ECU. The ECU determines the amount of DEF/ADBLUE fluid to inject based on inputs from sensors in the exhaust stream. Pressurized DEF/ADBLUE fluid is supplied to the dosing module from the supply module.
The main reaction involved in the Selective Catalytic Reduction (SCR) catalyst is the conversion of the NO_x to N_2 and H_2O. An average NO_2/NO_x ratio around 50% is required to give the optimum NO_x reduction efficiency in the exhaust system. Excess of ammonia (NH_3) is often used to facilitate the NO_x reduction to nitrogen, resulting in NH_3 slip. This ammonia must be removed by a secondary step in the Clean Up Catalyst (CUC). Temperature is very important to the chemical reactions that take place in the emission control system.

The Clean Up Catalyst converts the ammonia (NH_3) slip to nitrogen (N_2) and water vapor (H_2O). The CUC ensures that the ammonia slip to ambient is minimal.

The after treatment system setting in test cell is shown in Figure 35.

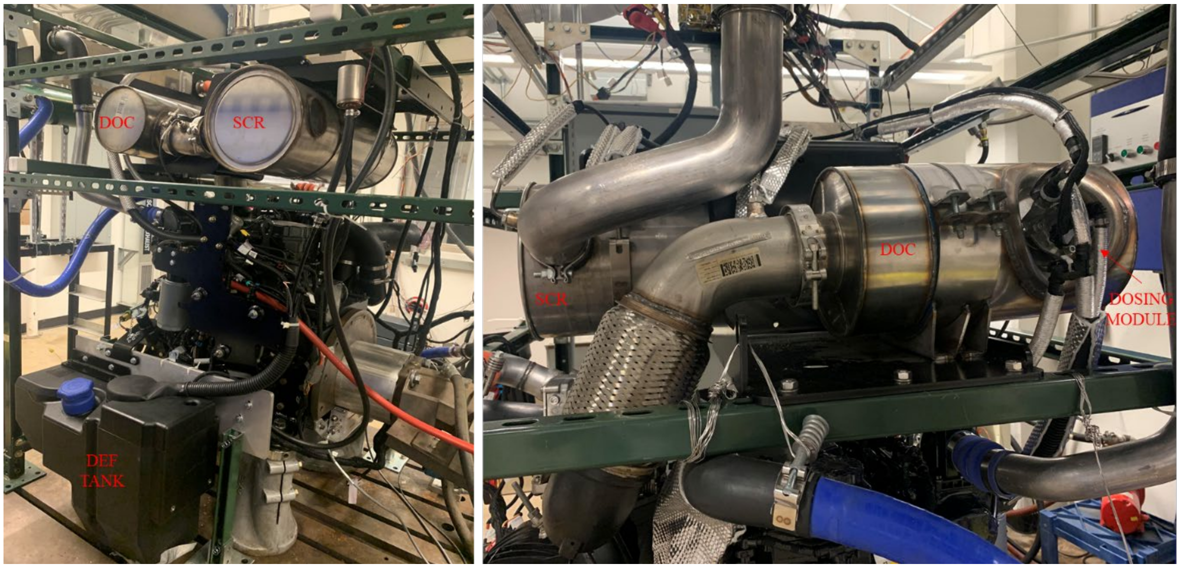

Figure 35. After Treatment System in Test Cell

3.1.3.5 Electrical Harness to Engine

CNH provided a standard wiring harness typically used on an off-road vehicle. The harness is connected from the engine electronic control unit (ECU) to all of the sensors on the engine and is responsible for sending the signals that control the cab, engine, transmission, and after treatment systems. They also provide UCM, SFB, ignition key, transmission shifter, display, switch pad, etc. Adapting the commercial harness and hardware to the test stand proved a daunting task because there were many excess terminals and each had to be identified prior to connection.

To start the engine by our hydraulic system, we need to figure out engine starting principle. All components involved in the starting circuit are in Figure 36. When the key switch is turned to the crank position, the Smart Fuse Box (SFB) receives the signal. Then the SFB sends a voltage signal entering the Universal Control Module (UCM). Then UCM will past along a “crank request” signal to the engine controller (ECU). And if the transmission in neutral, it will send voltage to the latch of the control relay in load center 6. This will be used to send voltage into the stater relay once the crank control relay has been activated.

The engine controller (ECU) receives a “OK to start from the vehicle (UCM)”. The engine will provide ground and power to the “Crank Control” relay in load center 6. Once the coil of the crank coil relay is activated, its latch will close and allow power through the relay onto the coil of the starter relay. This will close the latch of the stater relay which will allow voltage from the battery isolator onto the stater for cranking. The engine controller monitors the crank and cam sensors and will stop activating the crank control relay once the engine controller senses engine speed via the crank or cam sensors.

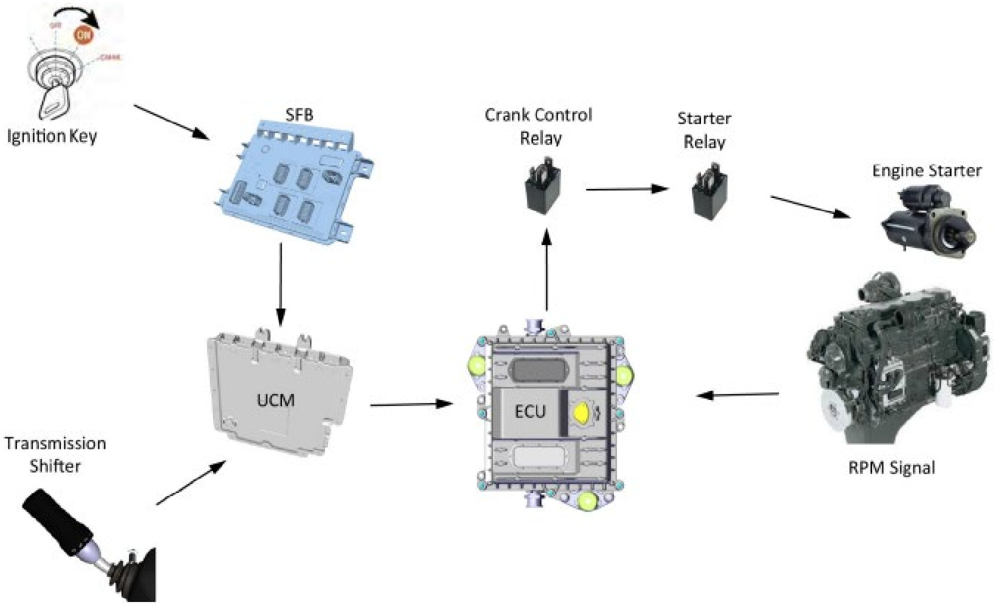

Figure 36. The Engine Starting Circuit

In our case we are using the engine load pump/motor to drive the engine ignition instead of the starter. Once we hold the ignition key switch in the ON position and the transmission shifter in neutral, we use the engine load pump/motor to drive the engine to a certain speed. If the engine receives an RPM signal, it will fire.

3.2 HIL Testbed Control

The engine operation points for a driving cycle include engine speed and load torque.

3.2.1 Engine Map Development

Engine maps are necessary for the HIL testbed control and operation. To obtain engine maps, the engine was controlled to run different steady-state operation points and the corresponding data was measured and recorded. The following methods were taken: first, the engine operation range including engine speed and torque are determined from field test data. The engine speed starts from the idling engine speed 1050 revolutions per minute (RPM) and then were grid every 100 RPM step from 1100 RPM. Engine torque range covers 0 to 300 Nm. Each set point is held until the engine reaches a steady state. Finally, all recorded data are processed to develop the engine maps. The outliers are excluded, and the measurements are averaged. Using the above method, the below steady-state engine maps can be obtained.

(1). Engine speed, pedal percentage map. Unlike on-road vehicles, due to the closed loop inside the ECU, the engine speed of the wheel loader is one-dimensional mapping with the pedal percentage. Figure 37 shows the engine speed and pedal position relationship.

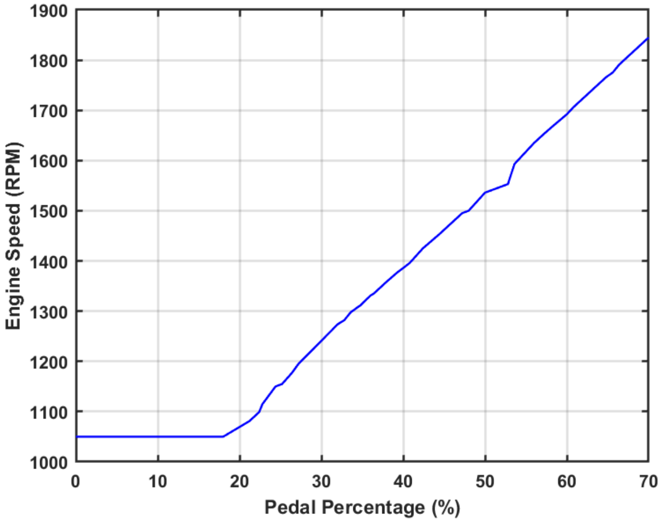

Figure 37. Engine speed and pedal position map

(2). Engine speed, engine torque and fuel consumption map. This engine map is crucial for fuel economy study. Figure 38 shows the fuel consumption map with different engine speeds and torques.

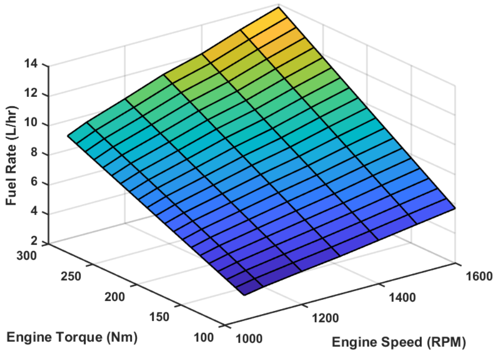

Figure 38. Engine speed, engine torque and fuel consumption map

(3). Engine speed, engine torque and HSC map. Figure 39 shows the HSC map with different engine speeds and torques.

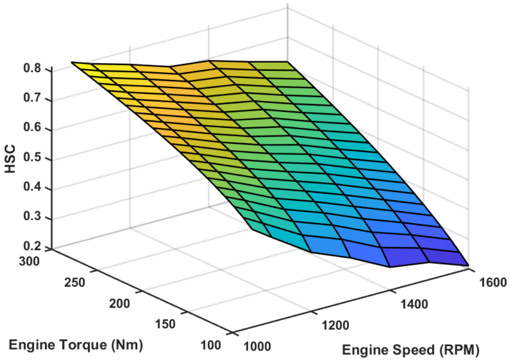

Figure 39. Engine speed, engine torque and HSC map

3.2.2 Engine Speed Control

The host computer employs MATLAB/SIMULINK, which controls the hydraulic system to provide the required load torque. Basically, LSC is fixed to keep a constant inlet pressure. The pump displacement is kept constant. We just need to change the HSC to get the desired outlet pressure. Hence, the load torque can be obtained since it is a function of the displacement and pressure drop.

To control the engine, we need to send the pedal signal by the controller instead of the real pedal so it can run the duty cycle we want. First, a real pedal is connected to get the relationship between pedal position percentage and the pedal signal voltage. It is shown in Figure 40.

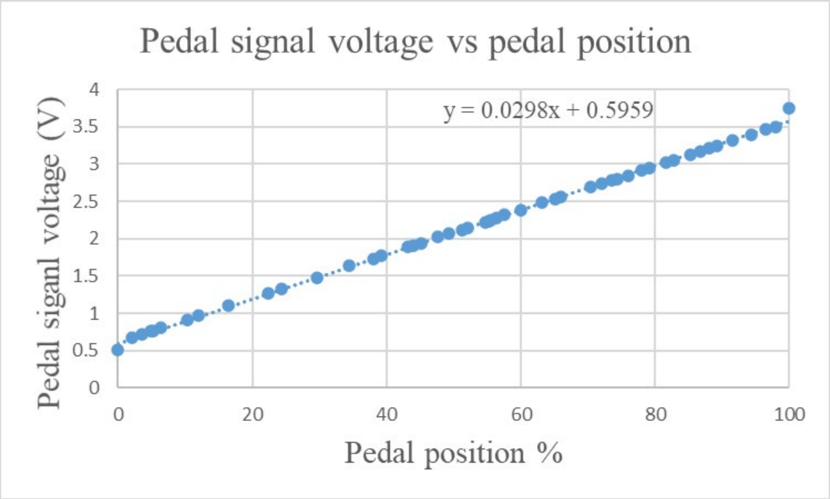

Figure 40. Relationship between Pedal Signal Voltage and Pedal Position

The pedal has the idle validation signal, which we need to send by the controller as well. The idle validation signal is ILDE when the pedal position percentage is less than 5%. When the pedal position percentage is larger than 5%, it says NOT IDLE. This can be realized by a relay, shown in Figure 41.

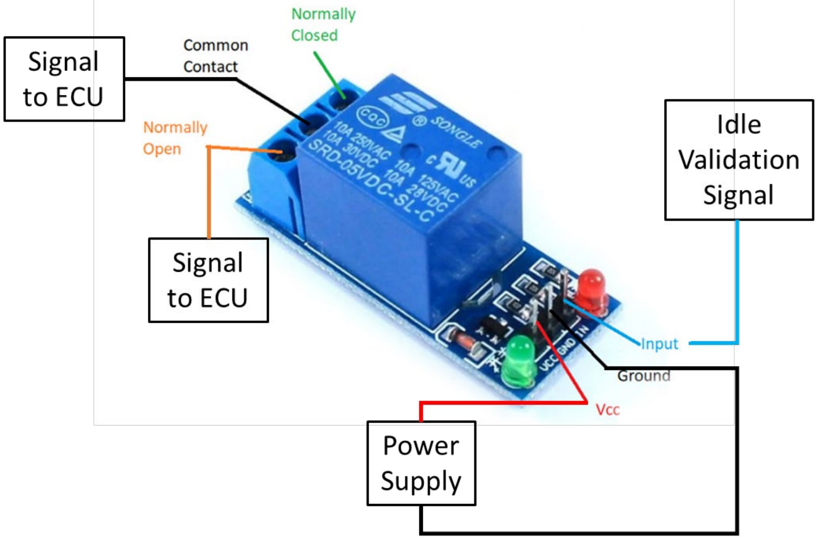

Figure 41. Idle Validation Signal Wiring Diagram

Once the test platform is set up, some tests can be performed. Based on tests, we found the engine speed is a linear function (1-D table) of pedal position, as shown in Figure 42. Therefore, if we want to achieve the desired engine speed, we can give the corresponding pedal position signal.

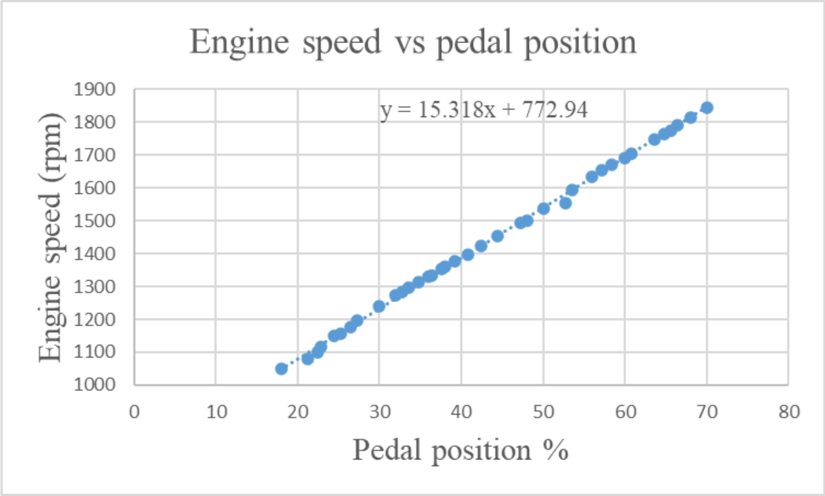

Figure 42. Relationship between Engine Speed and Pedal Position Signal

3.2.3 Load Torque Control

For a duty cycle, we not only need to realize the desired engine speed, but also need to achieve the desired engine torque. Engine load torque is applied by the EL pump/motor which is controlled by pressure drop and displacement as described in hydraulic system. In this setting, the displacement is fixed due to its relative slow response. As we use a load sensing mechanism to keep the inlet pressure constant, we change the outlet pressure of the EL pump/motor to change the load torque. From a control signal point of view, we keep LSC constant while changing HSC to change the load torque. It is worth noting that as the engine speed changes, so does the flow. Even if the HSC remains the same, the outlet pressure will change and therefore the engine torque will change. Basically, engine torque is a two-dimensional table of engine speed and HSC. We can also say that HSC is a two-dimensional table of engine speed and engine torque. The basic idea is shown in the below Figure 43.

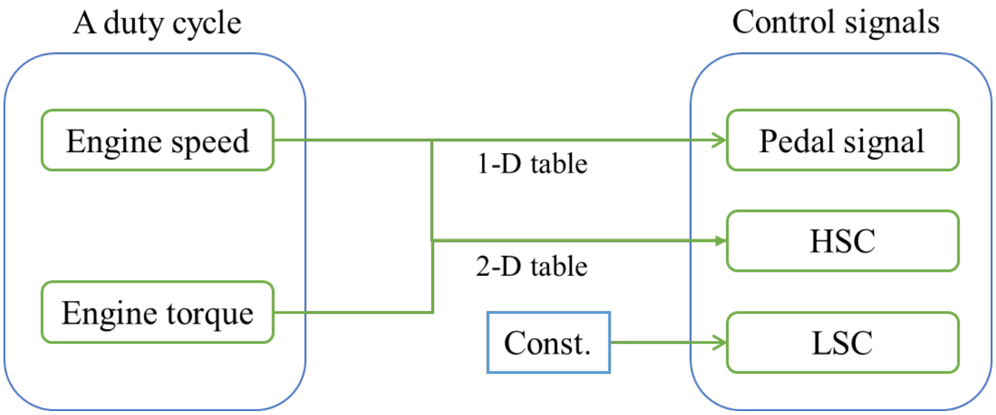

Figure 43. Diagram of Getting Control Signals from A Duty Cycle

Once we have engine operation conditions, the following method is used to achieve them using HIL.

The engine operation points for a driving cycle include engine speed and load torque. Controllers for achieving them have been designed. Figure 44 shows the controller design for engine speed control and load torque control.

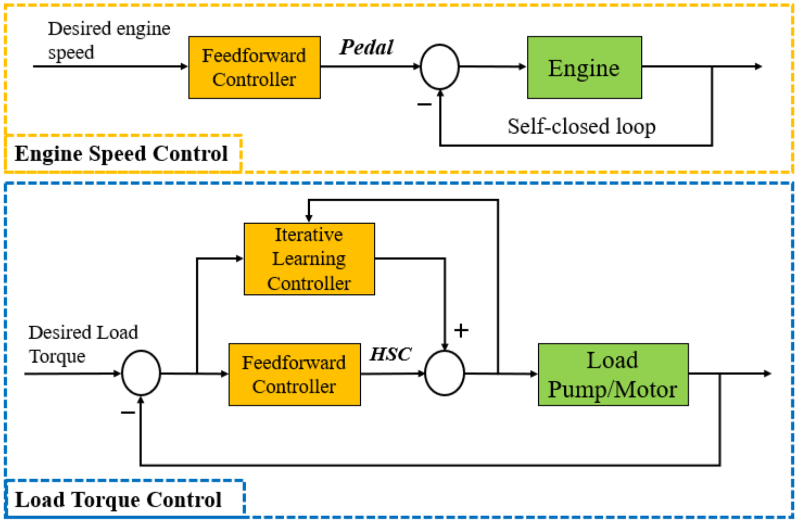

Figure 44. Controller design for tracking engine operation points

The engine speed control can be achieved by combining feed-forward control using pedal command and closed loop feedback control inside ECU. The feed-forward command can be obtained by the map from pedal percentage to engine speed. At the same time, the ECU closes the loop on the engine speed with the desired pedal percentage.

The load torque control can be achieved by the combination of feed-forward control and iterative learning control. Basically, the HSC is the control input for load torque at specific engine speed. Load torque is a 2-D mapping of engine speed and HSC, which means HSC is a 2-D mapping of engine speed and load torque as well. Hence, the feed-forward HSC command can be determined using load torque, engine speed and HSC map. If there are disturbances or unmodeled uncertainties, the pure feed-forward control would suffer bad performance. However, pure feed-forward control performs poorly in the presence of disturbances or unmodeled uncertainties. Since each cycle is repeated for different runs using the same HIL testbed, iterative learning control is a good way to handle this problem. In this case, the load torque error with a discount factor (0.5) is provided to the HSC for modification for the next run.

4. Evaluation and Testing with HIL Testbed

4.1 Baseline Evaluation

4.1.1 Cycle Description

The Standard Drive Cycle is a great way to test fuel efficiency and productivity using different techniques. For example, the standard driving cycle for on-road vehicles has been developed to test a vehicle's fuel efficiency and emissions. In the US, the standard cycle is called FTP-75 (Federal Test Procedure 75) and includes a series of tests. Likewise, the European Union has a similar standard cycle called the New European Driving Cycle (NEDC), which consists of two parts: an urban cycle and an extra-urban cycle.

However, there is no standard drive cycle for wheel loaders. Different companies and research institutes have their own drive cycles for the development of wheel loaders. Due to the complexity of the working environment and conditions, it is not convenient to test all scenarios, i.e., different loads, vehicle speeds, lift and tilt speeds. Additionally, collecting data through field tests is time-consuming and expensive.

To evaluate the impact of different techniques on fuel consumption, a driving cycle is required. The report first illustrates a systematic methodology to design a drive cycle for wheel loader, which is defined as baseline cycle. A typical drive cycle for wheel loader operation has six phases: bucket load, drive back, drive forward, and lift bucket, dump material, drive back and drive forward to pile for the next run, which is shown in Figure 45.

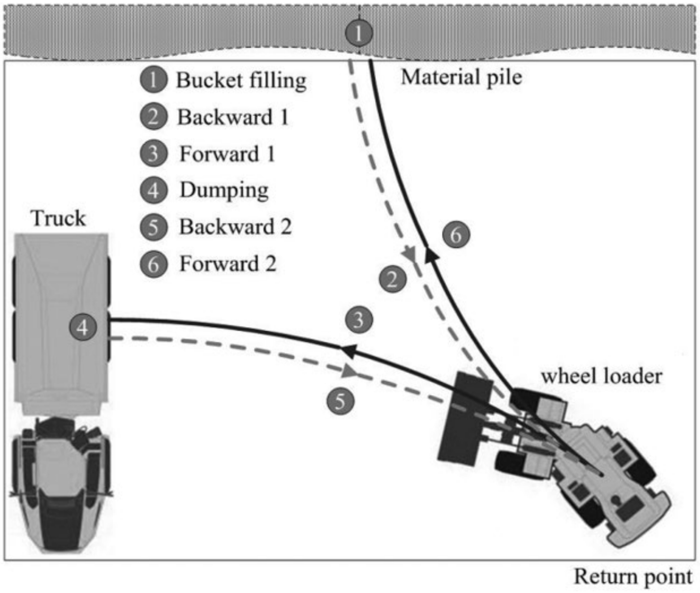

Figure 45. A typical drive cycle.

4.1.2 Methodology

The goal is to define how the wheel loader will operate, including all end-effector trajectories such as wheel speed, steering angle, bucket trajectory, given the material pile and truck position. Rule-based strategy is used to give all end-effector trajectories. A set of end-effector profiles are given in Figure 46.

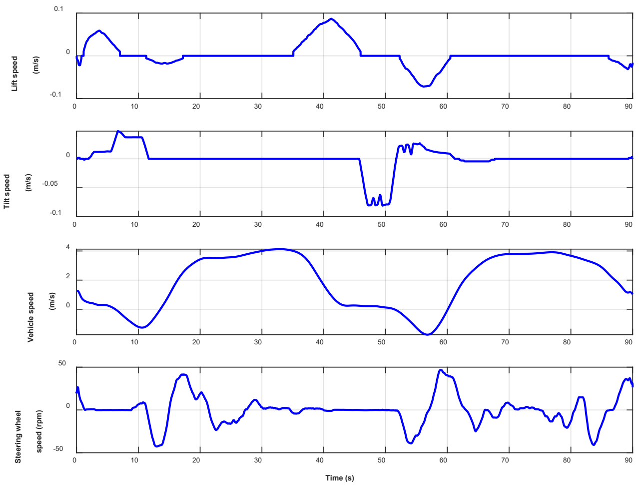

Figure 46. The baseline cycle end-effector profiles

The corresponding resistance forces and vehicle mass during the driving cycle are also shown in Figure 47.

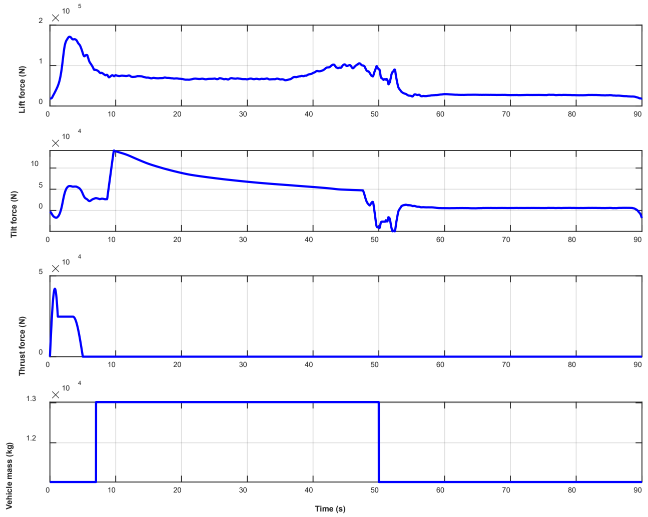

Figure 47. The baseline cycle corresponding resistance force and vehicle mass

Engine operating points are required for testing on an existing HIL testbed. From all end-effector profiles and the corresponding resistance forces, the engine operation conditions need to be determined. Based on the wheel loader powertrain feature, the engine must consider the needs of both the drivetrain and the hydraulic circuit. A strategy has been proposed to estimate the engine speed based on all the end-effector profiles including vehicle speed, steering angle, lift and tilt speed.
Figure 48 shows the engine speed estimation methodology.

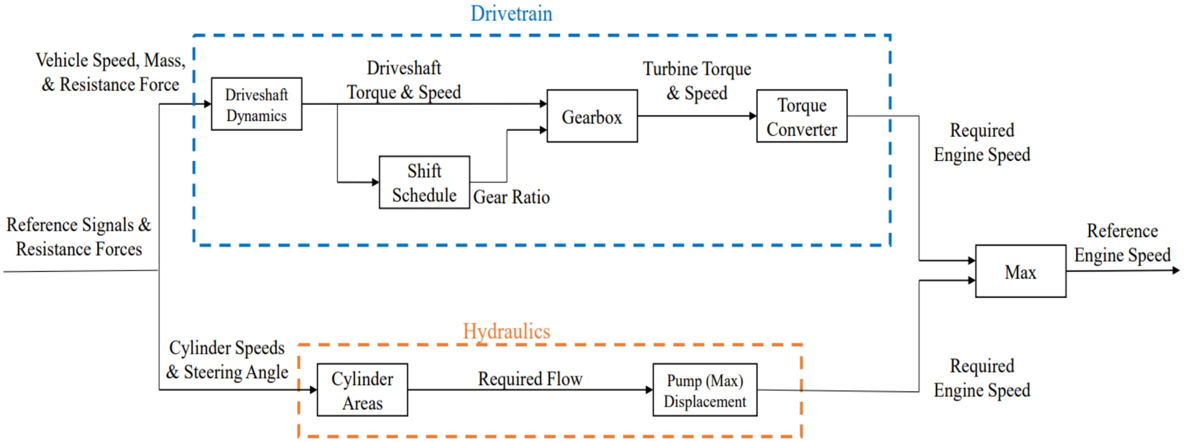

Figure 48. Engine speed estimate method.

On the upper branch, the required driveshaft speed and drive torque can be determined by the reference vehicle speed and resistance forces through the driveshaft dynamics. Based on the shift schedule, the gear ratio can be determined. Then the torque converter pump speed, which is the same as engine speed, can be determined using the torque converter model.

On the lower branch, the engine speed required by the hydraulic system can be estimated from the cylinder speeds (lift cylinder speed, tilt cylinder speed and steering cylinder speed) and their corresponding areas, where we assume the pump is at full displacement.

Then, the desired engine speed can take the maximum value of both branches at each time instance in the cycle. It implies that the engine can provide enough power for both systems.

Based on the method, the estimated engine speed is shown in Figure 49.

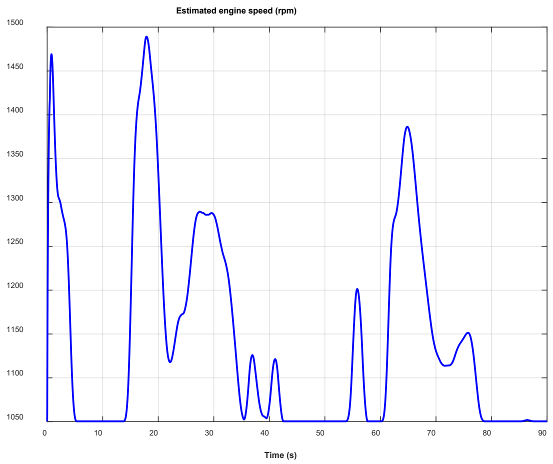

Figure 49. Estimated engine speed based on the baseline cycle end-effector profiles.

The engine torque is also required to conduct the HIL test. Forward simulation is not only used to obtain all the other required information but also validate whether the reference speeds are achievable. Using the fully validated and integrated wheel loader model, the tracking performance for all reference speeds are shown in Figure 50.

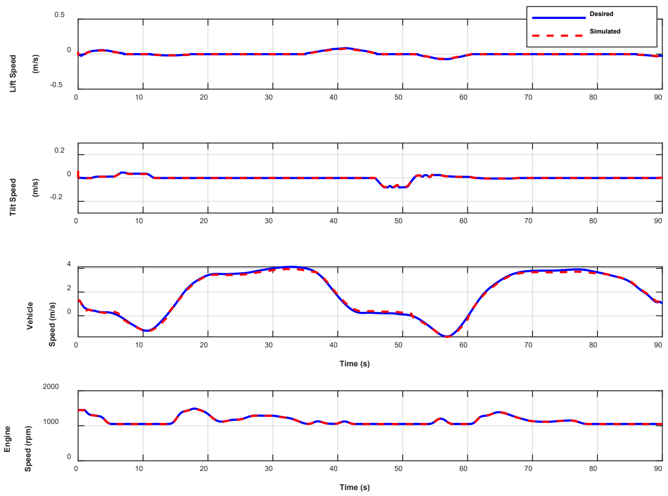

Figure 50. Reference speeds tracking performance

The RMSE are 2.8%, 1.58%, 2.7%, 0.16% for lift, tilt, vehicle, and engine speed.

The torque information including engine torque, torque converter pump torque, main pump torque, and brake pump torque are shown in Figure 51.

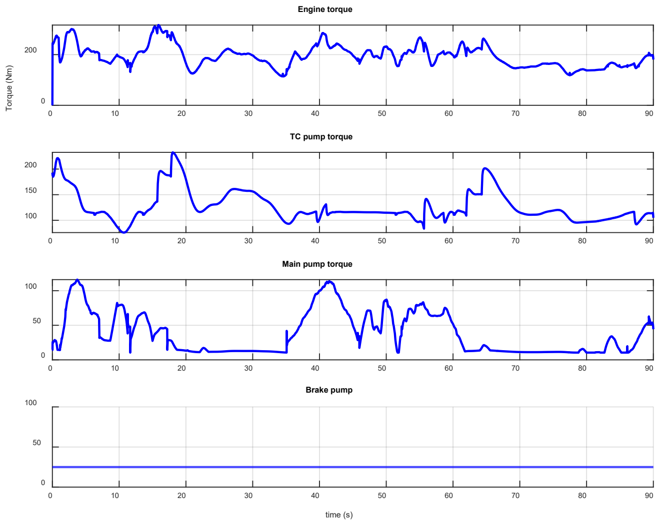

Figure 51. Simulation torque information using fully validated and integrated wheel loader model

In summary, the engine operation conditions are obtained through the above methodology for a drive cycle (baseline cycle), which are shown in Figure 52.

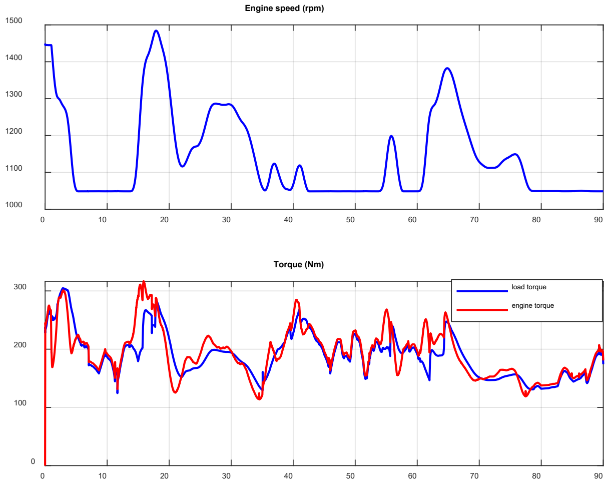

Figure 52. Baseline engine operation conditions

4.1.3 Baseline Evaluation HIL Test Result

The engine speed tracking result is shown in Figure 53.

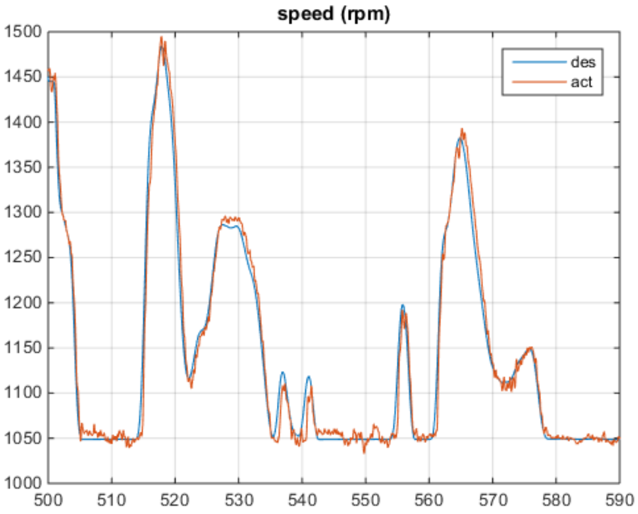

Figure 53. Baseline cycle HIL test engine speed result

The load torque tracking result is shown in Figure 54.

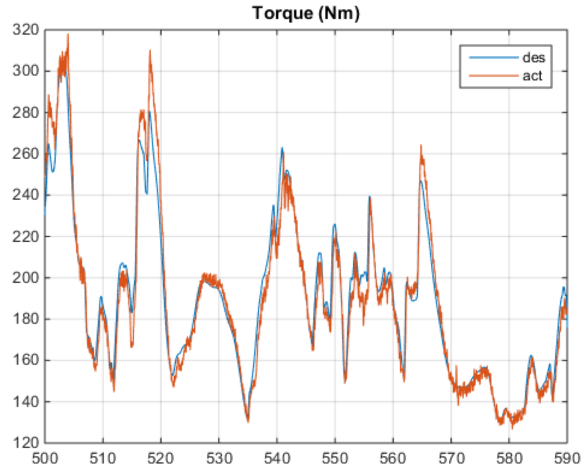

Figure 54. Baseline cycle HIL test load torque result

4.2 Partial Automation Evaluation

The main goal of this part is to evaluate partial automation optimizations compared to the baseline. First, a typical loading cycle can be divided into two parts: the digging phase and the transport phase. Their baselines should be clearly defined. Second, based on the same conditions, such as pile location, truck location, and the material need to be loaded, both digging and transport phases can be optimized. Third, both baseline and optimized results will be evaluated on the hardware-in-the-loop testbed.

4.2.1 Baseline Cycle Digging Phase

For the baseline digging phase, the pile shape is defined. The bucket needs to be filled with the full material. Assuming that the material is a medium density material, the full load mass is about 1500 kg. In the baseline cycle, the digging trajectory (blue line) and pile shape (red line) are shown in Figure 55.

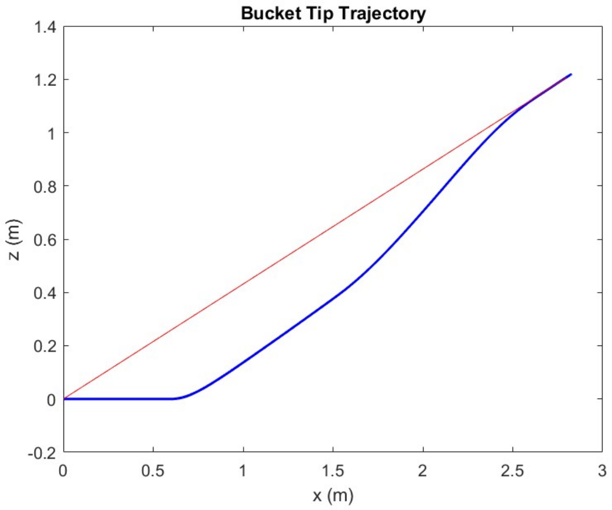

Figure 55. Baseline digging trajectory

4.2.2 Baseline Cycle Transport Phase

For the transport phase, the pile location and dump truck location are defined. The vehicle travels from pile to dump truck. In this case, the pile location is at (0,0) and the dump truck is at (14,-4).

The first step in transport is after the vehicle is loaded with material, that is, the bucket is full of material and needs to be lifted to the highest position for dumping. During the baseline cycle, the bucket is raised to 3.93 meters.

The second part of the transport is after dumping is finished, the vehicle bucket is empty, and the machine needs to drive from the dump truck position to the pile position for the next cycle.

Since the simulated wheel loader model has an engine map, the fuel consumption at different stages can be obtained, as shown in Table 1.

Table 1. Simulation fuel consumption for different phases in baseline

Simulation fuel consumption (g)	Transportation with lifting	Transportation after dumping	Total transport	Digging
Baseline	30.36	29.6	59.96	28.72

4.2.3 Optimization for Digging Phase.

Based on the same conditions, the optimization for digging phase is finished.

The optimized bucket tip trajectory is shown in Figure 56.

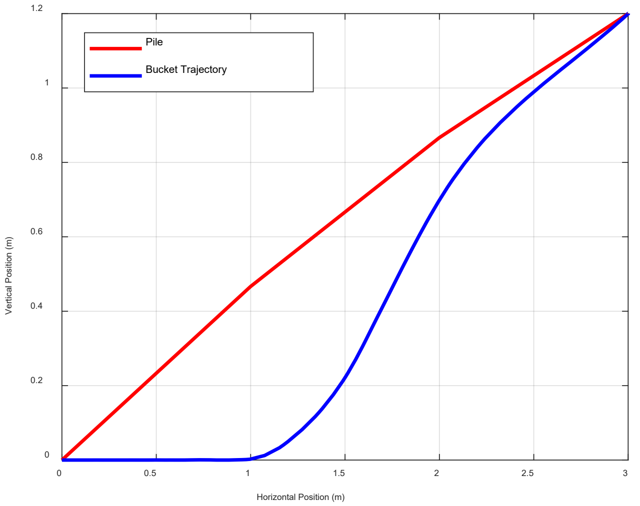

Figure 56. Optimization digging trajectory

To achieve the above bucket tip trajectory, the vehicle speed, bucket velocity and bucket height are shown in Figure 57.

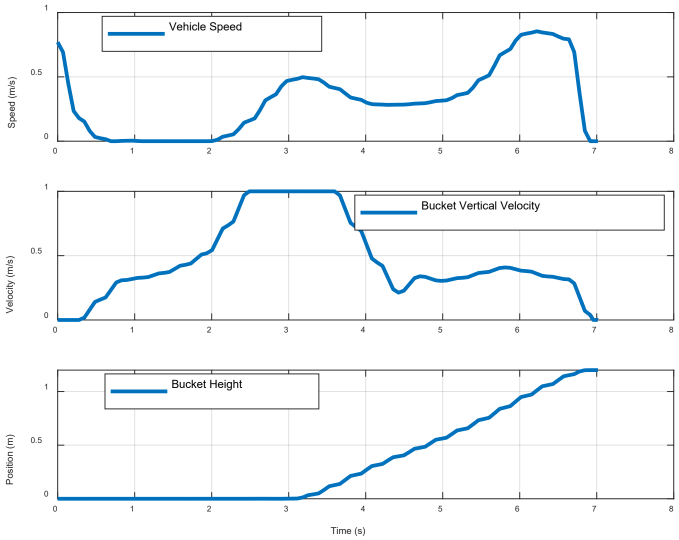

Figure 57. Vehicle speed, bucket velocity and height during the optimized digging

The optimized engine torque, torque converter pump torque and main pump torque are shown in Figure 58.

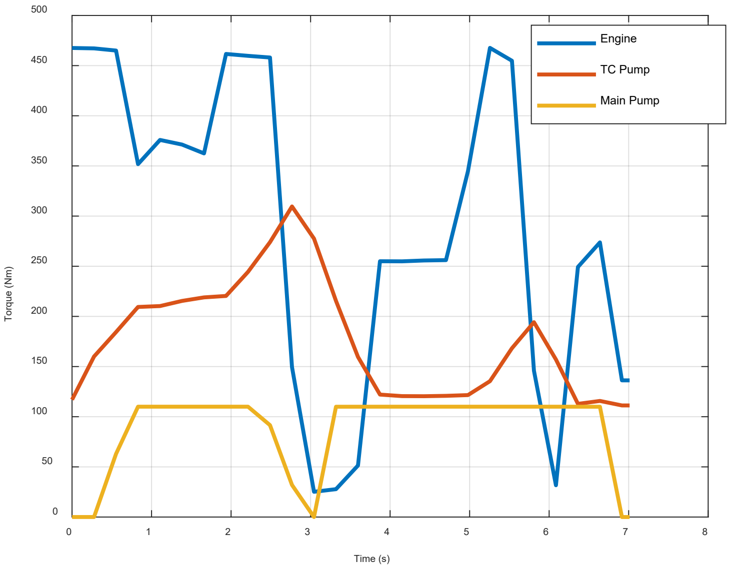

Figure 58. Torque information of the optimized digging

The engine speed and load torque for optimized digging phase is shown in Figure 59.

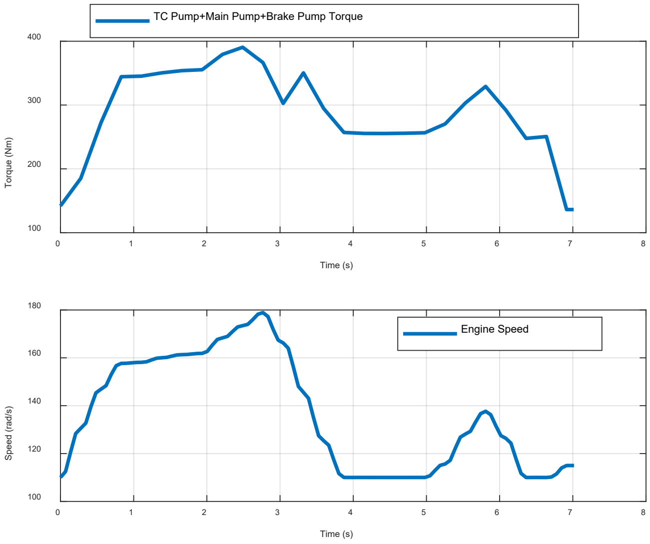

Figure 59. Engine speed and load torque for the optimized digging

4.2.4 Optimization for Transport Phase.

Based on the same pile location and dump truck location, optimization is finished for both parts of transport.

4.2.4.1 Transport Phase with Lifting Bucket

The first part in which the vehicle travels from pile location to dump site is optimized. The bucket is full of material. The optimized vehicle trajectory is shown in Figure 60.

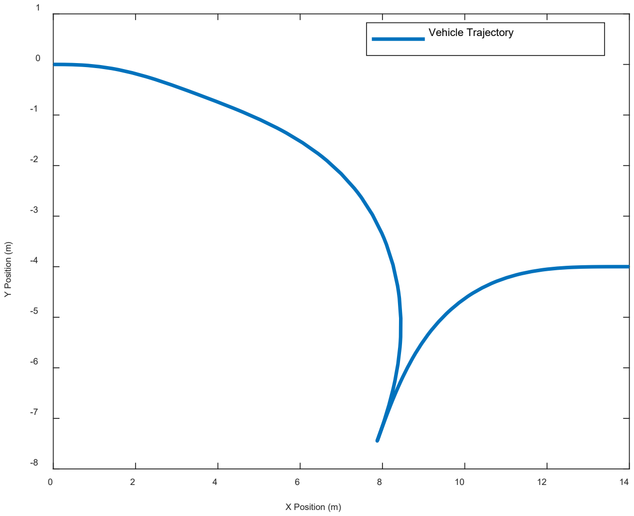

Figure 60. Optimized vehicle trajectory for transport with bucket lifting

During transportation, the bucket is lifted to 4 meters preparing for dumping, which is shown in Figure 61.

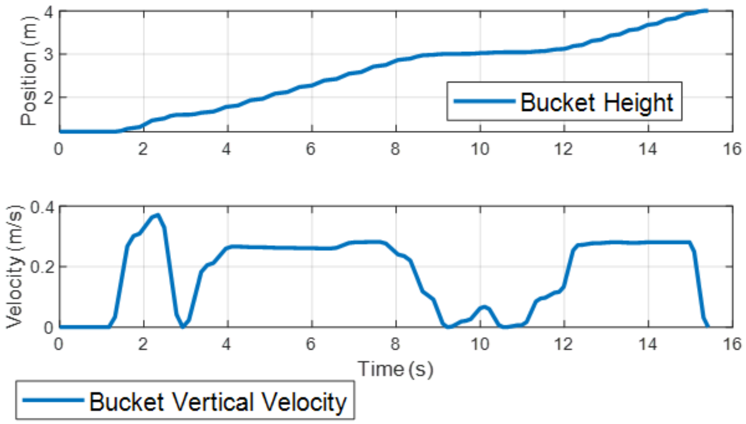

Figure 61. Bucket height and velocity during transport with bucket lifting

The vehicle speed, heading angle, steering angle and steering speed are shown in Figure 62.

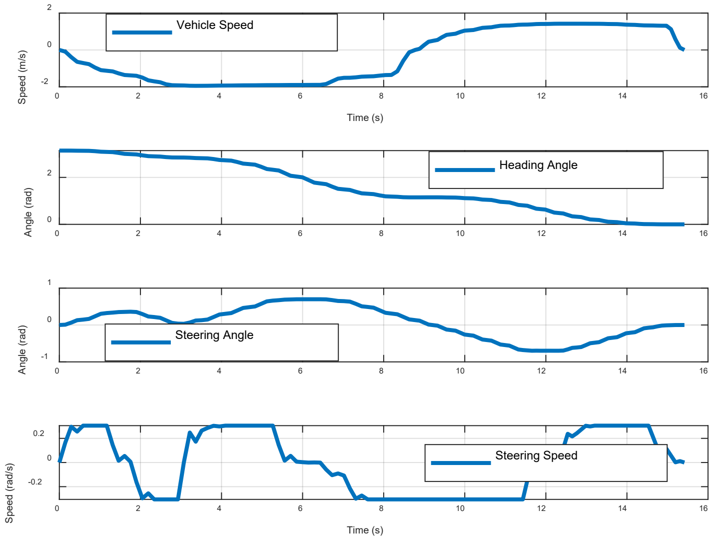

Figure 62. Vehicle speed, heading angle, steering angle and steering speed during transport with bucket lifting

The optimized engine torque, torque converter pump torque and main pump torque are shown in Figure 63.

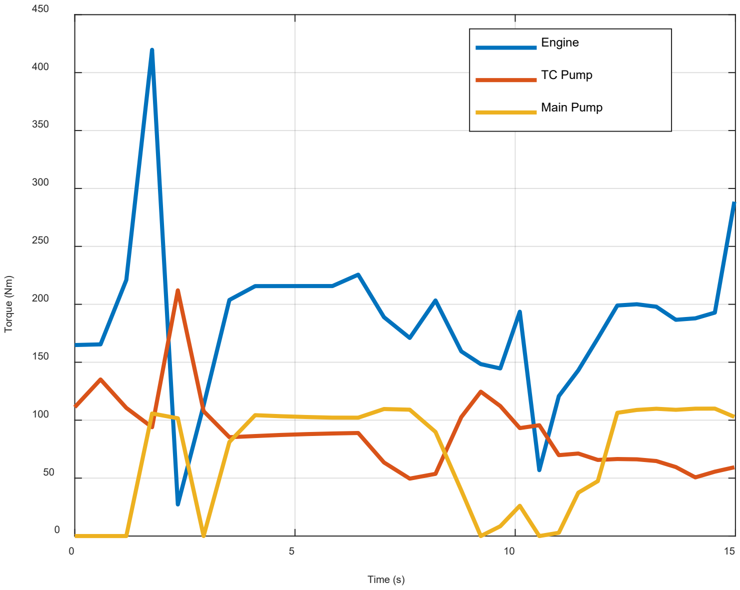

Figure 63. Engine torque, torque converter pump torque and main pump torque during transport with bucket lifting

The corresponding engine speed and load torque for this part of transport are shown in Figure 64.

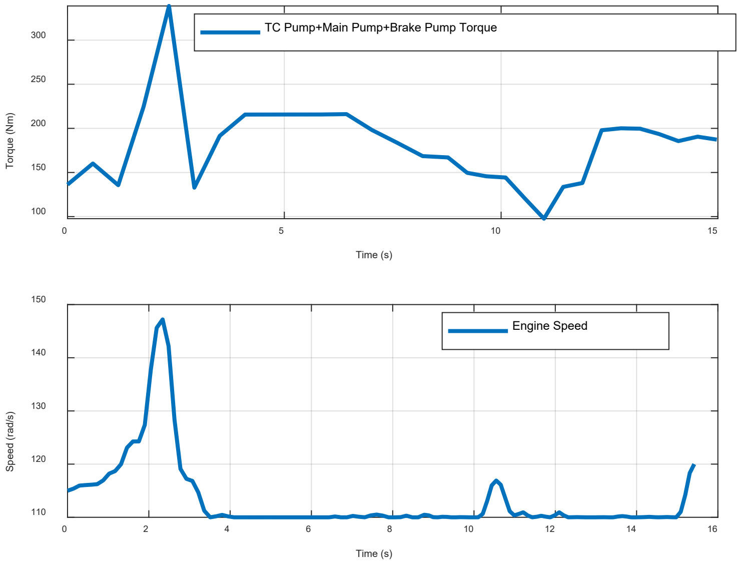

Figure 64. Engine speed and load torque during transport with bucket lifting

The fuel consumption will be measured from the HIL testbed based on the above engine points.

4.2.4.2 Transport Phase after Dumping

The second part of transport is vehicle travels from dump location to pile location after dumping. The vehicle trajectory of this part of transport is shown in Figure 65.

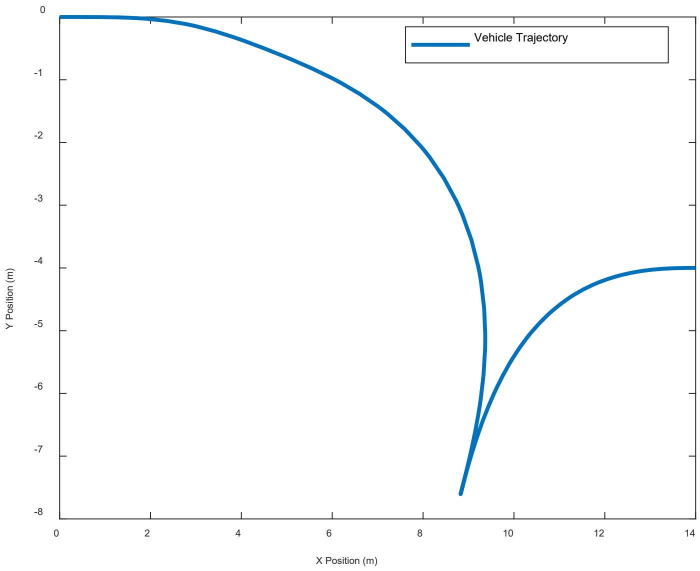

Figure 65. Optimized vehicle trajectory for transport after dumping

The vehicle speed, heading angle, steering angle and steering speed are shown in Figure 66.

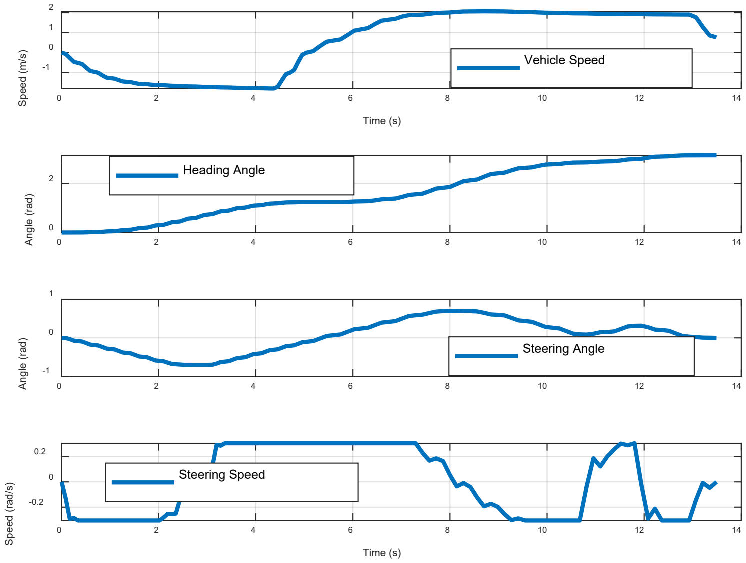

Figure 66. Vehicle speed, heading angle, steering angle and steering speed during transport after dumping

The corresponding engine speed and load torque for this part of transport are shown in Figure 67.

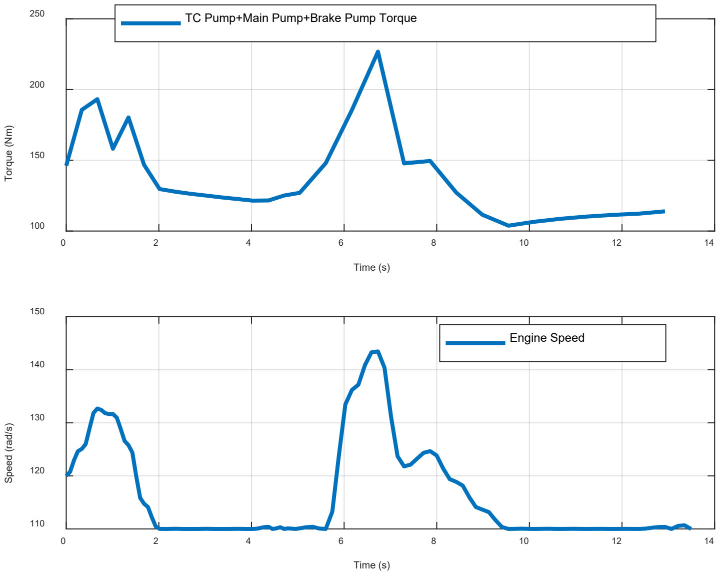

Figure 67. Engine speed and load torque during transport after dumping

The fuel consumption will be measured from the HIL testbed based on the above engine points.

4.2.5 Partial Automation Evaluation

4.2.5.1 Digging Phase Comparison

The optimized digging phase HIL test result is shown in Figure 68.

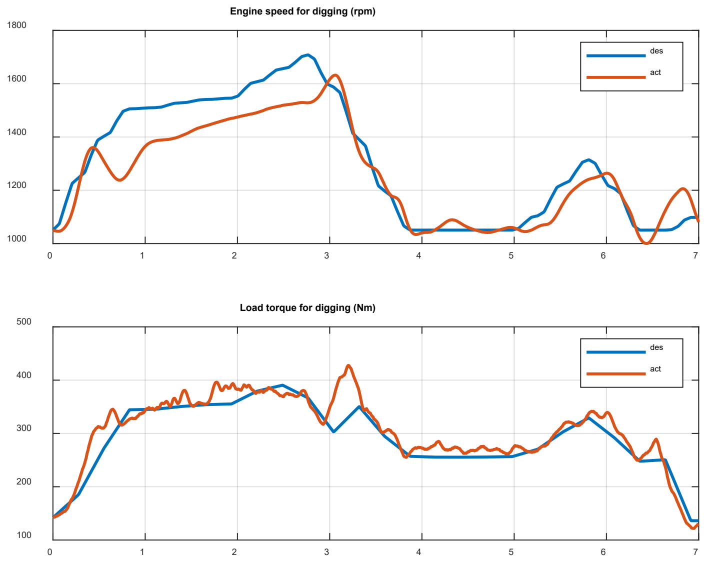

Figure 68. HIL test result for optimized digging phase

The digging phase HIL fuel consumption is 29.59 grams.

4.2.5.2 Transport Phase Comparison

The optimized transport with bucket lifting HIL test result is shown in Figure 69.

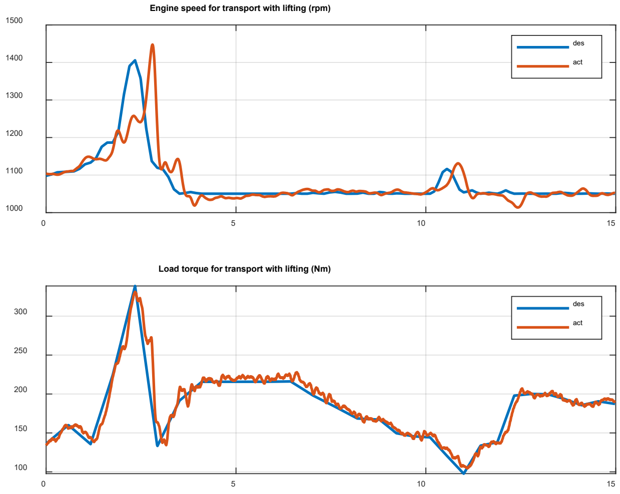

Figure 69. HIL test result for optimized transport with bucket lifting

The optimized transport after dumping HIL test result is shown in Figure 70.

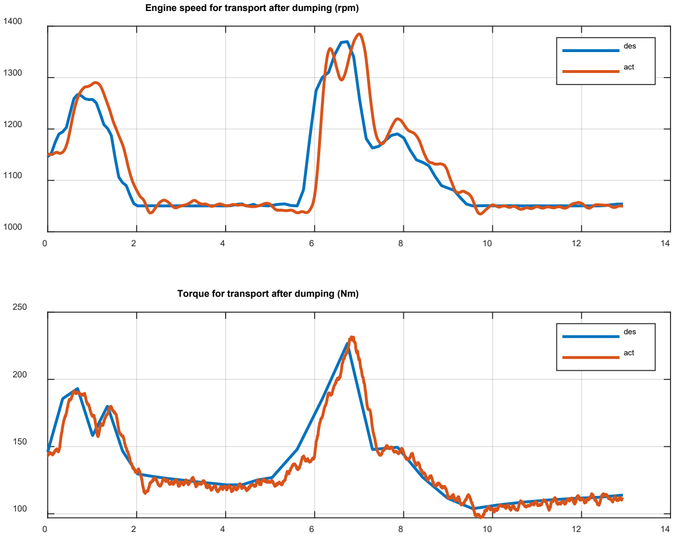

Figure 70. HIL test result for optimized transport after dumping

4.2.5.3 Partial Automation Comparison Summary

The simulation and HIL fuel consumption for transport phase for both baseline and optimization are listed in the table below.

Table 1. Fuel consumption at different phases in HIL and simulation baseline and optimization

Fuel consumption (grams)	Transportation with lifting	Transportation after dumping	Total transport	Digging
Baseline Simulation	30.36	29.6	59.96	28.72
Baseline HIL	34.46	31.73	66.19	29.59
Optimization simulation	21.23	14.25	35.48	18.15
Optimization HIL	23.16	17.62	40.78	19.26
Benefit simulation	30.1%	51.9%	40.8%	36.7%
Benefit HIL	32.8%	44.5%	38.4%	34.9%

First, the test results show that the HIL verifies the simulation results. Second, with the proposed optimization algorithm, partial automation such as digging phase and transport phase can achieve fuel efficiency of about 30%.

4.3 Joint Automation Evaluation

The main goal of this section is to evaluate joint automation optimizations compared to the baseline. First, a typical loading cycle is defined. Second, based on the same conditions, such as pile location, truck location, and the material that needs to be loaded, the loading cycle can be optimized. Third, both baseline and optimized results would be evaluated on the hardware-in-the-loop testbed.

4.3.1 Joint Optimization Simulation Result

The joint optimization has been implemented based on the algorithm developed in this project. The same conditions, such as stockpile position, truck location, and material properties, are used to set the conditions and constraints for optimization. The optimization results have been described as follows.

The optimized engine operation points and engine fuel injection are shown in Figure 71.

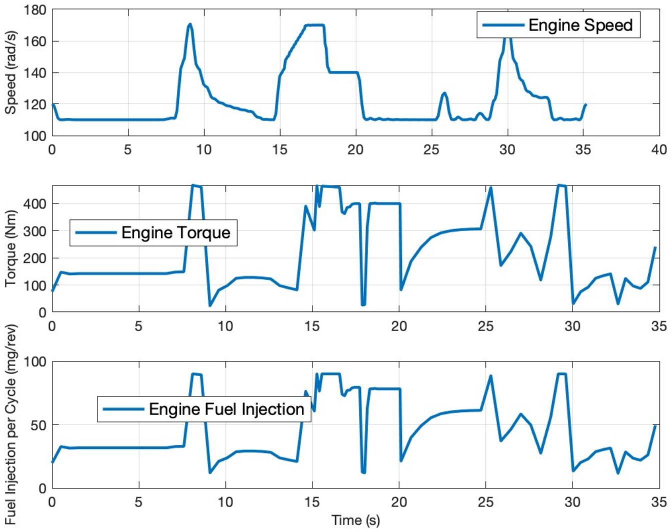

Figure 71. Engine operation points and fuel injection for optimized cycle

The torque converter operation conditions are shown in Figure 72.

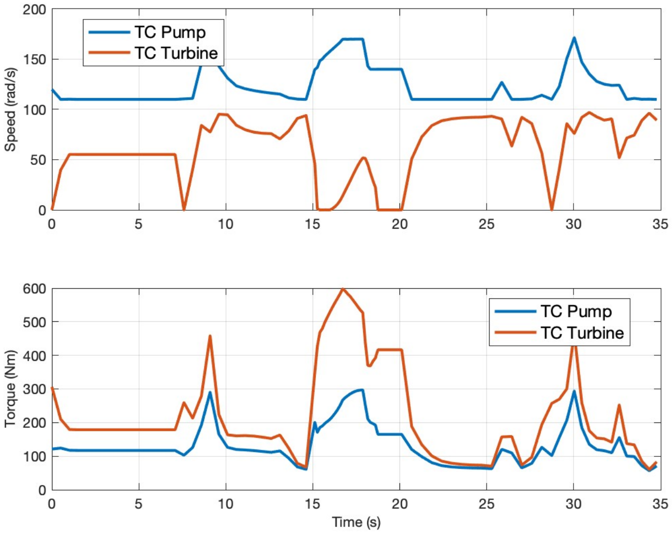

Figure 72. Torque converter operation conditions for optimized cycle

The optimized vehicle trajectory is shown in Figure 73.

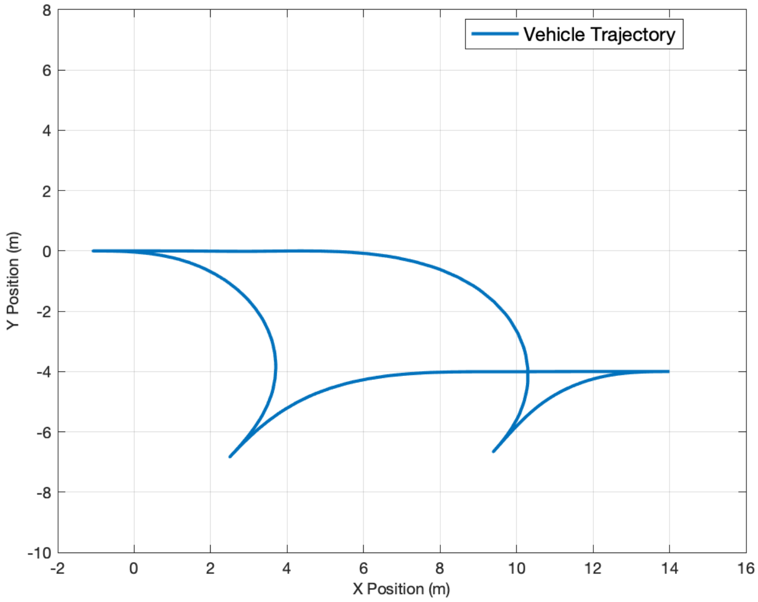

Figure 73. Vehicle trajectory for the optimized cycle

The optimized vehicle speed is shown in Figure 74.

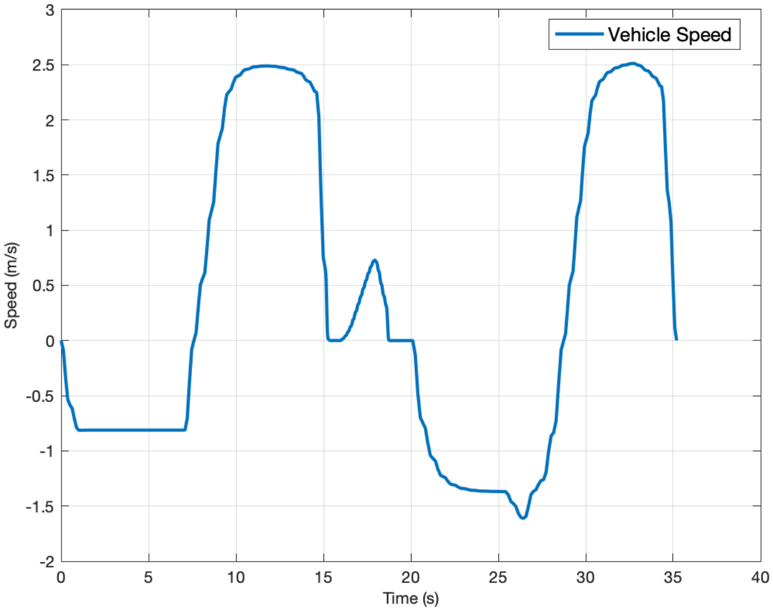

Figure 74. Vehicle speed for optimized cycle

The corresponding vehicle operation variables are shown in Figure 75.

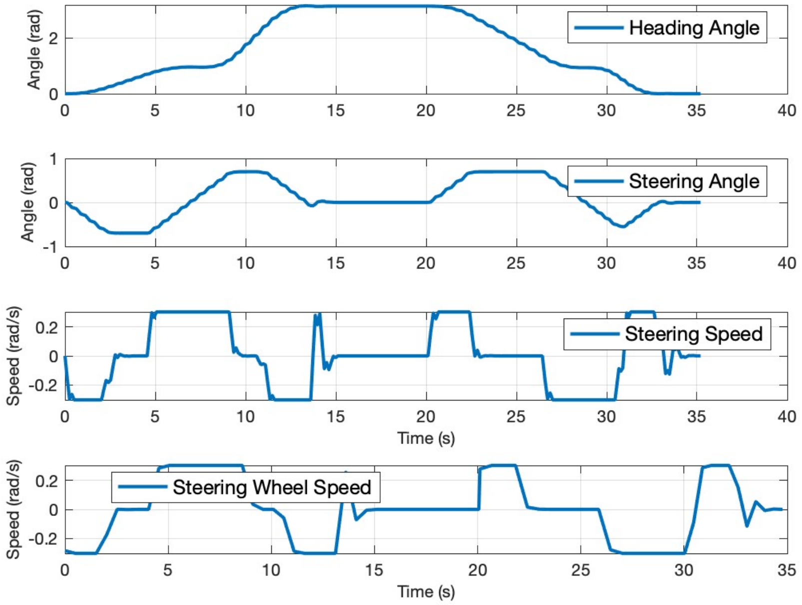

Figure 75. Heading angle, steering angle, steering speed and steering wheel speed for optimized cycle

The bucket trajectory during digging is shown in Figure 76.

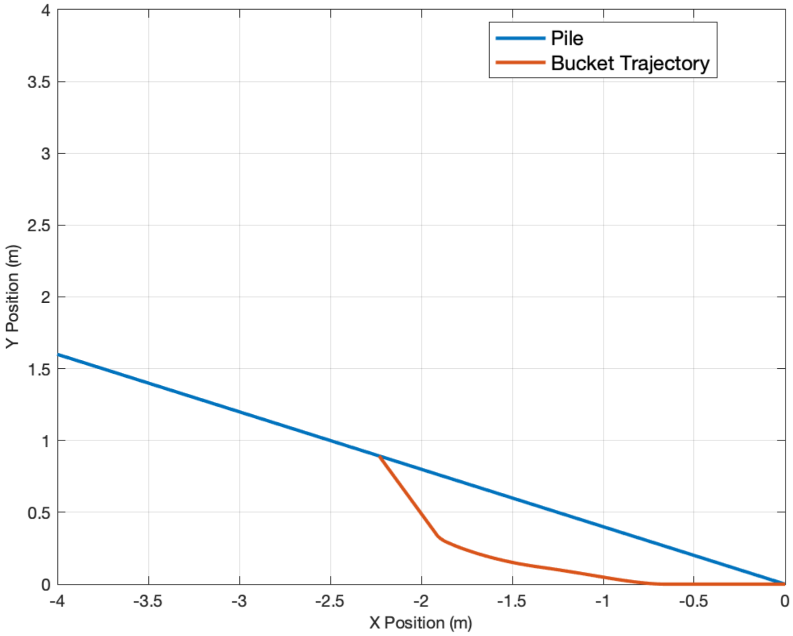

Figure 76. Bucket trajectory during digging for optimized cycle

The bucket digging loading area is shown in Figure 77. This ensures that the loaded material is the same as the baseline cycle.

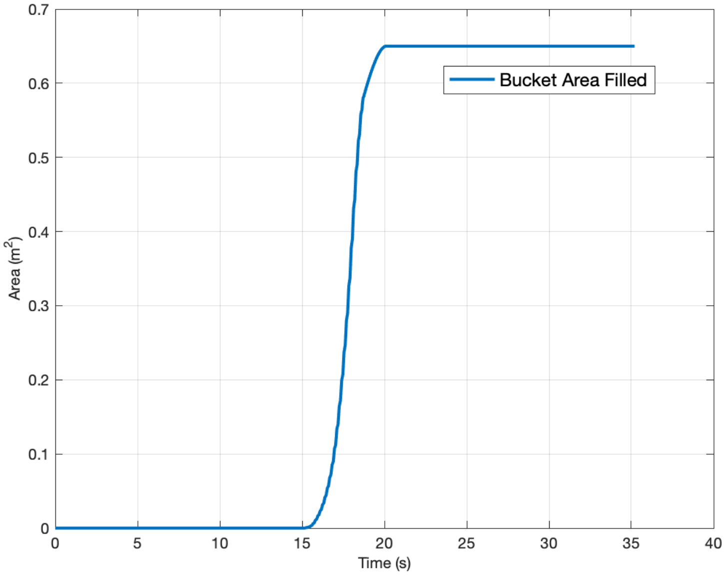

Figure 77. Bucket digging area for optimized cycle

The whole optimized cycle bucket motion is shown in Figure 78.

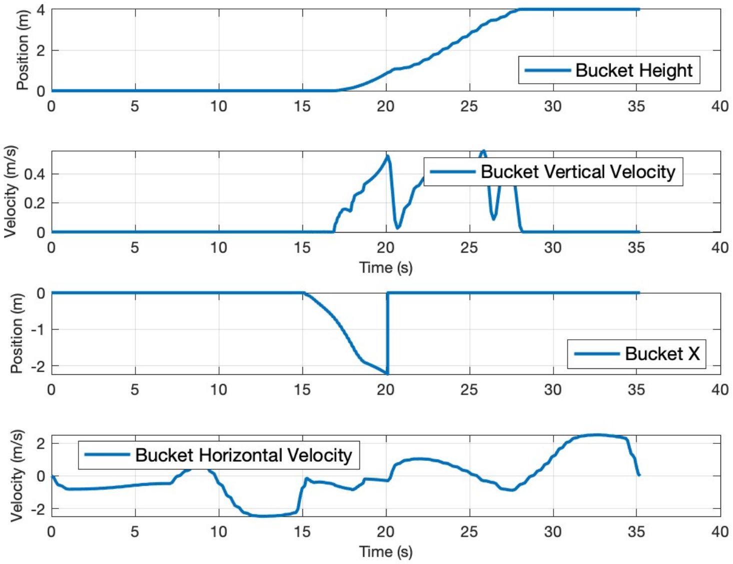

Figure 78. Bucket motion for optimized cycle

The corresponding bucket orientation is shown in Figure 79.

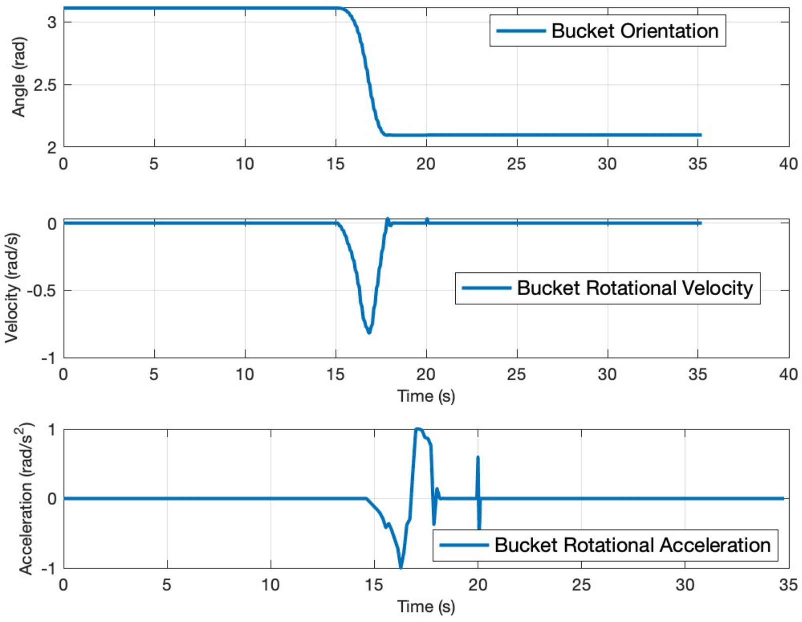

Figure 79. Bucket orientation for optimized cycle

The fuel consumption will be measured from the HIL testbed based on the above engine points.

4.3.2 Joint Optimization HIL Test Result

The baseline cycle tracking HIL testbed result is shown in Figure 80.

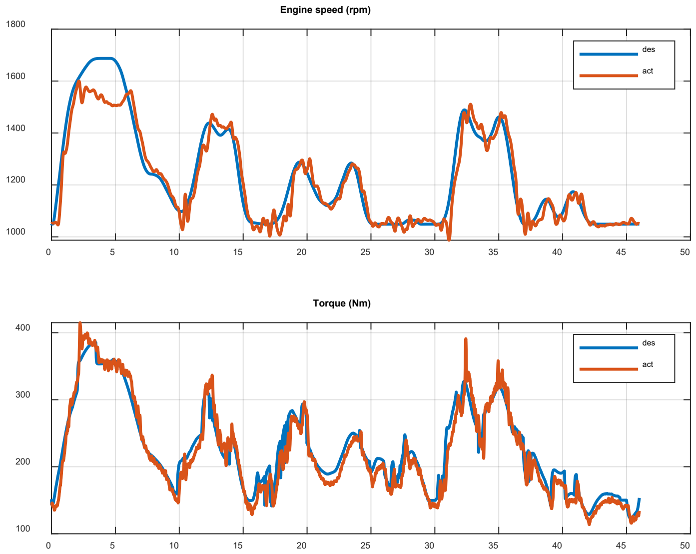

Figure 80. Baseline HIL test result

The Root-Mean-Square-Error of engine speed and load torque are 3.56% and 4.3%, which are less than 5%.

The optimized cycle engine speed tracking HIL testbed result is Figure 81.

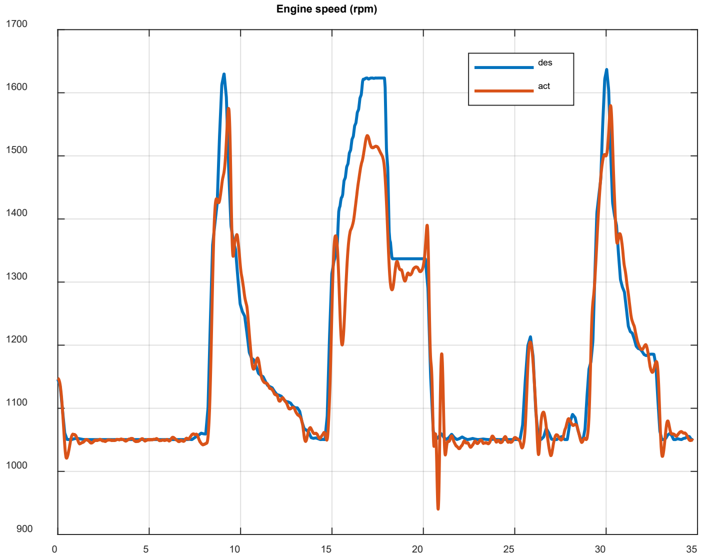

Figure 81. Optimized cycle HIL engine speed tracking

The optimized cycle load torque tracking HIL testbed result is shown in Figure 82.

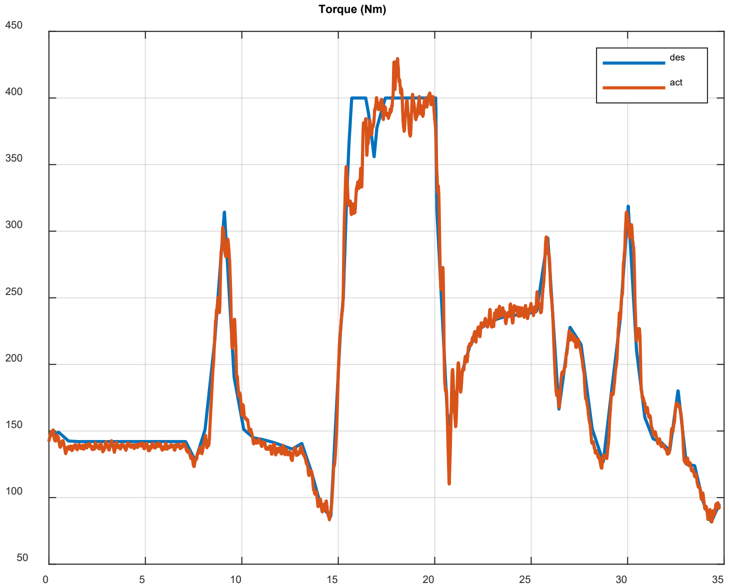

Figure 82. Optimized cycle HIL load torque tracking

The Root-Mean-Square-Error of engine speed and load torque are 3.1% and 3.3%, which are less than 5%.

4.3.3 Joint Automation Evaluation Summary

The simulation and HIL fuel consumption results of baseline cycle and optimized cycle are listed in the table below.

Table 3. Fuel consumption in HIL and simulation baseline and optimization

Fuel Consumption (grams)	Baseline Simulation	Baseline HIL	Optimization Simulation	Optimization HIL	Benefits Simulation	Benefits HIL
Total	92.99	95.83	62.83	65.38	32.4%	31.8%

First, the test results show that the HIL verifies the simulation results. Second, with the proposed optimization algorithm, joint automation can achieve more than 30% fuel benefit.

4.4 Different Scenarios Evaluation

In this joint optimization scenario, the dump truck is positioned at (14, -4) m, while the stockpile is situated at (0,0) m. It's important to clarify that these positions are referenced from the short-loading cycle data provided by CNH. Additionally, the mass of the material loaded by the bucket is 1500 kg, although it can be up to 4000 kg under normal circumstances. To demonstrate the robustness of our proposed optimization algorithm, we consider two profiles for the stockpile in this setup: a straight line and a curve.

4.4.1 HIL Evaluation for the Straight-Line Pile Optimization Profile

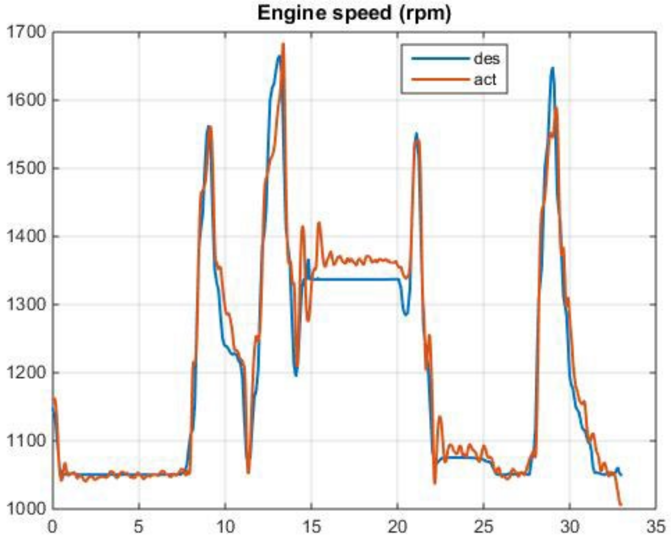

Figure 83. Engine Speed Tracking Performance

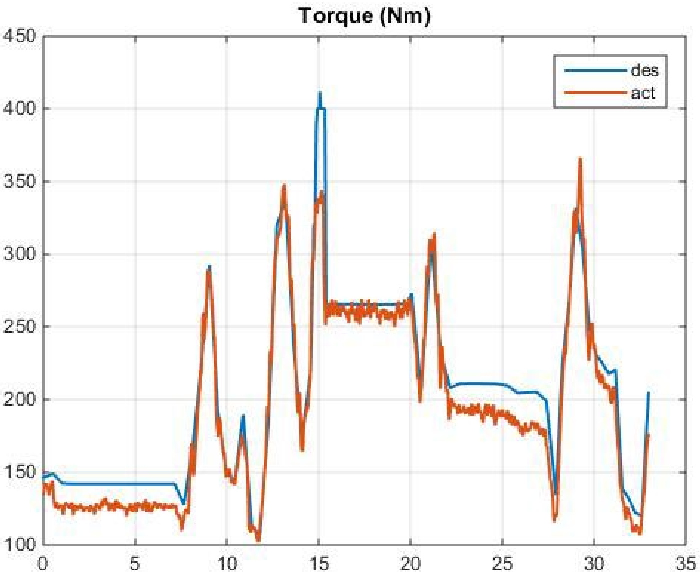

Figure 84. Engine Torque Tracking Performance

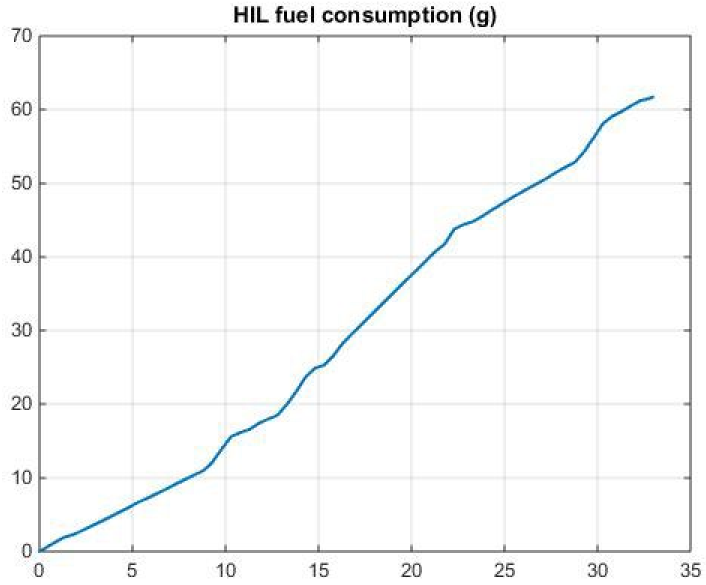

Figure 85. Fuel Consumption HIL Testing

The root mean square error (RMSE) for engine speed tracking is 2.11%, while for torque tracking, it is 4.81%. The fuel consumption is 61.68 grams.

4.4.2 HIL Evaluation for the Curve Pile Optimization Profile

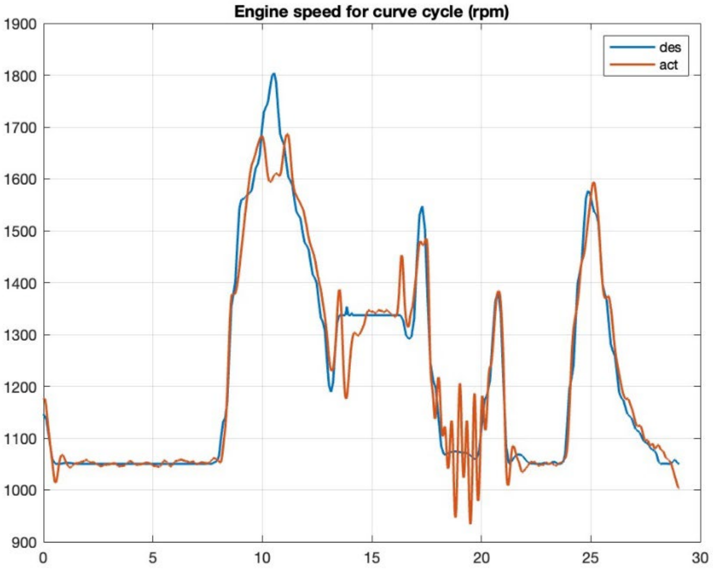

Figure 86. Engine Speed Tracking Performance

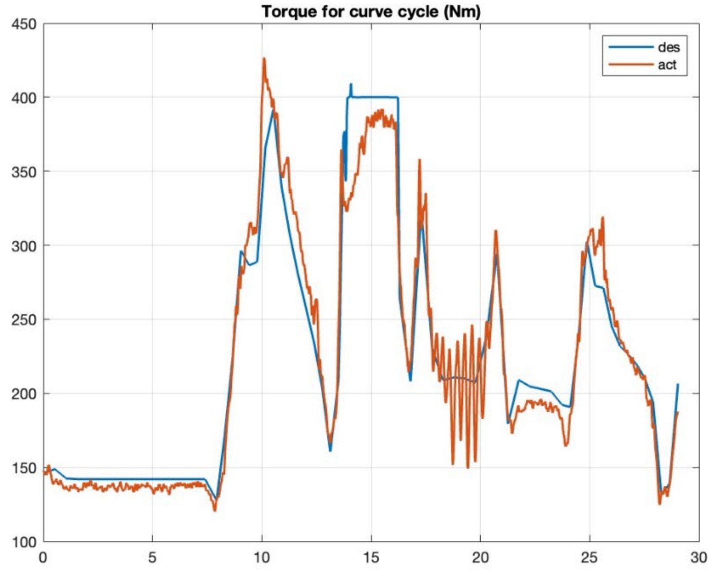

Figure 87. Engine Torque Tracking Performance

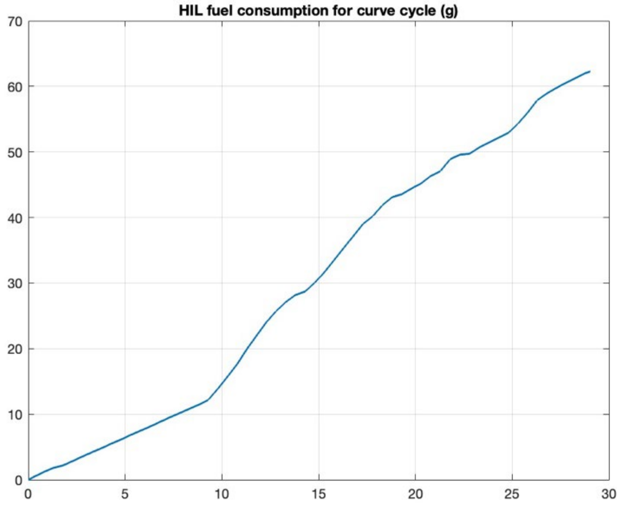

Figure 88. Fuel Consumption HIL Testing

The root mean square error (RMSE) for torque tracking is 4.57%, while for engine speed tracking, it is 2.6%. The fuel consumption is 62.27 grams.

The baseline cycle consumes fuel at a rate of 84.7 grams. Moreover, the baseline cycle takes 43 seconds, while the two optimized cycles take 33 seconds and 29 seconds, respectively. These optimized cycles significantly improve productivity. Both the simulated optimization results and the HIL testing results verify the achievability of fuel improvement through the proposed optimization algorithm and motion control strategy.

5. Summary and Conclusions

This project aimed to address the challenges of optimizing energy consumption and productivity in autonomous off-road vehicles by developing and validating a novel optimization and control system. The work was divided into three key components: optimization and control system development, HIL testbed design, and real-time testing and evaluation.

The optimization and control system focused on co-optimizing the vehicle's speed, tool motion, and powertrain dynamics to achieve significant fuel efficiency improvements without sacrificing productivity. By employing advanced real-time control algorithms and leveraging simplified models, the system dynamically adjusted vehicle parameters based on operational data. This approach allowed the system to reduce fuel consumption and optimize the vehicle's performance across various tasks, particularly during digging and transportation phases.

The project developed a Hardware-in-the-Loop (HIL) testbed, which played a critical role in validating the optimization and control algorithms. The HIL testbed combined the actual engine with virtual models of the hydraulic, steering, and powertrain systems, enabling the simulation of real-world working conditions. This reconfigurable testbed allowed for extensive testing under various scenarios, ensuring the reliability and scalability of the system.

During the evaluation and testing phase, the HIL testbed was used to simulate different vehicle operating conditions, including digging and transportation cycles. The real-time tests demonstrated that the optimized system achieved more than 30% fuel savings compared to conventional human-operated cycles. The results highlighted the effectiveness of the co-optimization approach in balancing fuel efficiency and productivity, making a strong case for its potential implementation in real-world applications.

Conclusions:
The project successfully demonstrated that energy savings of over 30% are achievable in autonomous off-road vehicles through the integration of advanced optimization and control strategies. The HIL testbed provided a reliable and controlled environment for validating these methods, proving that they can operate effectively under real-world conditions. Future work should focus on expanding the application of this optimization framework to other vehicle types and refining the control algorithms to further enhance system performance. The project showcases the potential for autonomous technologies to revolutionize off-road vehicle operations, contributing to significant reductions in energy consumption and operational costs.

6. Publications and Patents

[1] Yao, J., Edson, C. P., Yu, S., Zhao, G., Sun, Z., Song, X., & Stelson, K. A. (2023). Bucket Loading Trajectory Optimization for the Automated Wheel Loader. *IEEE Transactions on Vehicular Technology*, 72(6), 1–11.

[2] Edson, C. P., Yao, J., Zhao, G., & Sun, Z. (2023). Joint Optimization for Transport and Bucket Loading Phases of Automated Wheel Loaders. *IEEE/ASME Transactions on Mechatronics*, 28(4), 1–9.

[3] Yu, S., Zhao, G., Song, X., & Sun, Z. (2023). Control Oriented Model Order Reduction for the Hydraulic System of an Autonomous Wheel Loader. *Control Engineering Practice*, 139. Article. No. 105628.

[4] Zhao, G., Edson, C. P., Yao, J., Sun, Z., & Stelson, K. A. (2023). Development of a Dynamical Model and Energy Analysis for Wheel Loader. *Proceedings of the Institution of Mechanical Engineers. Part D, Journal of Automobile Engineering*.

[5] Yu, S., Song, X., & Sun, Z. (2023). On-Line Prediction of Resistant Force During Soil–Tool Interaction. *ASME Journal of Dynamic Systems, Measurement, and Control*, 145(8), 081004.

[6] Zhao, G., Yao, J., Connor, E., & Sun, Z. (2024). Design, Modeling, and Control of a Hardware-in-the-Loop Testbed for Off-Road Vehicles. *ASME Letters in Dynamic Systems and Control*.

[7] Yu, S., Song, X., & Sun, Z. (2024). Real-Time Gear-Shift Optimization for an Autonomous Wheel Loader. *IEEE Transactions on Control Systems Technology*.

[8] Song, X., Yu, S., & Sun, Z. (2024). Systems and methods for predicting external resistive forces encountered by industrial machines (Patent)

[9] Song, X., & Paramasivan, A. (2022). Method for Autonomous Optimal Management of Connected, Autonomous, or Conventional Machineries in Construction and Mining Worksites (Patent)

[10] Sun, Z., Zhao, G., Edson, C.P., & Yao, J. (2023). Control System for Automated Wheel Loader (Patent)